

AWARD NUMBER: W81XWH-16-1-0375

TITLE: SERS Nanosensors for in vivo Glucose Sensing

PRINCIPAL INVESTIGATOR: Richard Van Duyne

CONTRACTING ORGANIZATION: Northwestern University  
Evanston, IL 60208

REPORT DATE: September 2017

TYPE OF REPORT: Annual

PREPARED FOR: U.S. Army Medical Research and Materiel Command  
Fort Detrick, Maryland 21702-5012

DISTRIBUTION STATEMENT: Approved for Public Release;  
Distribution Unlimited

The views, opinions and/or findings contained in this report are those of the author(s) and should not be construed as an official Department of the Army position, policy or decision unless so designated by other documentation.

# REPORT DOCUMENTATION PAGE

Form Approved  
OMB No. 0704-0188

Public reporting burden for this collection of information is estimated to average 1 hour per response, including the time for reviewing instructions, searching existing data sources, gathering and maintaining the data needed, and completing and reviewing this collection of information. Send comments regarding this burden estimate or any other aspect of this collection of information, including suggestions for reducing this burden to Department of Defense, Washington Headquarters Services, Directorate for Information Operations and Reports (0704-0188), 1215 Jefferson Davis Highway, Suite 1204, Arlington, VA 22202-4302. Respondents should be aware that notwithstanding any other provision of law, no person shall be subject to any penalty for failing to comply with a collection of information if it does not display a currently valid OMB control number. **PLEASE DO NOT RETURN YOUR FORM TO THE ABOVE ADDRESS.**

<b>1. REPORT DATE</b> September 2017		<b>2. REPORT TYPE</b> Annual		<b>3. DATES COVERED</b> 1 Sep 2016 - 31 Aug 2017	
<b>4. TITLE AND SUBTITLE</b>  SERS Nanosensors for in vivo Glucose Sensing				<b>5a. CONTRACT NUMBER</b>	
				<b>5b. GRANT NUMBER</b> W81XWH-16-1-0375	
				<b>5c. PROGRAM ELEMENT NUMBER</b>	
<b>6. AUTHOR(S)</b>  Richard Van Duyne*, Anne-Isabelle Henry, Emma Vander Ende, Ji Eun Park, Michael McAnally  *email: vanduyne@northwestern.edu				<b>5d. PROJECT NUMBER</b>	
				<b>5e. TASK NUMBER</b>	
				<b>5f. WORK UNIT NUMBER</b>	
<b>7. PERFORMING ORGANIZATION NAME(S) AND ADDRESS(ES)</b>  Northwestern University Evanston, Illinois 60208-0001				<b>8. PERFORMING ORGANIZATION REPORT NUMBER</b>	
<b>9. SPONSORING / MONITORING AGENCY NAME(S) AND ADDRESS(ES)</b>  U.S. Army Medical Research and Materiel Command  Fort Detrick, Maryland 21702-5012				<b>10. SPONSOR/MONITOR'S ACRONYM(S)</b>	
				<b>11. SPONSOR/MONITOR'S REPORT NUMBER(S)</b>	
<b>12. DISTRIBUTION / AVAILABILITY STATEMENT</b>  Approved for Public Release; Distribution Unlimited					
<b>13. SUPPLEMENTARY NOTES</b>					
<b>14. ABSTRACT</b> The goal of this program is to develop of small and sensitive nanosensors for the continuous glucose monitoring in living tissue without the need for drawing blood. A major advantage of the transdermal sensors we are developing is to directly detect glucose itself – not the byproducts of its transformation. The technique we use – surface-enhanced Raman spectroscopy (SERS) – is based on light and informs on the presence of glucose on or nearby metallic nanosensors. In Year 1, we have worked on the development of i) sensitive nanosensors, ii) selective capture layers that can be immobilized onto metal surfaces, and iii) the integration of both. We have successfully developed a novel SERS nanoplatfrom that integrates gold nanorods with biocompatible hydrogels of variable stiffness. The fabrication of SERS-active microneedle patches has been successfully initiated and demonstrated over the first 12 months of the programs using stiff hydrogels. Several approaches have been taken and validated against SERS activity. Implementation of the glucose-capture layers in underway. We have shown that water-soluble molecules can diffuse through the hydrogel pores and be detected in the mM range, where glucose is physiologically relevant. These results are very promising regarding SERS-active transdermal patches.					
<b>15. SUBJECT TERMS</b> Glucose, diabetes, sensing, biosensing, boronic acid, SERS, Raman scattering, spectroscopy, hydrogel, microneedle array, continuous glucose monitoring, medical device					
<b>16. SECURITY CLASSIFICATION OF:</b>			<b>17. LIMITATION OF ABSTRACT</b>  Unclassified	<b>18. NUMBER OF PAGES</b>  58	<b>19a. NAME OF RESPONSIBLE PERSON</b> USAMRMC
<b>a. REPORT</b>  U	<b>b. ABSTRACT</b>  U	<b>c. THIS PAGE</b>  U			<b>19b. TELEPHONE NUMBER</b> (include area code)

## Table of Contents

	<u>Page</u>
<b>1. Introduction.....</b>	<b>5</b>
<b>2. Keywords.....</b>	<b>5</b>
<b>3. Accomplishments.....</b>	<b>5</b>
<b>4. Impact.....</b>	<b>20</b>
<b>5. Changes/Problems.....</b>	<b>20</b>
<b>6. Products.....</b>	<b>20</b>
<b>7. Participants &amp; Other Collaborating Organizations.....</b>	<b>22</b>
<b>8. Special Reporting Requirements.....</b>	<b>22</b>
<b>9. Appendices.....</b>	<b>24</b>

## 1. INTRODUCTION

Diabetes is a chronic disease in which levels of blood glucose – a small molecule that serves as an energy source – exceed the norm and pose a host of primary and secondary health complications. The goal of this program is to lighten the physical and psychological burden that daily blood glucose checks represent for patients and to improve their long-term health through the development of small and sensitive nanosensors that *continuously* detect and measure glucose in living tissue over a long period of time (several months) without the need for drawing blood. A major advantage of the transdermal sensors we are developing is to *directly* detect glucose itself – not the byproducts of glucose transformation - which require external reagents that add extra costs and steps, and which can respond to other molecules in the blood, such as fructose, leading to false inflation of measurements.

## 2. KEYWORDS

Glucose, diabetes, sensing, biosensing, boronic acid, SERS, Raman scattering, spectroscopy, hydrogel, microneedle array, continuous glucose monitoring, medical device

## 3. ACCOMPLISHMENTS

### **Major goals of the project**

As stated in the approved Statement of Work (SOW), the three major goals – or subtasks – of the first 12 months of this program were:

- 1- **Subtask 1: Nanosensors fabrication**, lead by Site 1 (Van Duyne lab).  
We proposed two designs: a metal film over nanospheres substrates that would be subcutaneously implanted, and a transdermal nanosensing patch that would be applied onto the skin.
- 2- **Subtask 2: Glucose capture layer synthesis**, lead by Site 2 (Mrksich lab).  
We proposed a boronic acid-based glucose capture layer. Several molecular designs are being investigated and evaluated for their efficiency to bind glucose.
- 3- **Subtask 3: Nanosensors functionalization with capture layers**, carried out by both Sites 1 and 2 (Van Duyne and Mrksich labs).  
This task consists in integrating the glucose capture layers to the nanosensors and evaluate the functionality of the whole nanosensing platform using surface-enhanced Raman spectroscopy (SERS)

### **Major activities accomplished under these goals in Months 1-12**

#### **SUBTASK 1: NANOSENSORS FABRICATION**

##### **1- Metal film over nanospheres (FONs) substrates**

Metal film over nanospheres (FONs) substrates are nanostructured metallic surfaces exhibiting high SERS performance (i.e., enhancing Raman signals by a factor of  $10^7$  or higher) with the advantage of being easily functionalized, thus serving as a great sensing platform and an ideal one for testing new functionalization layers.



FONs are typically made by evaporating silver or gold onto a hexagonal close packed array of silica spheres (~300-600 nm in diameter) either using thermal evaporation or physical vapor deposition. While the SERS performance – evaluated by measuring its enhancement factor (EF) – for these substrates is very good even over large areas, relatively little is known about the structure-performance relationship in these substrates.

To address this critical aspect of rational SERS sensor engineering at the nanoscale, the **Van Duyne lab** has investigated the interrelationship between structure (using scanning electron microscopy - SEM), far-field optical property (i.e., localized surface plasmon resonance (LSPR) spectroscopy) and near-field optical property (i.e., SERS)

Depending on the fabrication method (stationary vs. spinning metal deposition, designated as ST-FONs and SP-FONs, respectively), we clearly confirmed by SEM analysis that it is possible to control the fine morphology of the metal film in the 10–90 nm range, with the resulting nanofeatures differing in their shape and size dispersity. Using wavelength-scan surface-enhanced Raman excitation spectroscopy (WS-SERES), we directly measured the near-field SERS enhancement profile of both ST-FONs and SP-FONs and clearly showed that the near- and far-field profiles of SP-FONs were spectrally aligned, whereas a ~ 45 nm spectral shift was observed in the case of ST-FONs. The extensive numerical analysis revealed that the presence of nanofeatures with small size polydispersity results in the spectral alignment of optical far-field and near-field profiles. The absence of a commonly observed, near- to far-field spectral shift is attributed to a significant increase in the radiative damping originating from the surface morphology of the FONs.

In conclusion, we have shown that by controlling the FONs fabrication methodology through the metal evaporation conditions, it is possible to predict the SERS performance of the FONs substrates through the wavelength at which the maximum EF will occur. These findings were published this year in The Journal of Physical Chemistry C (Kurouski et al.).<sup>1</sup>

## 2- Microneedles arrays

### a. State of the art and rationale for design selection

One of the sensing platforms we are developing is a SERS-active microneedle array for a transdermal sensor capable of continuous glucose monitoring (CGM). Here we outline some of the basic structural parameters that dictate the effectiveness of such a sensor.

The most important feature is its **optical transparency** at the wavelength of the SERS excitation in the 700-800 nm region of the visible-NIR spectrum. These wavelengths of light penetrate human skin and enable Raman scattered light to be detected. Additionally, the transdermal patch requires a **robust design** so that both the structural integrity and functionality of the sensor are not compromised during penetration through skin. Once the patch is applied onto the skin, the biosensor needs to be mechanically and chemically **stable** throughout the continuous monitoring time period and remain functional over several weeks and months. The transdermal patch will serve as the biosensing component by evaluating the glucose level in the interstitial fluid. Therefore, optimizing the **depth of the microneedles** in direct contact with the epidermis is critical to target the fluid and avoid blood capillaries. As a result, we plan to fabricate microneedles with a maximum length of 600  $\mu\text{m}$ , ideally ~400  $\mu\text{m}$ . This will minimize the contamination risk of the

microneedles with blood-borne proteins, which may aggravate biofouling of the sensor, and also minimize pain by avoiding contact with nerves beneath the epidermis.

The **Mrksich lab** has fabricated polymer-based solid microneedles, taking into consideration all the pre-requisites outlined above. We have used a replica molding technique where the transdermal patch was shaped within an elastomeric mold (polydimethylsiloxane, PDMS) enabling reproducible fabrication of the patches. Two commercially available PDMS molds were purchased for the initial testing of polymer materials. The mold from Micropoint Technologies PTE Ltd has pyramidal features measuring 300  $\mu\text{m}$  in depth, 200  $\mu\text{m}$  in width, and spaced by a 500  $\mu\text{m}$  tip-to-tip distance. The second mold, from Blueacre Technology, has conical features measuring 300  $\mu\text{m}$  in depth, 300  $\mu\text{m}$  in width, and spaced by a 600  $\mu\text{m}$  tip-to-tip distance.

In addition to the structural requirements of a microneedle transdermal sensor, it must incorporate plasmonic materials to enhance the Raman scattering signal and be considered SERS-active. Thus, following the microneedle preparation, the transdermal biosensors were functionalized with SERS-active Au nanorods (AuNRs) that were synthesized in the **Van Duyne group**. There are two possible ways to incorporate the SERS active component with the transdermal patch: (i) functionalizing the microneedle surface with AuNRs, and (ii) embedding the AuNRs within the microneedles.

We are pursuing these two approaches by working with two different polymer types. The first approach requires the use of rigid polymers that do not swell in water. This allows us to locate AuNRs from the aqueous suspension solution on the microneedle surface. The second approach requires SERS active components densely distributed within the polymer matrix that must also be porous to allow glucose diffusion into the matrix. We have fabricated such microneedles using hydrogel-based materials. The selection of the hydrogel material relies on the mechanical robustness (to penetrate skin), porosity (for diffusion), biocompatibility, and optical characteristics of the solidified hydrogel.

## **b. Solid Microneedles SERS Biosensors using Rigid Polymers**

NOA (Norland Optical Adhesive) is a generic name for commercially available one-part adhesive liquids that can be cured under UV light exposure at room temperature. The composition of NOA products is protected by a commercial patent, but some studies report the constituents of NOA65,<sup>2-4</sup> which is a mixture of trimethylolpropane diallyl ether, trimethylolpropane trithiol, isophorone diisocyanate ester and benzophenone as the photoinitiator. Based on the major constituents being aliphatic, the Raman fingerprint of NOA materials are not expected to interfere with the Raman signals originating from the aromatic structure of the glucose capture ligand.

NOA materials are optically transparent which makes them a good candidate for transdermal biosensors. Once photocured, they form mechanically robust structures with modulus values up to 1 GPa. Three different versions of NOAs were chosen for fabricating the rigid polymer-based microneedles: NOA 61, NOA 65, and NOA 68. **Table 1** summarizes some of the characteristics of the NOA products that were used to prepare microneedle patches.

	NOA 61	NOA 65	NOA 68
Composition	Mercapto ester (30-50 %) Triallyl isocyanurate (30-55 %)	Mercapto ester (30-50 %) Mercapto ester (30-55 %)	Mercapto ester (30-50 %) Mercapto ester (35-60 %) Tetrahydrofurfuryl methacrylate (15-25 %)
Viscosity at 25C (cps)	300	1200	5000
Refractive Index (cured polymer)	1.56	1.524	1.54
Modulus of Elasticity (GPa)	1.03	0.14	0.14
Elongation at Failure (%)	38	80	80

**Table 1. Selected NOA products with corresponding chemical, physical and mechanical properties.** Listed information provided by the supplier (Norland Products).

In brief, NOA microneedle arrays are prepared by filling the aforementioned PDMS molds with NOA, removing air bubbles by gentle vacuum, and curing the polymer by UV exposure. The solidified array is then removed from the mold. Scanning electron microscopy (SEM) images of the resultant pyramidal and conical microneedle are shown in **Figure 1**. The pyramidal needles are uniform across large areas. However, the conical mold was more difficult to fill with NOA, and resulted in defective or missing tips. These experiments served to inform which mold needle shape best operates with the NOA materials.

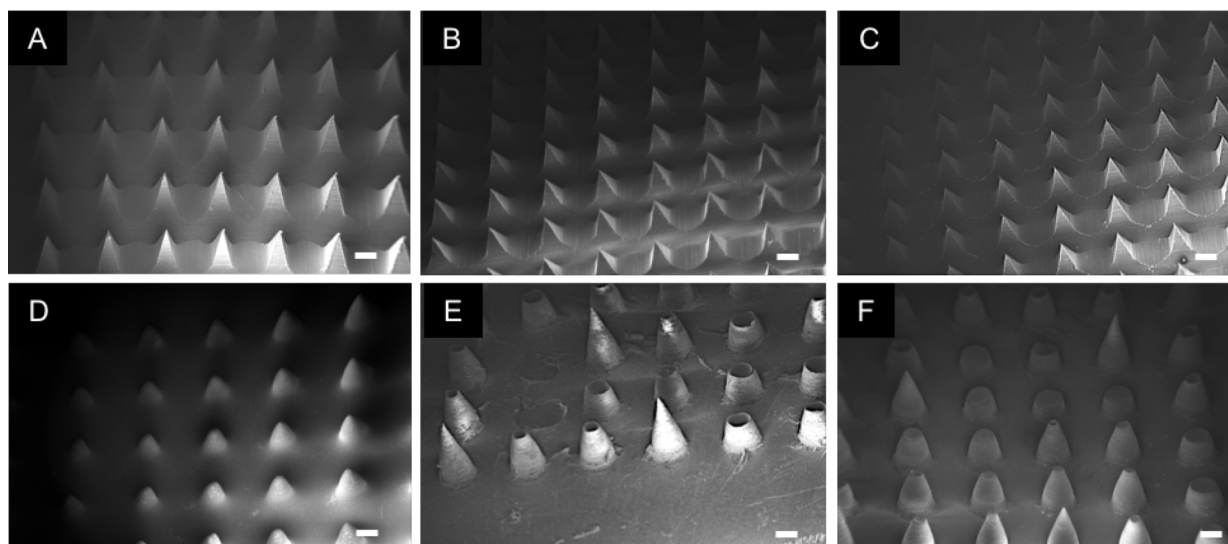


**Figure 1. SEM micrographs of pyramidal and conical NOA microneedles.** Materials made by using (A, D) NOA 61, (B, E) NOA 65 and (C, F) NOA 68. Scale bars: 200  $\mu$ m

The next step for the biosensor preparation was the assembly of the SERS active component, AuNRs synthesized in the **Van Duyne lab**, on the microneedles surface. The AuNRs are stabilized with a cetyltrimethylammonium bromide (CTAB) bilayer in aqueous solution. The physisorbed CTAB bilayer on the Au surface limits the particle-microneedle surface interactions due to a stronger particle-particle interaction. Therefore, the electrostatic attraction between particles must be overcome to bring the particles closer to the surface in favor of subsequent particle deposition. This can be done by adjusting the ionic strength of the suspension solution. We centrifuged the

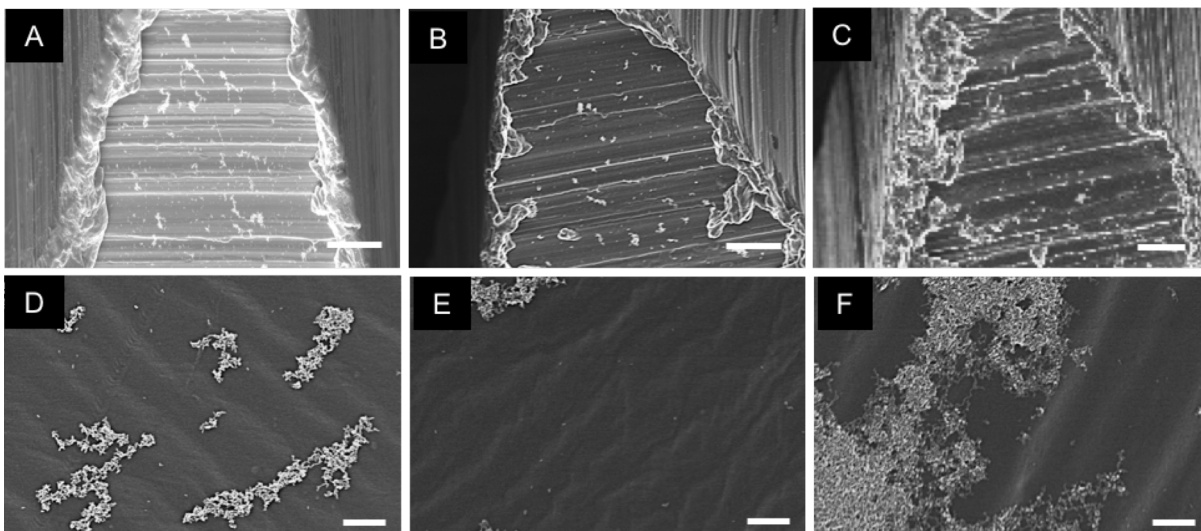


**Figure 2. SEM micrographs of Au nanorods assemblies on NOA microneedles and flat films using** (a, d) NOA 61, (b, e) NOA 65, and (c, f) NOA 68. Scale bars in (a, b, and c) are 10  $\mu\text{m}$ . Scale bars in (d, e, and f) are 1  $\mu\text{m}$ .

AuNRs suspension to remove the excess CTAB from the solution prior to re-suspending the AuNRs in a 5 mM NaCl aqueous solution. The NOA microneedles or flat NOA films (as a control) were then immersed in this particle suspension right after preparation. After incubating at room temperature for 2 hours, the samples were washed with deionized water to remove excess AuNRs. Investigation of the surface characterization for these samples by SEM revealed that AuNRs form large aggregates rather than individual AuNR monolayers on the NOA surface (**Figure 2**).

Raman scattering enhancement is highest when the excitation wavelength (785 nm) overlaps with the extinction maximum of the plasmonic material. The AuNRs synthesized by the **Van Duyne lab** for this project were optimized to have a solution-phase extinction maximum of  $\sim 783$  nm. However, this extinction maximum reflects the ensemble monomer spectrum in solution. Introduction of NaCl salt facilitated the AuNR assembly on both NOA microneedle surface and flat films, but there is evidence that doing so negatively affects the AuNR distribution on the surface.

AuNRs on the flat NOA surface demonstrated a quite different extinction spectrum than the characteristic plasmon bands in solution; two peaks were observed at 765 nm and 509 nm (**Figure 3**). This result may be caused by sedimenting pre-aggregated particles rather than individual particles on the surface and leading to extinction of larger aggregates at longer wavelengths.

We expect the AuNRs to self-assemble as an individual monolayer if the NOA surface charge is modified, rather than introducing a solution-phase charge (NaCl). Subsequently, NOA surfaces were treated with oxygen plasma prior to incubation with AuNR solution. As shown in **Figures 3 and 4**, plasma treatment on the NOA film significantly promoted the monolayer particle assembly as implied by an absorption peak in the 700-800 nm region. According to the surface images and the UV-Vis extinction peak intensity, we also investigated a change in the density of the AuNRs in the monolayer when different versions of NOAs were used. We concluded that AuNRs assembly on the plasma treated NOA 61 and NOA 65 surfaces will give the maximum SERS activity among the studied NOA forms for detecting the Raman signals and subsequent glucose sensing.

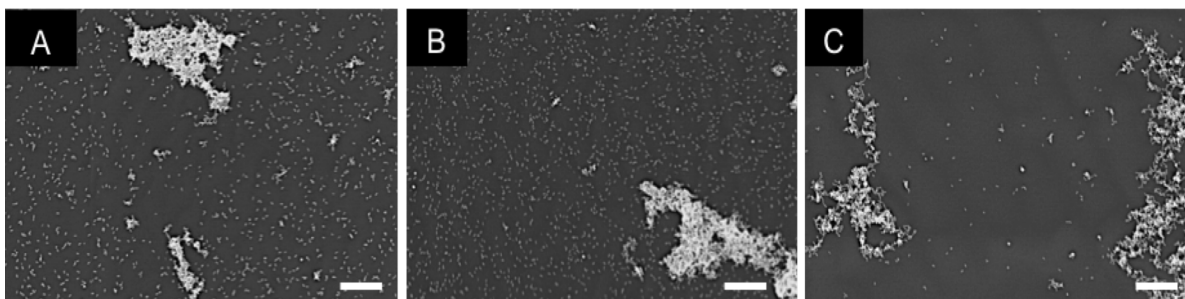


**Figure 4. Structural characterization of plasmonic NOA surfaces.** SEM micrographs of Au nanorods assembly on plasma treated flat NOA films using (a) NOA 61, (b) NOA 65, and (c) NOA 68. Scale bars are 1  $\mu\text{m}$ .

We also have evaluated the option to directly evaporate metal on the polymer rather than grafting AuNRs onto the surface. We deposited Au over the NOA microneedles using physical vapor deposition. Three different thicknesses of Au (40, 70, and 100 nm) were deposited to initially optimize the optical transparency, rigidity, and SERS enhancement at 785 nm. We confirmed the SERS activity (shown in Subtask 2, section 2) of the Au-covered microneedle array, shown in **Figure 5**.

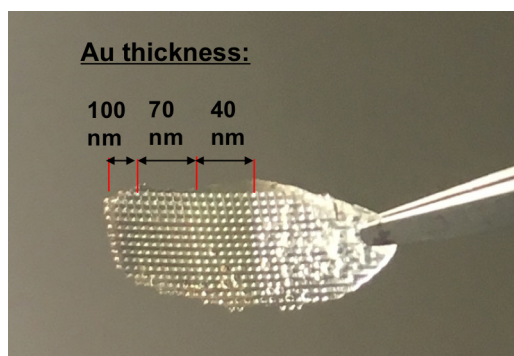


**Figure 5. Picture of a metallized microneedle array.** Au was deposited by physical layer deposition (PVD) with different thicknesses, as indicated on the image.

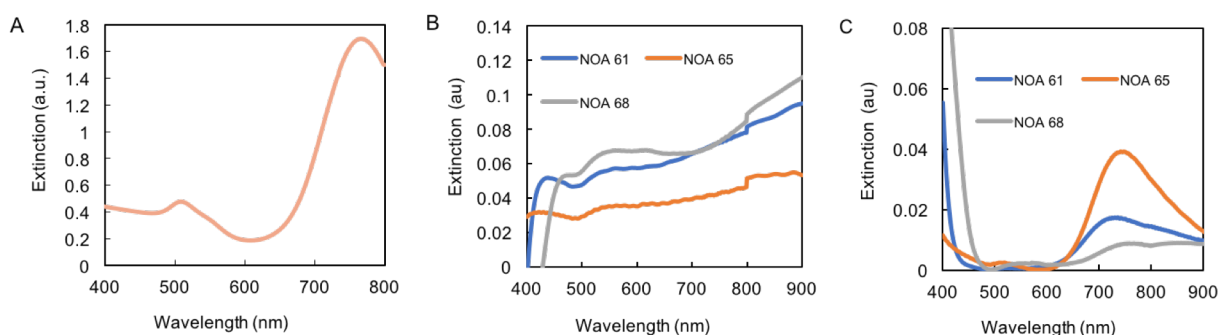


**Figure 3. Optical characterization of plasmonic NOA surfaces.** UV-Vis absorption spectra of Au nanorods (a) in solution, (b) on the flat, and (c) plasma treated flat NOA surfaces.

### c. SERS-active hydrogels approach

#### i. Soft hydrogel-based SERS biosensors

Hydrogel-based microneedles have mostly been used as drug delivery devices due to their biodegradation and tendency to swell in water. Our motivation for using the hydrogels in microneedles form relies on their capacity to extract interstitial fluid by diffusion through pores, thus enabling *in situ* biosensing once the SERS active component is incorporated.

We first tested the feasibility of using polyacrylamide (PAM) as a scaffold for plasmonic patches. AuNRs were incorporated in PAM prior to polymerization. The successful embedding of AuNRs in PAM was qualitatively confirmed by dark-field scattering as shown on the image in **Figure 6A** where the metal nanoparticle aggregates appear white. Then, the SERS activity of AuNRs in the hydrogel was confirmed using a model water-soluble molecule, 4-mercaptobenzoic acid (4-MBA). As shown in **Figure 6B**, SERS of 4-MBA is only observed when AuNRs are incorporated into the hydrogel. This result confirmed that 4-MBA diffuses through the hydrogel pores and adsorbs to AuNRs embedded in the hydrogel, which is already formed before exposure to 4-MBA.

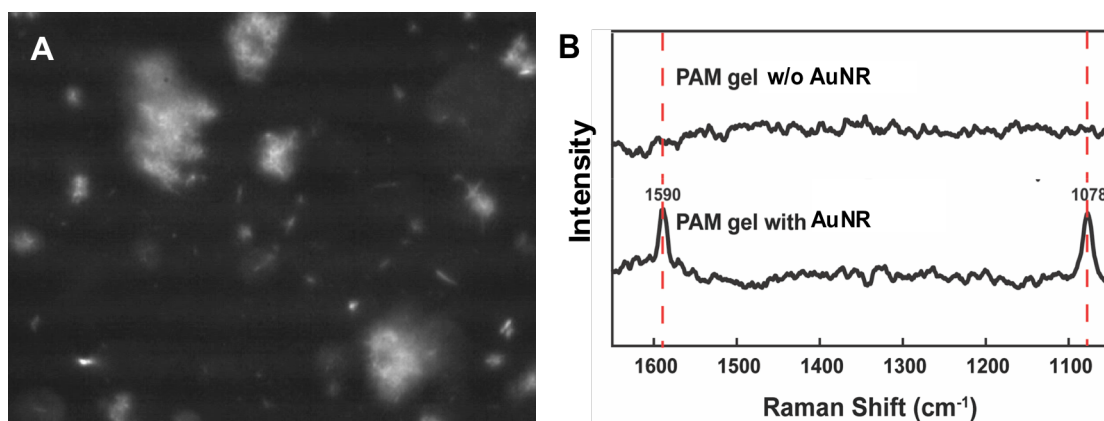


**Figure 6. SERS-active hydrogel made with PAM.** A) Dark-field scattering image of PEG hydrogel with AuNRs B) SERS spectra of PEG hydrogel with and without AuNRs with 4-MBA (Average of seven spectra using 20x ELWD objective,  $P_{\text{ex}} = 500 \mu\text{W}$ ,  $\lambda_{\text{ex}} = 785 \text{ nm}$ , Savitsky-Golay filtering and baseline correction).

PAM was a useful polymer for us to start with to confirm analyte detection with the AuNRs embedded within the hydrogel. However, the limited stiffness (maximum 1 MPa)<sup>6</sup> of PAM makes it unsuitable for the fabrication of microneedles capable of piercing human skin. For an actual sensor, the microneedle design must use a hydrogel with high ( $\sim \text{GPa}$  range) stiffness.

Based on literature results showing that microneedles made with poly(ethylene glycol) (PEG) effectively pierced mouse skin *ex vivo*,<sup>7</sup> we selected PEG as our polymer of choice for stiff, transparent, and biocompatible microneedle transdermal patches. Similar to the PAM hydrogel preparation, AuNRs were added to the polymer precursors and then photopolymerized to produce PEG hydrogels loaded with AuNRs. Again, AuNRs were successfully embedded in PEG hydrogels as seen by dark-field scattering (**Figure 7A**). SERS activity of the plasmonic PEG hydrogels was confirmed after incubation in 1 mM 4-MBA and compared against a control sample (PEG hydrogel only, without AuNRs, and incubated in 4-MBA) (**Figure 7B**, black spectrum). Only the hydrogel with AuNRs (**Figure 6B**, red spectrum) showed the two dominant vibrational modes of 4-MBA. This result shows that 4-MBA can diffuse through the PEG hydrogel and adsorb onto AuNRs.



In conclusion, AuNRs were successfully integrated into a SERS-active PEG hydrogel. This proof-of-concept study will be taken forward to glucose sensing by functionalizing AuNRs with glucose capture ligands and detecting glucose diffused through PEG hydrogel. This is a promising result where water-soluble molecules can diffuse through the hydrogel pores and be detected in the mM range, where glucose is physiologically relevant.

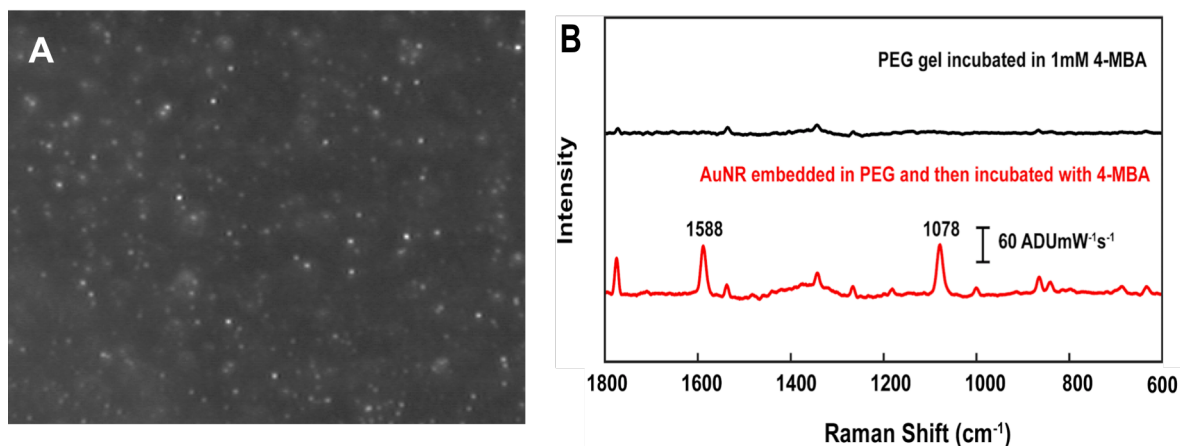


**Figure 7. SERS-active hydrogel made with PEG.** A) Dark-field scattering image of a PEG hydrogel with AuNRs B) SERS spectrum PEG hydrogel: black) without AuNRs incubated in 1 mM 4-MBA, red) with AuNRs embedded in hydrogel initially and incubated in 1mM 4-MBA (Average of seven spectra using a 20x ELWD objective,  $P_{\text{ex}} = 620 \mu\text{W}$ ,  $\lambda_{\text{ex}} = 785 \text{ nm}$ , Savitsky-Golay filtering and baseline correction).

## ii. Solid hydrogel-based microneedles

Based on relevant biocompatibility studies in the literature, we have also worked with an acid anhydride copolymer containing alternating maleic anhydride and methyl vinyl ether groups. This material was purchased from International Specialty Products, NJ, under the tradename Gantrez AN-139. Gantrez is a non-toxic material<sup>9</sup> and exhibits antimicrobial properties when blended with PEG.<sup>10</sup> Donnelly et al. demonstrated various examples of Gantrez-PEG based microneedles for drug delivery and biosensing applications<sup>11-13</sup>.

We have focused on adapting the Gantrez-PEG blend chemistry to fabricate SERS active transdermal patches for glucose sensing. Incorporation of SERS active components, Au nanorods, as embedded within the polymer matrix was achieved by an easy particle dispersion in the pre-polymer solution and subsequent solidification of the matrix at elevated temperature (80 °C). The microneedles were fabricated by casting the pre-polymer solution on the PDMS mold and solidifying within the mold at high temperature (**Figure 8A**). The flat films were prepared on the flat surface. As the water content evaporates, carboxyl groups on the Gantrez and hydroxyl groups on the PEG chains goes through esterification reaction and finally the polymer matrix solidifies. The resulting patch became very rigid and the AuNRs assembly within the matrix exhibited light absorption features in the target 700-800 nm region (**Figure 8B**). More detailed characterization of both mechanical properties and biocompatibility are in progress to provide a comprehensive evaluation of the hydrogel-based microneedles.

In conclusion, the fabrication of SERS-active microneedle patches has been successfully initiated and demonstrated over the first 12 months of the programs. Several approaches have been taken and validated against SERS activity. Implementation of the glucose-capture layers is underway, as described in more details in Subtask 3.

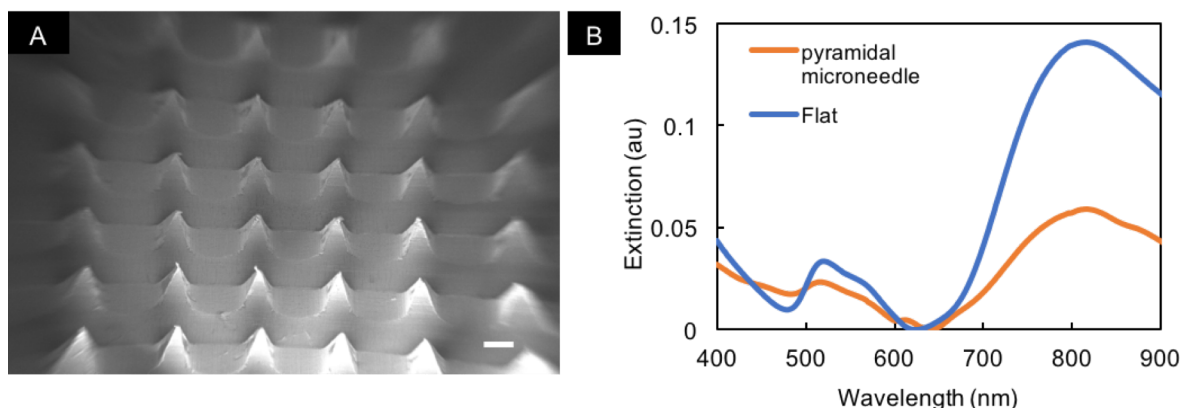


**Figure 8. Characterization of solid plasmonic-PEG microneedles.** A) SEM micrograph of Gantrez-PEG pyramidal microneedles. Scale bar is 200  $\mu\text{m}$ . B) UV-vis extinction spectra of Au nanorods assembly embedded in the Gantrez-PEG hydrogel with pyramidal microneedles and flat film.

## SUBTASK 2: GLUCOSE CAPTURE LAYER SYNTHESIS

### 1. Bisboronic acid synthesis and product quality check

Over this first year we began an in-depth characterization of the bisboronic acid glucose capture layer reported in our 2016 publication(cite). Additionally, we have implemented a quality check protocol to ensure high synthetic batch-to-batch reproducibility.

After synthesizing 1,1-bisboronic acid (1,1-BBA) in the **Mrksich lab**, its binding constant ( $K$ ) with glucose was evaluated in PBS buffer (pH 7.4) as a systematic quality check in the **Van Duyne lab**. To determine the  $K$ , a UV-vis titration study was done by varying the concentration of glucose (0-1000 mM) at a constant 1,1-BBA concentration. Two absorbance peaks of 1,1-BBA (206 and 245 nm) are observable in the UV region (**Figure 9A**). As the concentration of glucose increased there was a blue shift for the peak at 245 nm and the signal intensity decreased. The resulting data was fitted to a Langmuir isotherm model (**Figure 9B**) and the binding constant of 1,1-BBA in PBS buffer determined to be  $158 \text{ M}^{-1}$ . For comparison, the binding constant of 4-mercaptophenylboronic acid (4-MPBA), a commonly used monoboronic acid used to bind glucose, was determined to be around only  $50 \text{ M}^{-1}$ .

In addition to UV-vis titrations, normal Raman spectra of each batch of 1,1-BBA were collected to ensure that each batch was molecularly identical. Following these checks, 1,1-BBA was used to functionalize SERS-active substrates for glucose sensing.



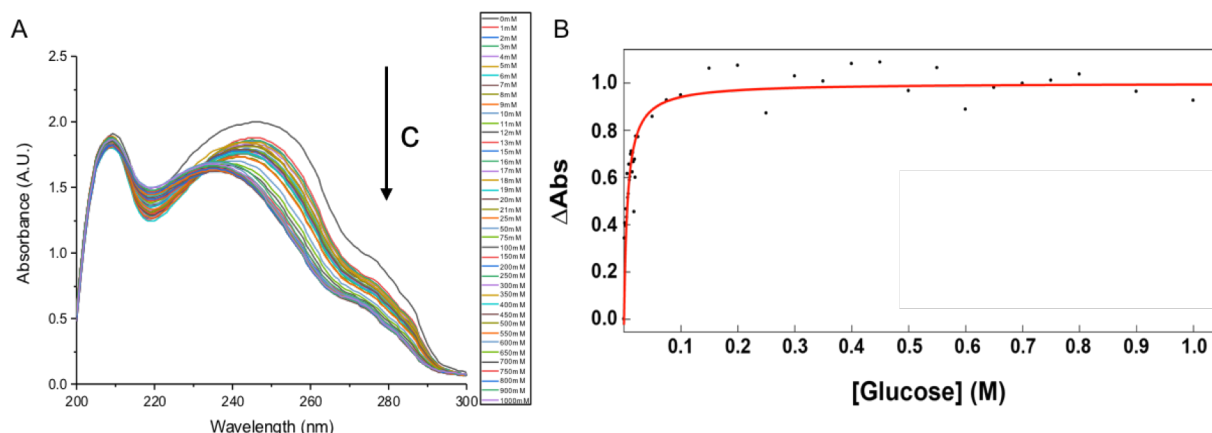


**Figure 9. Confirmation of glucose binding to 1,1-BBA by UV-vis spectroscopy.** (A). UV-vis spectra of the concentration dependent binding of 1,1-BBA with glucose in 10% MeOH/PBS at pH 7.4, B) Langmuir isotherm of 1,1-BBA binding interaction with glucose.

With the synthesis of these capture layers established on a small scale (~ 10 mg), the **Mrksich lab** has taken advantage of ChemCore, a chemical synthesis service at Northwestern University, to obtain larger amounts (100 mg - 1 g) on a routine basis in order to devote more time to developing even better capture molecules. This larger scale is sufficient for transitioning the focus of the project from material development to sensor implementation in parallel with capture molecule development.

## 2. Monoboronic acids modification

The following monoboronic acid derivatives (**Figure 10**) are currently being synthesized in the **Mrksich lab** as trial compounds for optimizing our glucose sensing platform. The parameters we wish to optimize are the binding constant and selectivity over fructose. Each of these derivatives retains the electron-withdrawing fluorine group of 1,1-BBA that allows for sensing of glucose at physiological pH.

By minimizing the distance between the boronic acid receptor and the surface-binding thiol, we can maximize the Raman signal enhancement, which is distance dependent. Additionally, the pinacol boronic ester glucose duplex (**Figure 10A**) should enable direct detection of glucose Raman peaks, which will serve as a reference for directly detecting glucose using shorter capture agents (**Figure 10B and C**).

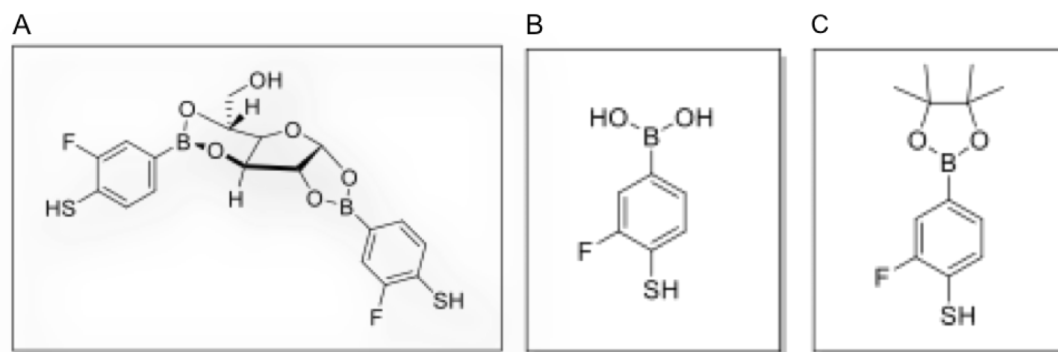


**Figure 10. Monoboronic acid derivatives** identified as alternative capture layers to bisboronic acids.

### SUBTASK 3: NANOSENSORS FUNCTIONALIZATION WITH CAPTURE LAYERS

#### 1. AuNRs/AuFONs functionalization and SERS data

##### a. Performance evaluation for SERS substrates

As mentioned in Subtasks 1 and 2, AuFONs and AuNRs are the two plasmonic substrates used in our SERS nanosensors. Both are highly robust and reproducible substrates with high enhancing capabilities whose fabrication production can be scaled up for large distribution. Importantly, the surface chemistry of both AuFONs and AuNRs can be easily tuned by functionalizing the surface with different ligands, making them ideal SERS substrates for biosensing and subsequent functionalization with anti-biofouling layers.

AuNRs and AuFONs were both fabricated so that their localized surface plasmon resonance (LSPR), or extinction maximum, were optimized for 785 nm excitation wavelength through tuning of metal thickness and underlying microspheres diameter (for AuFONs) and aspect ratio (AuNRs,  $\sim 45$  nm by 15 nm).

The SERS activity of the AuNRs was confirmed in the **Van Duyne lab** by functionalizing the surface with a water-soluble Raman reporter, 4-MBA, and subsequently measuring the SERS spectrum with a 785 nm excitation wavelength (**Figure 11**). The peaks observed on the SERS spectrum at 1078 and 1590  $\text{cm}^{-1}$  represent the two dominant ring vibrational modes of 4-MBA. The average enhancement factor (EF) of the 785-nm optimized AuNRs was calculated to be  $4 \times 10^4$ .

Although lower than that of AuFONs, the EF can be increased by aggregating nanorods into dimers and trimers, creating electromagnetic hotspots known to considerably boost the SERS signal.<sup>9</sup> We are therefore pursuing controlling the aggregation of nanorods when deposited onto microneedles patches, both in solid microneedles and hydrogel approaches. The SERS activity was confirmed using 1,2-bis(2-pyridyl)ethylene (BPE), a non-resonant Raman reporter molecule commonly used in the **Van Duyne lab** to confirm the SERS activity of plasmonic substrates.

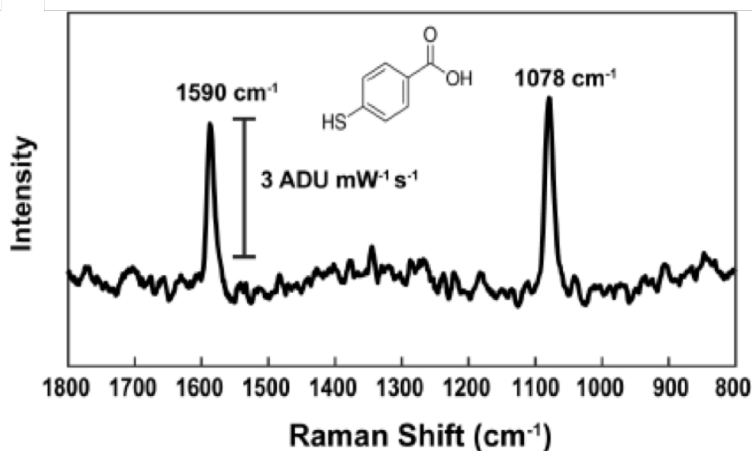


**Figure 11. Confirmation of SERS activity by AuNRs used as plasmonic nanosensors.** SERS spectrum of 4-MBA on AuNRs (20x ELWD objective,  $\lambda_{\text{ex}} = 785$  nm, Savitsky-Golay filtering and baseline correction).

## b. Glucose cross-section measurements

The importance of glucose in metabolic disorders has led to many researchers attempting to quantify glucose concentration *in vivo* using Raman scattering techniques, including by stimulated Raman scattering (SRS) microscopy. As normal Raman scattering (NRS) studies of glucose showed very weak scattering, surface-enhanced Raman scattering (SERS) and coherent Raman scattering techniques were used to enhance the low overall NRS signal (**Figure 12**). Unfortunately, previous research either cites a literature value of the differential Raman scattering cross-section (DRSC) that references unpublished and non-peer reviewed data for the DRSC of the 1126  $\text{cm}^{-1}$  mode of glucose, or simply omits the exact value.

To resolve this issue, we utilized femtosecond stimulated Raman scattering (FSRS) to quantitatively determine its DSRCs using both stimulated Raman loss (SRL) and stimulated Raman gain (SRG) simultaneously (**Figure 12**). Using the two analogous FSRS techniques, SRG and SRL, we determine that the DSRCs of glucose excited at 514.5 nm range from a low of  $5.0 \pm 1.1 \times 10^{-30}$  to a high of  $8.9 \pm 0.9 \times 10^{-30} \text{ cm}^2 \text{ molecule}^{-1} \text{ sr}^{-1}$ .

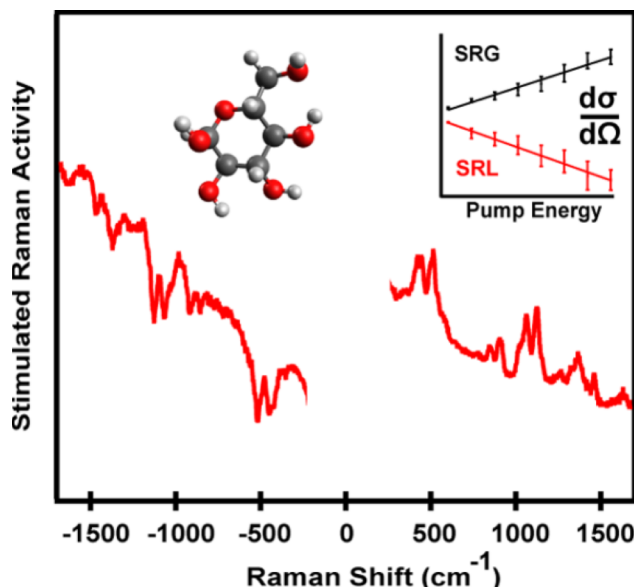


**Figure 12. Determination of glucose Raman section.** The DRSC of multiple vibrational modes of glucose was determined for the first time using FSRS. In the FSRS approach, SRL and SRG spectra were obtained simultaneously, then a linear regression was performed on the pump energy dependent stimulated Raman activity.

Based on this measurement, we can confidently evaluate the DRSC for 1124  $\text{cm}^{-1}$  mode of glucose at 785 nm excitation to be  $\sim 1.05 \times 10^{-30} \text{ cm}^2 \cdot \text{molecule}^{-1} \cdot \text{sr}^{-1}$ . This work established both the compatibility of SRL for measuring DRSCs and values for the DRSC of multiple vibrational modes of glucose, something of direct interest to the PRMRP effort. These results were published earlier this year by McAnally et al. in *Analytical Chemistry*.<sup>14</sup>

### c. Microneedles array – SERS data

Plasmonic polymers consisting of AuNRs in NOA microneedles or flat films were incubated in a concentrated solution capture ligand. The CTAB bilayer on the nanorods was replaced with the capture ligand and immobilization through S-Au binding. NOA samples are then immersed in a buffer solution to saturate the surface with the working buffer condition. Varied concentrations of glucose were used to study the glucose sensing capability of the capture ligand. After incubating the microneedle samples in the glucose solution, SERS spectra were collected.

NOA microneedles metallized with Au films were incubated in a concentrated solution of glucose capture ligand 4-MPBA so that the SERS substrate surface was decorated with 4-MPBA. 4-MPBA was used to detect glucose since it is the simplest phenylboronic glucose capture ligand that is known to bind glucose. With a thiol group present in the molecule, 4-MPBA readily forms self-assembled monolayers on the SERS-active metal surface.

As shown in **Figure 13**, SERS spectra were obtained from NOA microneedles with three different thicknesses of Au (40, 70, and 100 nm). SERS spectrum of bare NOA microneedles (no Au film) was taken to evaluate potential background signals of NOA that may overlap with the SERS signals from 4-MPBA. No NOA SERS signals were found to potentially interfere with SERS signals of 4-MPBA. With the highest SERS intensity of 4-MPBA and highest degree of optical transparency, NOA microneedles with a 40 nm-thick Au film were found to be best among the three thicknesses for detecting glucose.

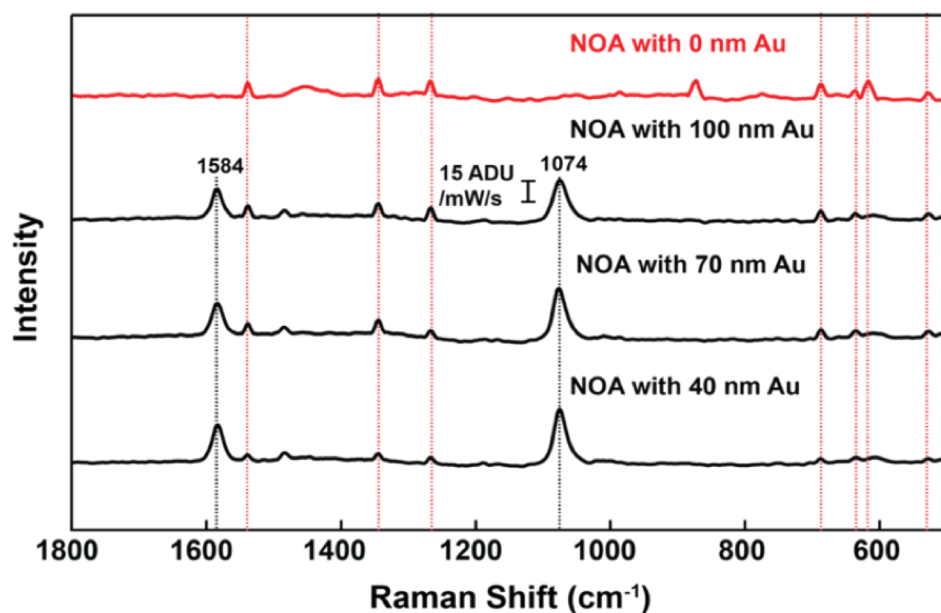


**Figure 13. SERS activity of metallized microneedles array.** SERS spectra of NOA microneedles with different thicknesses of Au (0, 40, 70, 100 nm) (20x ELWD objective,  $\lambda_{\text{ex}} = 785 \text{ nm}$ ,  $P_{\text{ex}} = 278 \mu\text{W}$ , Savitsky-Golay filtering and baseline correction).

The  $\text{pK}_a$  value of 4-MPBA is around 9 and the ideal pH to detect glucose should be basic condition (pH 9 or higher). SERS spectra were taken with the microneedles incubated in pH 10 buffer and then in 10 mM glucose solution (pH 10). The resulting SERS spectra (**Figure 14**) shows that the dominant peaks of 4-MPBA at 1074 and 1584  $\text{cm}^{-1}$  did not shift upon glucose addition, but the

peak intensities of both peaks increased when glucose was added. This is consistent with literature results in which only the SERS signal intensities changed upon glucose binding to 4-MPBA.<sup>3,8</sup> To further investigate the detection of glucose with 4-MPBA, experiments will be done at various concentrations to observe the intensity changes and correlate these to glucose concentration. This is a promising result in that these SERS-active NOA microneedles show potential as transdermal glucose nanosensors.

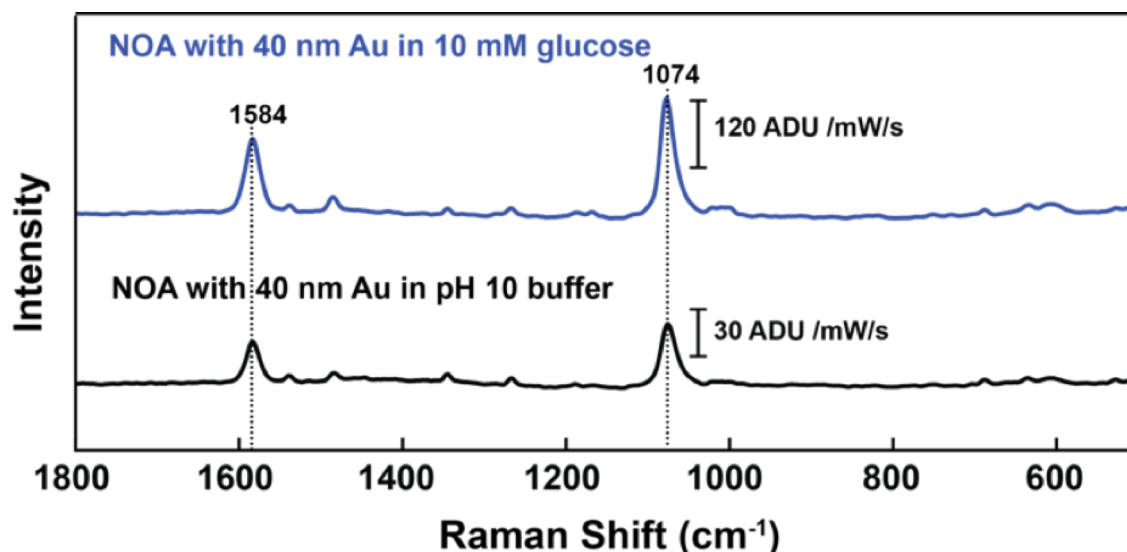


**Figure 14. SERS activity of plasmonic microneedles array.** SERS spectra of NOA microneedles with and without 10 mM glucose in pH 10 buffer (20x ELWD objective,  $\lambda_{\text{ex}} = 785 \text{ nm}$ ,  $P_{\text{ex}} = 278 \text{ } \mu\text{W}$ , Savitsky-Golay filtering and baseline correction).

## References

1. D. Kurouski, N. Large, N. Chiang, A.-I. Henry, T. Seideman, G. C. Schatz and R. P. Van Duyne, *The Journal of Physical Chemistry C*, 2017, **121**, 14737-14744.
2. G. W. Smith, *Phys Rev Lett*, 1993, **70**, 198-201.
3. T. Kyu and D. Nwabunma, *Macromolecules*, 2001, **34**, 9168-9172.
4. B. Pinto-Iguanero, A. Olivares-Perez and I. Fuentes-Tapia, *Opt Mater*, 2002, **20**, 225-232.
5. B. Nikoobakht and M. A. El-Sayed, *Chem Mater*, 2003, **15**, 1957-1962.
6. C. K. Tsung, X. S. Kou, Q. H. Shi, J. P. Zhang, M. H. Yeung, J. F. Wang and G. D. Stucky, *J Am Chem Soc*, 2006, **128**, 5352-5353.
7. M. Dasog and R. W. J. Scott, *Langmuir*, 2007, **23**, 3381-3387.
8. A. R. Ferhan, L. H. Guo and D. H. Kim, *Langmuir*, 2010, **26**, 12433-12442.
9. J. M. Irache, M. Huici, M. Konecny, S. Espuelas, M. A. Campanero and P. Arbos, *Molecules*, 2005, **10**, 126-145.
10. R. F. Donnelly, T. R. R. Singh, A. Z. Alkilani, M. T. C. McCrudden, S. O'Neill, C. O'Mahony, K. Armstrong, N. McLoone, P. Kole and A. D. Woolfson, *Int J Pharmaceut*, 2013, **451**, 76-91.

11. R. F. Donnelly, D. I. J. Morrow, M. T. C. McCrudden, A. Z. Alkilani, E. M. Vicente-Perez, C. O'Mahony, P. Gonzalez-Vazquez, P. A. McCarron and A. D. Woolfson, *Photochem Photobiol*, 2014, **90**, 641-647.
12. R. F. Donnelly, M. T. C. McCrudden, A. Z. Alkilani, E. Larraneta, E. McAlister, A. J. Courtenay, M. C. Kearney, T. R. R. Singh, H. O. McCarthy, V. L. Kett, E. Caffarel-Salvador, S. Al-Zahrani and A. D. Woolfson, *Plos One*, 2014, **9**.
13. G. R. C. Hamilton, L. Fullerton, B. McCaughan, R. F. Donnelly and J. F. Callan, *New J Chem*, 2014, **38**, 2823-2830.
14. M. O. McAnally, B. T. Phelan, R. M. Young, M. R. Wasielewski, G. C. Schatz and R. P. Van Duyne, *Analytical Chemistry*, 2017, **89**, 6931-6935.

### **Opportunities for training and professional development provided by the project**

Ji Eun Park joined the Van Duyne group in September 2016 as a second-year graduate student. She was trained in AuFONs fabrication, LSPR and SERS characterization, including EF measurement. She is now fully trained and operational for working independently in the lab on the experiments relevant to this program.

Other team members were already trained into their field of expertise.

Dr. Anne-Isabelle Henry was selected for an oral presentation at the National Spring 2017 meeting of the American Chemical Society (April 2-6, 2017) in San Francisco, CA. Her talk, entitled 'Towards SERS-enabled diagnostics: quantitative detection of glucose and other biomarkers', presented the results from the 1,1BBA-AuFON sensor published in September 2016 in the Journal of the American Chemical Society (Sharma et al. J. Am. Chem. Soc. 138, 13952-13959) by herself, Pradeep Bugga, Milan Mrksich, and Richard Van Duyne.

### **Dissemination of results to communities of interest**

Ji Eun Park took part in the 'All Scout Nanoday' outreach event organized by the International Institute for Nanotechnology and hosted in part by the Van Duyne lab. They engaged with a young audience (~10-14 year-old girl and boy scouts from the Chicago area) to communicate about nanotechnology research and careers in science.

### **Plan for the next reporting period towards accomplishing outlined goals**

The Van Duyne group will continue working on optimizing the plasmonic microneedle patches by varying the nanorods loading and evaluating the SERS performance of metallized microneedles through skin by differential SERS (d-SERS) using a newly purchased and tested dual-wavelength instrument acquired through this program. Data analysis regarding quantitative analysis of glucose concentration in 4-MPBA SERS spectra will be carried out. Evaluation of alternative capture layers on the SERS substrates will continue.

The Mrksich group will transfer the synthesis of a high glucose binding BBA (2,2-BBA) to the core synthesis facility at Northwestern. The synthesis of the alternative boronic acids described in Subtask 2 will be completed.

Both groups will keep working on evaluating glucose-capture layer binding in solution but most importantly on metal surfaces, as well as measuring SERS spectra and quantifying glucose concentration. Finally, the resulting SERS glucose nanosensors will be tested through skin and their

stability in biofluid evaluated.

#### 4. IMPACT

##### **Impact on the development of the principal discipline(s) of the project**

The development of plasmonically-active polymer platforms is new when applied to combining microneedles and SERS. As such, this an exciting new avenue unraveled by this project. Both groups are closely and actively pursuing the development of these new functional platforms. We anticipate publishing findings in at least one scientific publication over the next reporting period.

##### **Impact on other disciplines**

Nothing to Report.

##### **Impact on technology transfer**

Nothing to report

##### **Impact on society beyond science and technology**

Nothing to report

#### 5. CHANGES/PROBLEMS

##### **Changes in approach and reasons for change**

Nothing to report.

##### **Actual or anticipated problems or delays and actions or plans to resolve them**

Difficulties in reproducing previous data with 1,1-BBA has slowed down the project more than anticipated in the first months. We now have in place both methods and plans for quality control of capture ligands. We also actively pursue all reasonable options for short, thiolated glucose capture ligands, such as the three alternative boronic acids shown in Accomplishments/Subtask 2.

##### **Changes that had a significant impact on expenditures**

Nothing to report.

##### **Significant changes in use or care of human subjects, vertebrate animals, biohazards, and/or select agents**

Nothing to report.

#### 6. PRODUCTS

## **Publications, conference papers, and presentations**

### **▪ Journal publications**

List of peer-reviewed articles appearing in scientific journals, acknowledging federal support:

- 1- A.-I. Henry, T. W. Ueltschi, M. O. McAnally, and R. P. Van Duyne 'Surface-enhanced Raman spectroscopy: from single particle/molecule to angstrom-scale spatial resolution and femtosecond time resolution' Faraday Discuss. (2017) *accepted for publication*, DOI: 10.1039/c7fd00181a
- 2- D. Kourouski, N. Large, N. Chiang, A.-I. Henry, T. Seideman, G. C. Schatz, and R. P. Van Duyne 'Unraveling the near- and far-field relationship of 2D surface-enhanced Raman spectroscopy substrates using wavelength-scan surface-enhanced Raman excitation spectroscopy' J. Phys. Chem. C (2017), 121, 14737-14744.
- 3- M. O. McAnally, B. T. Phelan, R. M. Young, M. R. Wasielewski, G. C. Schatz, and R. P. Van Duyne 'Quantitative determination of the differential Raman scattering cross-sections of glucose by femtosecond stimulated Raman scattering' Anal. Chem. (2017) 89, 6931-6935.

### **▪ Books or other non-periodical, one-time publications**

Nothing to report.

### **▪ Other publications, conference papers, and presentations**

Presentations acknowledging this program:

- 1- Anne-Isabelle Henry 'Chemical identification at the nanoscale: basics and applications of surface-enhanced Raman spectroscopy (SERS)' Midwest Microscopy and Microanalysis Society; November 18, 2016, Deerfield, IL.
- 2- Anne-Isabelle Henry 'Towards SERS-enabled diagnostics: quantitative detection of glucose and other biomarkers' 253<sup>rd</sup> National Meeting of the American Chemical Society; April 2, 2017, San Francisco, CA.

### **▪ Website(s) or other Internet site(s)**

A brief description of the SERS-enabled biosensing efforts in the Van Duyne lab is provided on the group webpage:

<http://sites.northwestern.edu/vanduyne/research/sers-biosensing/>

Direct access to the pdfs of publications outlined above is also provided on the website:

<http://sites.northwestern.edu/vanduyne/publications/>

### **▪ Technologies or techniques**



Plasmonic microneedles described in Accomplishments/Subtasks 1 and 3 are technologies directly resulting from this program.

- **Inventions, patent applications, and/or licenses**

Nothing to report.

- **Other Products**

Nothing to report.

## 7. PARTICIPANTS AND OTHER COLLABORATING ORGANIZATIONS

### Individuals working on the project

Name:	<i>Ji Eun Park</i>
Project Role:	<i>Graduate Student</i>
Researcher Identifier (e.g. ORCID ID):	
Nearest person month worked:	<i>12</i>
Contribution to Project:	<i>Ms. Park has performed work on nanosensors fabrication and characterization by SERS</i>
Funding Support:	

Name:	<i>Emma Vander Ende</i>
Project Role:	<i>Graduate Student</i>
Researcher Identifier (e.g. ORCID ID):	
Nearest person month worked:	<i>6</i>
Contribution to Project:	<i>Ms. Vander Ende has performed work on nanosensors fabrication and characterization by SERS. She trained Ms. Park in AuFON fabrication, LSPR, and SERS, and provides experimental design and project development support.</i>
Funding Support:	<i>National Science Foundation Graduate Research Fellowship Program (DGE-132458)</i>

Name:	<i>Michael O. McAnally</i>
Project Role:	<i>Graduate Student</i>
Researcher Identifier (e.g. ORCID ID):	<i>0000-0002-8681-2952</i>
Nearest person month worked:	<i>3</i>
Contribution to Project:	<i>Mr. McAnally has performed work on glucose</i>

	<i>Raman cross-section measurement</i>
Funding Support:	<i>National Science Foundation Graduate Research Fellowship Program (DGE-082416)</i>

Name:	<i>Anne-Isabelle Henry</i>
Project Role:	<i>Research Assistant Professor</i>
Researcher Identifier (e.g. ORCID ID):	<i>0000-0003-1900-7416</i>
Nearest person month worked:	<i>12</i>
Contribution to Project:	<i>Dr. Henry has performed work on nanosensors and provided internal organizational support</i>
Funding Support:	

Name:	<i>Richard Van Duyne</i>
Project Role:	<i>Professor</i>
Researcher Identifier (e.g. ORCID ID):	<i>0000-0001-8861-2228</i>
Nearest person month worked:	<i>1.5</i>
Contribution to Project:	<i>Dr. Van Duyne has supervised work on nanosensors and advised on scientific direction</i>
Funding Support:	

Name:	<i>Pradeep Bugga</i>
Project Role:	<i>Graduate Student</i>
Researcher Identifier (e.g. ORCID ID):	
Nearest person month worked:	<i>12</i>
Contribution to Project:	<i>Mr. Bugga has performed work on the capture ligands synthesis</i>
Funding Support:	

Name:	<i>Daniel Sykora</i>
Project Role:	<i>Graduate Student</i>
Researcher Identifier (e.g. ORCID ID):	<i>0000-0002-5675-7454</i>
Nearest person month worked:	<i>1</i>
Contribution to Project:	<i>Mr. Sykora has performed work on the evaluation of protein reagent receptors.</i>
Funding Support:	

Name:	<i>Nihan Yonet-Tanyeri</i>
Project Role:	<i>Postdoctoral fellow</i>
Researcher Identifier (e.g. ORCID ID):	<i>0000-0003-3867-2200</i>
Nearest person month worked:	<i>6</i>
Contribution to Project:	<i>Dr. Yonet-Tanyeri has performed work on the polymer microneedle patches</i>
Funding Support:	

Name:	<i>Allen Yang</i>
Project Role:	<i>Research Technologist</i>
Researcher Identifier (e.g. ORCID ID):	<i>0000-0003-2003-5887</i>
Nearest person month worked:	<i>8</i>
Contribution to Project:	<i>Mr. Yang has performed work on functionalization materials with peptides and receptors</i>
Funding Support:	

Name:	<i>Milan Mrksich</i>
Project Role:	<i>Professor</i>
Researcher Identifier (e.g. ORCID ID):	<i>0000-0002-4964-796X</i>
Nearest person month worked:	<i>1.5</i>
Contribution to Project:	<i>Dr. Mrksich has overviewed work on capture ligands synthesis and advised on scientific direction</i>
Funding Support:	

- **Change in the active other support of the PD/PI(s) or senior/key personnel since the last reporting period.**

Nothing to report.

- **Other organization involved as partners**




The electron microscopy facility was used to characterize the morphology of the microneedles platforms by scanning electron microscopy.

- **Organization Name:** NUANCE, Northwestern University
- **Location of Organization:** Evanston, IL
- **Partner's contribution to the project**
  - **Facilities** project staff (Ji Eun Park and Dr. Nihan Yonet-Tanyeri) used the partner's facilities for project activities

## 8. APPENDICES

## Spiers Memorial Lecture

### Surface-enhanced Raman spectroscopy: from single particle/molecule spectroscopy to ångström-scale spatial resolution and femtosecond time resolution

Anne-Isabelle Henry,  Tyler W. Ueltschi,  Michael O. McAnally   
and Richard P. Van Duyne \*

Received 15th August 2017, Accepted 18th August 2017

DOI: 10.1039/c7fd00181a

Four decades on, surface-enhanced Raman spectroscopy (SERS) continues to be a vibrant field of research that is growing (approximately) exponentially in scope and applicability while pushing at the ultimate limits of sensitivity, spatial resolution, and time resolution. This introductory paper discusses some aspects related to all four of the themes for this Faraday Discussion. First, the wavelength-scanned SERS excitation spectroscopy (WS-SERES) of single nanosphere oligomers (*viz.*, dimers, trimers, *etc.*), the distance dependence of SERS, the magnitude of the chemical enhancement mechanism, and the progress toward developing surface-enhanced femtosecond stimulated Raman spectroscopy (SE-FSRS) are discussed. Second, our efforts to develop a continuous, minimally invasive, *in vivo* glucose sensor based on SERS are highlighted. Third, some aspects of our recent work in single molecule SERS and the translation of that effort to ångström-scale spatial resolution in ultrahigh vacuum tip-enhanced Raman spectroscopy (UHV-TERS) and single molecule electrochemistry using electrochemical (EC)-TERS will be presented. Finally, we provide an overview of analytical SERS with our viewpoints on SERS substrates, approaches to address the analyte generality problem (*i.e.* target molecules that do not spontaneously adsorb and/or have Raman cross sections  $<10^{-29}$  cm<sup>2</sup> sr<sup>-1</sup>), SERS for catalysis, and deep UV-SERS.

## 1. Introduction

In the four decades since the publication of the seminal SERS papers and the 11 years since the last Faraday Discussion on SERS,<sup>1</sup> it is useful to reflect on how the field has evolved and matured. Clearly, there has been an enormous outpouring of results, both at the fundamental, basic science level (*e.g.* SMSERS, EC-SERS, TERS, EC-TERS) and at the applied science level (*e.g.* bioassays and diagnostic tools). This is also true in related areas such as localized surface plasmon

Departments of Chemistry, Biomedical Engineering, and Applied Physics, Northwestern University, Evanston, IL 60208-3113, USA. E-mail: vanduyne@northwestern.edu

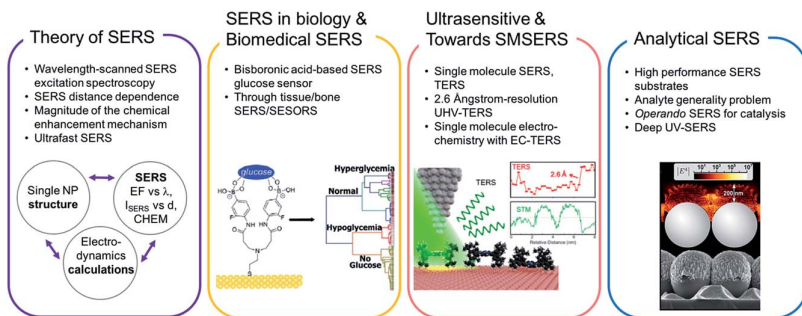


Fig. 1 Overview of significant results and questions in SERS and TERS. Following the four topics of this Faraday Discussion, significant progress and directions in SERS and TERS are presented in these four panels, each illustrated (bottom) by a key concept or result: from left to right, a diagram of the structure–function relationship workflow for single nano-particle SERS; the chemical structure of a bisboronic acid-based glucose sensor for the quantitative detection of glucose levels (reprinted with permission from ref. 48, copyright 2016 American Chemical Society); a schematic representation and data showing the 2.6 Å resolution of TERS for functional surface imaging (reprinted from ref. 55 with permission, copyright 2016 American Chemical Society); the structural characterization by scanning electron microscopy and corresponding electrodynamics calculations for identifying electromagnetic hotspots on SERS Ag metal nanospheres (AgFONs) substrates (reprinted with permission from ref. 71, copyright 2013 American Chemical Society).

resonance (LSPR) biosensing and plasmonics in general. The timeline of discovery and magnitude (presently ~8000 papers per year) of this activity has been carefully reviewed.<sup>2</sup> This introductory lecture discusses some aspects of all four themes of the 2017 Faraday Discussions on SERS. A complete review citing all the contributions from the community is not attempted. Rather, examples from our own work are used to illustrate the main points. Fig. 1 provides a graphical overview of the topics in SERS and TERS that we cover. Examples of the questions that will be addressed include: what nanostructure has the largest enhancement factor (EF)?; what is our current understanding of the magnitude of the chemical (CHEM) mechanism of SERS?; what are the successes and limitations of SERS biosensors?; and what progress has been made in pushing the limits of SERS and TERS with respect to analyte generality, surface generality, spatial resolution, and time resolution?

## 2. Theory of SERS enhancement

The central question of the origin of SERS has been a long-standing discussion in the SERS community, since the early days of SERS in the late 1970s and early 1980s. The two components of the enhancement – electromagnetic and chemical – both contribute; but, are still not as well quantified as one would like. However, significant progress has been made during the past 10 years in characterizing, quantifying, and therefore solidifying our understanding of the mechanisms at play in the enhancements. The following topics have been selected to illustrate some important steps forward in understanding and broadening the theory of SERS enhancement: (1) wavelength-scanned SERS excitation spectroscopy (WS-

SERES); (2) the distance dependence of SERS; (3) the magnitude of the chemical enhancement mechanism; and (4) ultrafast SERS.

## 2.1 WS-SERES of single Au nanosphere oligomers

The question of quantifying the enhancement factor and its relationship to nanoparticle structure and the LSPR spectrum has been addressed in a series of structure–activity relationship studies at the single ‘nanoparticle’ (or, more accurately, the single nanosphere oligomer) level. By taking advantage of the fact that metal nanoparticles strongly scatter light, so that they can be indexed when drop-cast at a relatively low concentration on a TEM grid, it becomes possible to do a spatially correlated LSPR-HRTEM-SERES study. In such studies the LSPR, SERS, and WS-SERES are measured for specific nanosphere oligomers of known structure – shape, size, number of cores and relative geometry in the case of multiple cores – by HRTEM.<sup>3,4</sup>

Spatially correlated LSPR-HRTEM-SERS/SERES studies<sup>5,6</sup> have revealed several important new mechanistic insights about SERS. First, strongly coupled nanoparticles (*i.e.*, 2 or more nanoparticles of the same or different structure containing a “hot spot”) behave in a fundamentally different manner than isolated nanoparticles.<sup>7</sup> Whether in the single wavelength or the wavelength-scanned excitation studies on single nanoparticle oligomers, it was clearly observed that the wavelengths at which the enhancement factor maximum and the LSPR (*i.e.*, extinction maximum) occur do not coincide. In other words, the LSPR scattering maximum could not predict the wavelength at which the maximum average EF occurs. Second, while the LSPR is extremely sensitive to very small structure changes, the SERS EF is more forgiving. Isolated Au nanospheres have maximum average EFs  $< 10^4$ ; but, Au nanosphere oligomers have maximum average EFs of  $1\text{--}4 \times 10^8$  roughly independent of structure (*e.g.* dimers, trimers, tetramers, *etc.*) as long as they provide sub-1 nm crevices in or near the junction site.<sup>5,6</sup>

The practical implications of these studies are significant. First, they demonstrate that using the wavelength of the LSPR maximum to predict the wavelength corresponding to the maximum EF is not correct as it is in the isolated particle case. Second, single nanoparticle oligomer studies unambiguously show how simply changing the excitation wavelength increases the maximum average EF. This means that SERS substrates with strongly coupled nanostructures benefit from excitation wavelengths in the NIR.

## 2.2 The distance dependence of SERS

Gersten and Nitzan<sup>8</sup> developed a model to describe the decay of the SERS intensity as a function of the molecule–metal distance for various plasmonic materials (*e.g.* Ag, Cu, Au) with spheroidal shapes. Experimental efforts followed to measure the SERS distance dependence using various molecular probes and dielectric spacer layers. Using a simplified sphere model and the  $|E|^4$  approximation, the distance dependence can be written as:

$$I = \left(1 + \frac{r}{a}\right)^{-10}$$

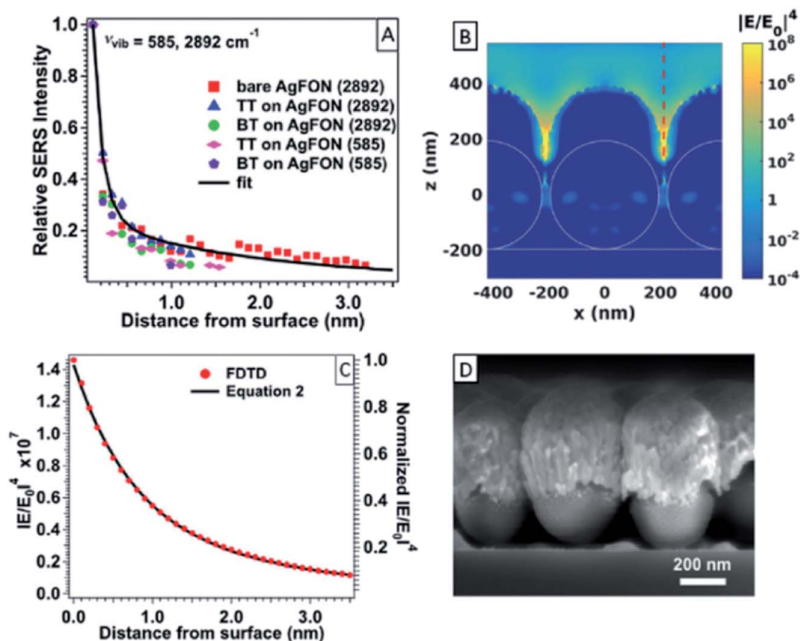
where  $I$  is the SERS intensity,  $a$  is the radius of curvature of the field enhancing nanostructure, and  $r$  is the distance between the adsorbate analyte and center of

the plasmonic sphere. One concludes that the maximum SERS intensity occurs when the adsorbate is in direct contact with the substrate and that the EM enhancement is a long-range effect that typically extends to distances  $\sim 10$  nm away from the metallic surface.<sup>9,10</sup> Kovacs *et al.* investigated the distance dependence of the SERS EF using Langmuir–Blodgett monolayers of arachidic acid on an island film substrate.<sup>10</sup> This study concluded that the lack of direct contact with the tetra-*t*-butyl phthalocyanine probe molecule demonstrates that the long-range distance dependence observed can be attributed to the electromagnetic enhancement. Self-assembled monolayers (SAMs) of thiols have been widely used to probe the distance dependence of SERS. Here the thiol acted either as the spacer layer or as both the spacer layer and probe molecule. SAMs have shown fewer structural defects in the film than Langmuir–Blodgett spacer layers, and thus are viewed as more reliable and reproducible spacer layers.<sup>11–13</sup> Van Duyne introduced the use of atomic layer deposition (ALD) to fabricate ultrathin, conformal dielectric spacers on SERS substrates.<sup>1</sup> In this work, it was concluded that the SERS intensity decreased by a factor of 10 when the probe molecule, pyridine, was spaced 2.8 nm from the AgFON surface.

Recently, the Van Duyne group carried out a high-resolution distance dependence study by using atomically thin ( $\sim 1.3$  Å) layers of  $\text{Al}_2\text{O}_3$  deposited by ALD.<sup>14</sup> In this study, a single Ag film-over-nanospheres (AgFON) substrate was used throughout the course of an ALD alumina deposition, using the methylalumina surface species as the probe molecule. As illustrated in Fig. 2A, we used two different vibrational modes (sym. C–H ( $2892\text{ cm}^{-1}$ ) and sym. Al–CH<sub>3</sub> ( $585\text{ cm}^{-1}$ ) stretches) to monitor the decay of the SERS intensity with respect to the spacer layer thickness. Experimentally, the sharp decrease in SERS intensity as a function of spacer thickness is best fit using a two-term distance expression (see the bottom equation in Fig. 2) with a short-distance and a long-distance dependence. The relative SERS intensity decrease corresponds to a  $\sim 80\%$  loss of signal intensity  $\sim 0.5$  nm away from the surface and 90% loss  $\sim 2$  nm away. In this modified Gersten and Nitzan model,  $a_1$  and  $a_2$  are the short- and long-range radii of curvature features, respectively. The different radii of curvature are associated with the small ( $<1$  nm) and large ( $>10$  nm) nanoparticle structures on the heterogeneous AgFON surface (Fig. 2D). Fig. 2B and C shows the near-field distance dependence of a AgFON calculated using FDTD. The cross-section of the near-field distribution (Fig. 2B) shows, as expected, a maximum value of  $|E/E^0|^4$  in the gap between two nanospheres. In some cases, one can also expect strong localized field hotspots at the top of the AgFON, in between pillars and irregularities. Fig. 2C shows how this local electric field varies when moving away from the metallic surface (red dashed line in panel B). The FDTD calculations clearly show that the field decreases to  $\sim 36\%$  and  $\sim 10\%$  of the initial intensity at distances of  $\sim 1$  and  $\sim 3$  nm from the surface, respectively. A fit of the FDTD data using the two-term Gersten and Nitzan model is in qualitative agreement with the experimental observations in Fig. 2A.

### 2.3 Magnitude of the chemical enhancement mechanism

When the adsorbate is chemically bonded to the surface, the chemical (CHEM) mechanism contributes to the Raman signal enhancement in addition to the electromagnetic mechanism. This enhancement is primarily through charge



$$I_{\text{SERS}} = C_1 \left(1 + \frac{r}{a_1}\right)^{-10} + C_2 \left(1 + \frac{r}{a_2}\right)^{-10}$$

Fig. 2 Distance dependence of SERS. (A) SERS intensity decay of sym. C–H ( $2892\text{ cm}^{-1}$ ) and sym. Al–CH<sub>3</sub> ( $585\text{ cm}^{-1}$ ) stretches as a function of distance with a two-term fit (equation at bottom). (B) Spatial distribution of local electric field enhancement from FDTD calculations of simulated Ag FON surface. (C) Near-field distance dependence profile at gap of simulated Ag FON surface observed at the dashed red line in (B). (D) Side-view SEM micrograph of Ag FON substrate used. Reprinted and adapted with permission from ref. 14, copyright 2016 American Chemical Society.

transfer mechanisms where the excitation wavelength is either resonant or non-resonant with the metal–molecule charge transfer electronic states.<sup>15</sup> Jensen *et al.* calculated theoretical CHEM enhancement factors as high as  $7 \times 10^3$  for *para*- and *meta*-substituted pyridine on a silver cluster. We have investigated both experimentally and theoretically, in collaboration with the Schatz group at Northwestern, the origin and magnitude of the CHEM mechanism by investigating how the total enhancement varies with different substituents on a benzenethiol framework adsorbed on silver and gold.<sup>16</sup> Experimentally, the total enhancement was measured to vary by a factor of 10 as a result of chemical substitution. In unpublished work, we have significantly extended the number of substituted benzenethiol systems to include more electron withdrawing and electron donating substituents. Experimentally, we can now report that the total enhancement varies by a factor of more than  $2 \times 10^2$  over this data set. 4-



Bromobenzenthioi shows the largest enhancement and 4-methylsulfanylbzenzenethioi the lowest.

## 2.4 Ultrafast SERS

In the spirit of pushing the boundaries of what is possible in the domain of SERS, the development of surface-enhanced femtosecond stimulated Raman spectroscopy (SE-FSRS) is an attractive research target. FSRS has been successfully used to monitor the vibrational signature of molecules with both a high temporal resolution (10–100 fs) and high spectral resolution (5–20  $\text{cm}^{-1}$ ).<sup>17,18</sup> However, these experiments necessitate high analyte concentrations and large Raman cross sections. To overcome these challenges, Ploetz *et al.* attempted to combine the high enhancement factors of plasmonic substrates with FSRS using a 1 kHz repetition rate laser system. Unfortunately, they were not able to observe SE-FSRS signals.<sup>19</sup> By using a 100 kHz repetition rate laser system with average powers high enough for signal generation, but low peak powers to avoid substrate damage, SERS was successfully combined with FSRS (Fig. 3A).<sup>20</sup> This proof-of-principle paper presented ground-state SE-FSRS spectra with characteristic Fano-like line-shapes. The authors conservatively estimated time- and ensemble-averaged enhancement factors for SE-FSRS to be  $10^4$  to  $10^6$ ; however, this estimated EF was limited by sample degradation. While the dependence of SE-FSRS gain on Raman pump power was shown to be linear in extremely low power regimes, with increasing power sample degradation resulted in a signal decrease by a factor of 2 on a timescale of 30 minutes (Fig. 3D).

In order to improve the signal to noise ratio (SNR) of SE-FSRS both concentration and pathlength were varied to find the optimal balance between signal generation and probe extinction (*i.e.*, absorption + scattering) (Fig. 3E).<sup>21</sup> To further push the limits of SE-FSRS, a femtosecond stimulated Raman spectrometer was built around a tunable 1 MHz laser system to decrease peak powers while increasing the number of events probed to maximize the SNR (Fig. 3C).<sup>22</sup> The sample damage problem has now been eliminated over the 30 minute data acquisition period required for a three-pulse time-resolved SE-FSRS experiment (Fig. 3D).

In addition to optimizing the SNR of SE-FSRS, significant effort has been put towards uncovering the origin of the observed Fano-like lineshapes arising from these colloidal nanoparticle–molecular systems from both experimental<sup>23,24</sup> and theoretical<sup>25,26</sup> perspectives (Fig. 3B). Experimentally, Frontiera *et al.* used nanosphere oligomer substrates consisting of aggregated 90 or 60 nm Au spheres coated with *trans*-1,2-bis(4-pyridyl)-ethylene (BPE) encapsulated in a silica shell to change the energy of the plasmon resonances of the substrate with respect to the wavelengths of the Raman pump and stimulating probe pulses.<sup>23</sup> They observed that the phases of the dispersive lineshapes change as the plasmon resonance is varied. By fitting to extract the line width and coupling information they observed that the molecule–plasmon coupling has no observable effect on the vibrational coherence lifetime of the molecule. With the use of a tunable 1 MHz system, we have been able to follow up this report with a more in-depth wavelength dependent study. Using the same nanoparticle substrates, Buchanan *et al.* varied the wavelength of the Raman pump pulse and probed both the stimulated Raman gain (SRG) and stimulated Raman loss (SRL) activities (Fig. 3F).<sup>24</sup> This study

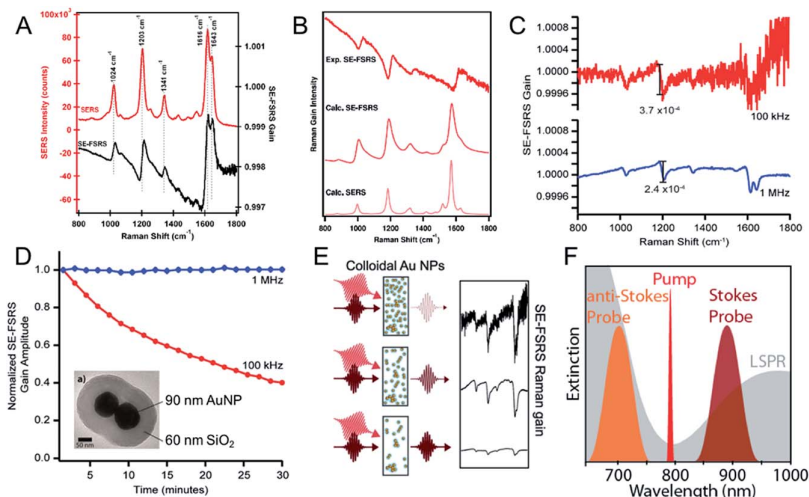


**Fig. 3** Ultrafast SERS. (A) SERS spectrum and SE-FSRS spectrum of *trans*-1,2-bis(4-pyridyl) ethylene (BPE)-functionalized Au nanosphere assemblies (inset in (D)). Both spectra have high S/N. The SE-FSRS spectrum shows dispersive lineshapes due to resonance effects from the plasmon. Image adapted from ref. 20 with permission, copyright 2011 American Chemical Society. (B) Comparison of SE-FSRS experiment and classical coupled wave theory to understand the dispersive lineshapes. Image adapted from ref. 25 with permission, copyright 2017 American Physical Society. (C) SE-FSRS spectra of BPE functionalized Au nanosphere assemblies obtained with 50 pJ per pulse of Raman pump at 100 kHz (red) and 1 MHz (blue). Both repetition rates yield similar SE-FSRS signal strengths; but, the spectra obtained at 100 kHz exhibit noise in the spectral region of 1000–1200 cm<sup>-1</sup> that is 10× greater than that obtained at 1 MHz. (D) Sample damage over 30 min. Data acquisition time has been eliminated at 1 MHz repetition rate. Images (C) and (D) adapted from ref. 22 with permission, copyright 2017 American Chemical Society. (E) To achieve maximum S/N in transmission SE-FSRS experiments requires balancing scattering and enhancement by optimizing nanoparticle concentration and pathlength. Image (E) adapted from ref. 77 with permission, copyright 2016 American Chemical Society. (F) The first multi-wavelength and anti-Stokes SE-FSRS is reported. The SE-FSRS lineshapes vary dramatically as a function of excitation wavelength. Image (F) adapted from ref. 24 with permission, copyright 2017 American Chemical Society.

demonstrated the wide variety of lineshapes attainable in SE-FSRS, as well as lineshape dependence that is not predicted by current SE-FSRS theories.<sup>25,26</sup> This suggests that current theories are incomplete as demonstrated by the incorrectly predicted amounts of dispersive character either near an LSPR<sup>25</sup> or at wavelengths to the red of the LSPR.<sup>26</sup> Thus, further theoretical efforts are needed and should be aided by the collection of additional experimental data over wider ranges of excitation wavelengths. Both theoretical models were applied to single oligomers;<sup>25,26</sup> the presence of dispersive peaks in both sets of calculated SE-FSRS spectra suggests that the complex lineshapes observed experimentally are not simply an artifact of the ensemble measurement. However, to better correlate with theoretical results, experimental studies of individual oligomers should be made in order to remove inherent ensemble averaging. Such measurements would also eliminate any possibility that the broadband probe pulse is being

chirped by propagation through the colloidal sample, potentially creating a phase shift in the stimulating field that could add an additional dispersive element to the measured lineshapes.

As single oligomer-SE-FSRS is experimentally realized, some questions will be answered, but new ones will arise. In particular, there are outstanding questions dealing with the self-heterodyne nature of the SE-FSRS signal that isn't present in similar experiments, such as SE-CARS. Reducing the dimensionality of the experiment by probing individual oligomers will help, but conceptually an understanding of how a self-heterodyned signal field is plasmonically-enhanced is crucial to a deeper knowledge of SE-FSRS. In the same vein, understanding the plasmonic enhancement of a self-heterodyned signal may lead to clues as to why single-oligomer SECARS experiments have not shown dispersive line-shapes<sup>27–29</sup> in comparison to bulk SECARS and solvent experiments.<sup>30,31</sup>

### 3. SERS in biology and biomedical SERS

One of the most successful translations of SERS out of the analytical laboratory lies in its use to probe living systems – from cells to whole bodies – to assist biomedical research from fundamental mechanistic studies up to diagnostics.<sup>32</sup> Owing to the formidable diversity of substrates available (*e.g.*, nanostars, nanospheres with or without magnetic cores, immunoassays, plasmonic paper, plain nanostructured metal films and more), the choice of plasmonic substrate can now be driven by the application itself rather than dictated by technical limitations regarding the incident wavelength or other factors. The substrate can also be adapted to the experiment format: *e.g.*, microfluidic channels,<sup>33</sup> or solution.<sup>34,35</sup>

Probably the most impressive results towards *in vivo*, multiplexed diagnosis come from SERS nanotags that are both sensitive and stable SERS probes with bright, reliable signals in time<sup>36</sup> even through tissue or bone.<sup>37</sup> Typically, SERS nanotags consist of Au or Ag nanospheres on which a Raman reporter molecule is adsorbed, and the whole is coated with a protective silica<sup>38</sup> or polymer<sup>39</sup> shell. These nanotags target pre-determined analytes, *e.g.* biomarkers, through immuno-targeting. Measuring the dye spectrum indirectly proves the presence of the targeted biomarkers, without the need of aggregating metal colloids that inevitably complicate the data analysis. Finally, using different tags with a single measurement – so-called multiplexing – in an imaging detection mode dramatically increases the throughput of one single measurement, making SERS ideal to be used for clinical diagnostics, tumor detection and tumor margin monitoring.<sup>40–43</sup> An additional factor that arises and is quite critical to the translation of Raman and SERS to non-experts and outside the analytical laboratory is the development of miniaturized Raman spectrometers about the size of a smartphone.<sup>44,45</sup>

The work in the Van Duyn lab to develop an *in vivo* glucose sensor based on SERS is a good example of an important biosensing problem that requires chemical modification of the surface to effect glucose binding or close approach. While glucose is an important analyte, the Raman cross-section was only recently published by the Van Duyn group,<sup>46</sup> who demonstrated the difficulties in glucose Raman scattering – necessitating the use of SERS. The first-generation sensor was based on mixed self-assembled monolayers that acted as partition layers for close glucose approach, but had no selectivity for glucose *vs.* fructose.<sup>47</sup> The second

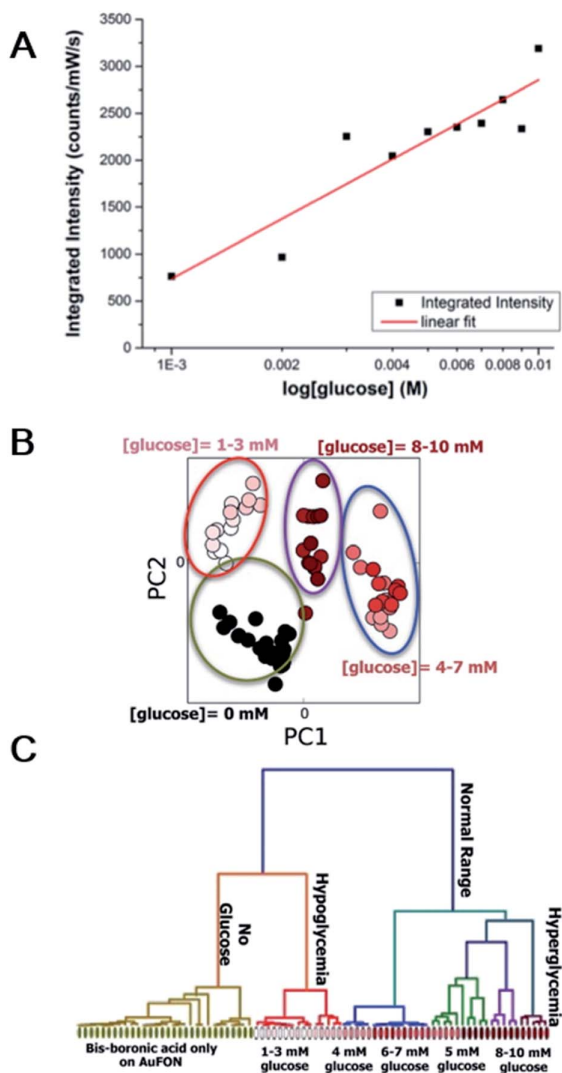


Fig. 4 Quantitative detection of glucose by SERS. (A) Quantitative relationship between SERS signal and glucose concentration as shown by the linear log scale glucose concentration (1–10 mM) as a function of integrated SERS intensity (1070  $\text{cm}^{-1}$  peak, SERS difference spectra). (B) Principal Component Analysis (PCA) comparison of PC1 vs. PC2 for varying concentrations of glucose (1–10 mM). (C) Greater distinction between spectra is found when coupling Hierarchical Cluster Analysis (HCA) with PCA. HCA enables distinguishing between hypoglycemia (1–3 mM), normal glucose range (4–8 mM), and hyperglycemia (>8 mM). Reproduced with permission from ref. 48, copyright American Chemical Society 2016.

generation SERS glucose sensor improves the selectivity towards glucose.<sup>48</sup> A novel bisboronic acid ligand with a tunable scaffold incorporating two mono-fluoro boronic acid motifs, known to bind saccharides<sup>49</sup> and a thiol moiety

enabling binding to metal surfaces has now been developed.<sup>48</sup> By varying the distance between the amine and each boronic acid moiety, the binding constant for glucose can be tuned from 29 up to 167 M<sup>-1</sup>. In addition, the ratio of the binding constants for glucose to fructose can be tuned, resulting in more favorable selectivity of glucose with respect to fructose. Spectroscopically, glucose is qualitatively and quantitatively detected *via* SERS difference spectroscopy, *i.e.* the subtraction of the 'BBA only' from the 'BBA with glucose' spectrum. The unique glucose vibrations (840 cm<sup>-1</sup>, 1095 cm<sup>-1</sup>, 1342 cm<sup>-1</sup>) and the distinctive derivative lineshape (~1620 cm<sup>-1</sup>) that are observed attest to the effective binding of glucose to the immobilized ligands. Fig. 4A displays the quantitative relationship between the SERS signal and glucose concentration. Principal component analysis (PCA) shows that the concentration response of the sensor is clustered in distinct groups (Fig. 4B). Further, Fig. 4C shows that even greater distinction between spectra is found when Hierarchical Cluster Analysis (HCA) is coupled with PCA. HCA enables the classification of the sensor response as indicative of hypoglycemia (1–3 mM), the normal glucose range (4–8 mM), and hyperglycemia (>8 mM).

## 4. Ultrasensitive and towards single molecule SERS

### 4.1 Single molecule SERS and TERS

SERS has the capability of detecting and identifying single molecules that are resonance Raman active. The strongest evidence to date for single molecule SERS (SMSERS) is the isotopologue proof (Fig. 5A–D).<sup>50</sup> Silver nanoparticles are dosed with a 50 : 50 mixture of the two R6G isotopologues at a total concentration of 10<sup>-9</sup> M (Fig. 5B). Very high SNR single molecule SERS spectra are obtained on each nanoparticle that show isotopically sensitive vibrational modes at 601 cm<sup>-1</sup> and 611 cm<sup>-1</sup> (Fig. 5C). A histogram ( $N = 50$ ) of such single molecule events is shown in Fig. 5D. The structures of the silver nanoparticles (Fig. 5E) that yielded single molecule SERS was obtained by the correlated LSPR-HRTEM-SMSERS method.<sup>51</sup> These results show that only nanoparticle assemblies yield SMSER spectra confirming the hypothesis and early results<sup>52,53</sup> on the need for 'hot spots' in or near nanoparticles' junction(s). Further, it is demonstrated that fused nanoparticles of any shape yield high quality SMSERS and nanoparticle assemblies that have nanogaps are not required to observe SMSERS.

Likewise, the isotopologue proof has been used to establish the existence of single molecule tip-enhanced Raman spectroscopy (SMTERS).<sup>54</sup> A combination of experimental and theoretical studies provides a detailed view of the isotopic response of R6G-*d*<sub>0</sub> and R6G-*d*<sub>4</sub> in the 600–800 cm<sup>-1</sup> region. The single-molecule nature of the TERS experiment is confirmed through two lines of evidence. First, the vibrational signature of only one isotopologue at a time was observed from multiple TERS spectra. Second, the spectral wandering of the 610 cm<sup>-1</sup> mode of R6G-*d*<sub>0</sub> was less than 4 cm<sup>-1</sup>, which in turn is less than the 10 cm<sup>-1</sup> isotopic shift so that no confusion in assignment resulted. Consequently, the total TERS enhancement factor can now be accurately established as  $EF_{\text{TERS}} = 1.0 \times 10^{13}$  because only one molecule at a time is measured. Furthermore,  $EF_{\text{TERS}}$  can be

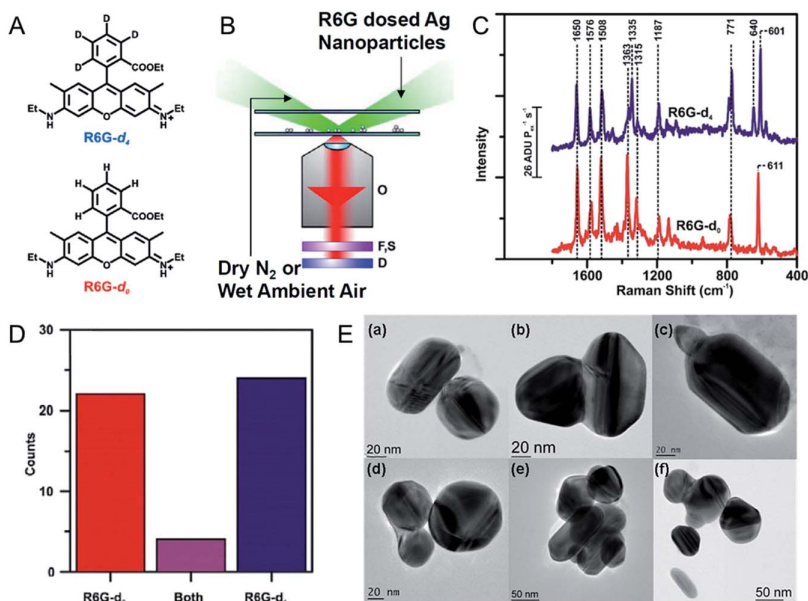
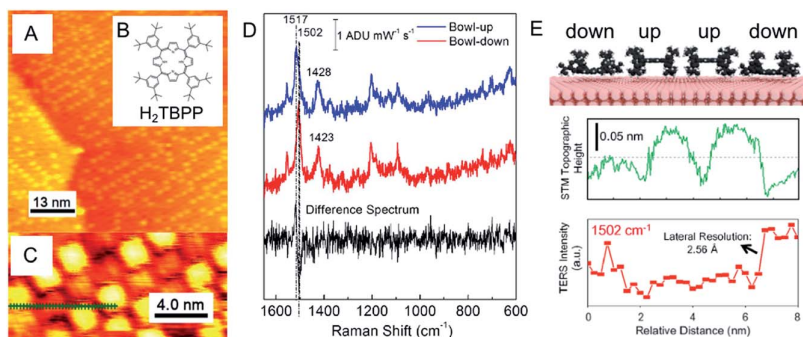


Fig. 5 Isotopologue proof of single molecule SERS. (A) Chemical structure of the isotopologues: R6G-*d*<sub>4</sub> and R6G-*d*<sub>0</sub>. (B) Ag nanoparticles dosed with a 50 : 50 mixture of R6G isotopologues at a total concentration of  $10^{-9}$  M. (C) SMSERS of R6G-*d*<sub>0</sub> (red line) and R6G-*d*<sub>4</sub> (blue line) ( $\lambda_{\text{ex}} = 532$  nm,  $t_{\text{aq}} = 10$  s,  $P_{\text{ex}} = 2.4$  W cm<sup>-2</sup>, grazing incidence). (D) Histogram of SMSERS events where only R6G-*d*<sub>0</sub>, only R6G-*d*<sub>4</sub> and both R6G-*d*<sub>0</sub> and R6G-*d*<sub>4</sub> vibrational modes were observed. (A–D) Reprinted with permission from ref. 50, copyright 2007 American Chemical Society. (E) TEM images of SMSERS active nanostructures. Reprinted with permission from ref. 51, copyright 2008 American Chemical Society.

partitioned into an electromagnetic contribution of  $10^6$  and a molecule-localized resonance Raman contribution of  $10^7$ .

#### 4.2 2.6 Å resolution UHV-TERS

UHV-TERS combines the ability of scanning probe microscopy (SPM) to resolve atomic-scale surface features with the single molecule chemical sensitivity of surface-enhanced Raman spectroscopy (SERS). The conformational dynamics of a free-base porphyrin, *meso*-tetrakis(3,5-ditertiarybutylphenyl)-porphyrin (H<sub>2</sub>TBPP, Fig. 6B), adsorbed on a Cu(111) surface at room temperature are interrogated with UHV-TERS (Fig. 6A–E).<sup>55</sup> The H<sub>2</sub>TBPP/Cu(111) system has two metastable surface-mediated isomers (Fig. 6A). At room temperature, the barrier between the porphyrin ring buckled up and buckled down conformations is easily overcome and the two conformers randomly switch between these two states (Fig. 6C). Simultaneous measurement of STM (Fig. 6E middle) and TERS line scans (Fig. 6E bottom) across four H<sub>2</sub>TBPP molecules (Fig. 6C) demonstrates that TERS has 2.6 Å lateral resolution under ultrahigh vacuum (UHV) conditions. This work presents the first UHV-TERS on Cu(111) and unambiguously demonstrates



**Fig. 6** High resolution UHV-TERS. (A) Large-scale STM topographic image of a sub-monolayer coverage of  $\text{H}_2\text{TBPP}$  on  $\text{Cu}(111)$  as probed by a Ag tip (imaging conditions: 1.0 V, 100 pA, 60 nm  $\times$  60 nm). (B) Molecular structure of  $\text{H}_2\text{TBPP}$ . (C) High-resolution STM topographic image probed by a Ag tip (imaging conditions: 0.75 V, 550 pA, 16 nm  $\times$  8 nm) before the TERS imaging experiment. The dotted green line indicates the points where TERS spectra were obtained. (D) TERS spectrum of the bowl-up and bowl-down conformations of  $\text{H}_2\text{TBPP}$  reconstructed from the line scan. The difference spectrum shows a  $\sim 15 \text{ cm}^{-1}$  shift in the  $1502 \text{ cm}^{-1}$  mode for the down geometry. TERS spectra were acquired with 1.00 mW 561 nm excitation for 30 s. (E) Top: Schematic of  $\text{H}_2\text{TBPP}$  porphyrin rings on  $\text{Cu}(111)$  buckled up/down, middle: simultaneously acquired STM line scan, bottom: TERS line scan of the integrated  $1502 \text{ cm}^{-1}$  mode. Reprinted with permission from ref. 55, copyright 2016 American Chemical Society.

that TERS can distinguish the conformational differences between neighboring molecules with ångström-scale spatial resolution.

### 4.3 Single molecule electrochemistry with EC-AFM-TERS

A nanoscale understanding of electrochemical processes, including heterogeneities in electrochemical behavior across an electrode surface, is critical to understanding electrocatalysis, biological electron transfer, energy production, and energy storage. TERS is an ideal tool for elucidating structure–activity relationships in electrochemical systems at the nanoscale. Electrochemical atomic force microscopy tip-enhanced Raman spectroscopy (EC-AFM-TERS) was first demonstrated by Kuroski *et al.*<sup>56</sup> and electrochemical scanning tunneling microscopy tip-enhanced Raman spectroscopy (EC-STM-TERS) by Zeng *et al.*<sup>57</sup> Kuroski *et al.* published the first TERS study of a redox reaction.<sup>56</sup> Using an electrochemical AFM (EC-AFM) platform (Fig. 7A) the authors investigated the redox behavior of Nile Blue (NB) spontaneously adsorbed onto an indium-tin oxide (ITO) surface. TERS spectra were acquired with a Au tip (70 nm Au on Si) using 632.8 nm excitation. The spectrum of NB was monitored during cyclic voltammetry in Tris buffer (50 mM Tris + 50 mM NaCl at pH 7), scanning from 0 to  $-0.6 \text{ V}$  versus Ag/AgCl and back with a scan rate of  $10 \text{ mV s}^{-1}$  (Fig. 7B). As the potential was swept from 0 to  $-0.6 \text{ V}$ , the resonant oxidized form ( $\text{NB}_{\text{OX}}$ ) was converted to the nonresonant reduced form ( $\text{NB}_{\text{RED}}$ ) and the intensity of the  $591 \text{ cm}^{-1}$  mode decreased (Fig. 7C). Upon scanning the potential back to 0 V versus Ag/AgCl,  $\text{NB}_{\text{RED}}$  was oxidized back to  $\text{NB}_{\text{OX}}$  and the signal increased back to its original intensity (Fig. 7C). TERS voltammograms were constructed by



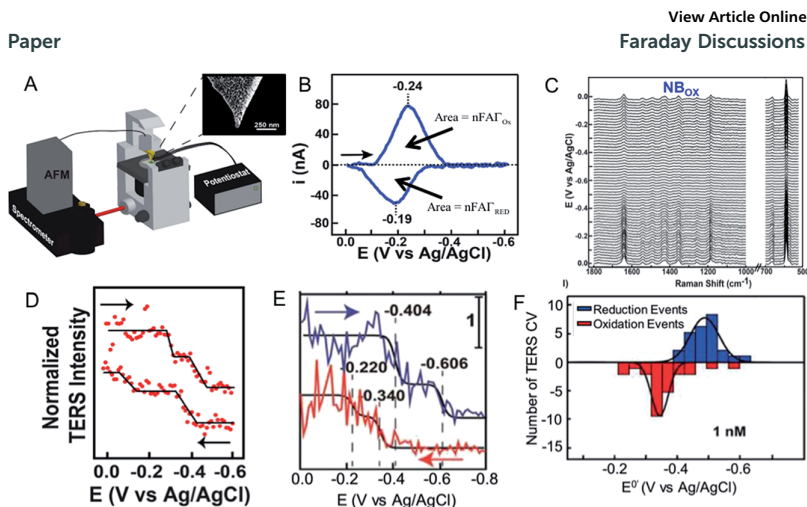


Fig. 7 Single-molecule EC-AFM-TERS. (A) EC-AFM-TERS apparatus with Au-coated (70 nm) tip, as observed by scanning electron microscopy in inset. (B) Background subtracted CV of NB on ITO. (C) Potential dependence of the integrated TERS intensity of the 591  $\text{cm}^{-1}$  band of oxidized Nile Blue ( $\text{NB}_{\text{ox}}$ ). (D) Potential dependence of the integrated TERS intensity shows step-like behavior indicative of single- or few-molecule electrochemistry at coverage = 0.02 ML. (A–D) Reprinted with permission from ref. 56, copyright 2015 American Chemical Society. (E) Potential dependence of the integrated TERS intensity and fitting to the Laviron model at coverage < 0.0001 ML. (F) Histograms of single molecule formal potentials extracted from fitting TERS CVs. (E) and (F) Reprinted with permission from ref. 58, copyright 2017 American Chemical Society.

integrating the intensity of the 591  $\text{cm}^{-1}$  mode. Remarkably, some TERS voltammograms, such as the one shown in Fig. 7D, exhibit steplike features indicative of few- or single-molecule behavior. That we are working in the few- or single-molecule regime is further corroborated by calculating the average number of molecules under the tip. For a tip radius of 20 nm and an average surface number density of  $2 \times 10^{12}$  molecules per  $\text{cm}^2$ , the average number of molecules under the tip is  $\sim 6$ . In other locations on the sample, the TERS voltammogram did not contain steps, demonstrating a nonuniform surface coverage of NB across the ITO surface. This work demonstrated the potential of TERS for studying redox reactions at the nanoscale, probing few- or single-molecule behavior across a nonuniform surface coverage inaccessible by SERS.

EC-AFM-TERS was employed for the first time to observe nanoscale spatial variations in the formal potential,  $E^0$ , of a surface-bound redox couple.<sup>58</sup> TERS cyclic voltammograms (TERS CVs) of single Nile Blue (NB) molecules were acquired at different locations spaced 5–10 nm apart on an indium tin oxide (ITO) electrode (Fig. 7E). Analysis of TERS CVs at different coverages was used to verify the observation of single-molecule electrochemistry. The resulting TERS CVs were fit to the Laviron model for surface-bound electroactive species to quantitatively extract the formal potential  $E^0$  at each spatial location. Histograms of the single-molecule  $E^0$  at each coverage indicate that the electrochemical behavior of the cationic oxidized species is less sensitive to the local environment than the neutral reduced species (Fig. 7F). This information is not accessible using purely electrochemical methods or ensemble spectroelectrochemical measurements. We anticipate that the



quantitative modeling and measurement of site-specific electrochemistry with EC-AFM-TERS will have a profound impact on our understanding of the role of nanoscale electrode heterogeneity in applications such as electrocatalysis.

The most recent EC-STM-TERS study examined adsorption geometry and chemical reactivity as a function of applied potential.<sup>59</sup> Combined experimental and simulation data for the case of adenine/Au(111) demonstrated that protonated physisorbed adenine adopts a tilted orientation at low potentials while it is vertically adsorbed near the potential of zero charge. Further potential increase induces adenine deprotonation and reorientation to a planar configuration.

#### 4.4 Summary comments on ultrasensitive and single molecule SERS/TERS

Enormous progress has been made in the last 10 years in the area of ultrasensitive and single molecule SERS/TERS. SMSERS has been convincingly demonstrated by the isotopologue method; it requires “hot spots” but not necessarily nanogaps in nanoparticle assemblies, and the excitation of a molecular electronic resonance. SMSERS is beginning to move from proof-of-concept experiments to fundamental studies of molecular motion on nanoparticle surfaces using super-resolution microscopy approaches,<sup>60</sup> monitoring catalytic processes,<sup>61</sup> and studying chemical reactivity through single-site, single-molecule electrochemistry.<sup>62–64</sup>

Likewise, SMTERS has been established by the isotopologue method and the tip or tip-sample junction is a scanning “hot spot” with extraordinary spatial resolution down to the few Ångström level. TERS of adsorbed molecules that do not possess an electronic resonance at the laser excitation wavelength shows an electromagnetic enhancement of only 4–6 orders of magnitude. This is sufficient to observe a few hundred molecules under the tip at packing densities near full monolayer coverage; but, to achieve single molecule sensitivity, an additional resonance enhancement of 4–7 orders of magnitude is required.

Over the last decade, TERS and UHV-TERS in particular have been established as important techniques for the high-resolution functional imaging of surfaces. A notable example is the demonstration of the nanoscale chemical imaging of a dynamic molecular phase boundary.<sup>65</sup> Other noteworthy outcomes include low-temperature (19 K) UHV-TERS,<sup>66</sup> minimized tip and molecular degradation,<sup>67</sup> and improved stability in the presence of ultrafast irradiation.<sup>68</sup> Moving forward, TERS needs to demonstrate its generality with respect to substrates and adsorbates. While it is being used very successfully on Au, Ag, and Cu through the hybridization between the plasmon resonances of the tip and sample (gap-mode plasmons), the high resolution mapping of 1 nm or less has yet to be demonstrated on non-plasmonic substrates. However, one can point to the successful use of the ITO surface as the working electrode in the single molecule EC-AFM-TERS studies cited above. If current trends continue and TERS can be demonstrated under a wider range of experimental conditions, including ever more realistic *in situ* studies, it is destined to become a major analytical technique for surface science.

## 5. Analytical SERS

The analytical application of SERS is a broad and rapidly developing sub-field. No attempt is made here to present a comprehensive review, rather the following

topics are presented to illustrate some key points relevant to: (1) SERS substrates; (2) the analyte generality problem; (3) *operando* SERS for catalysis; and (4) deep UV-SERS.

### 5.1 SERS substrates

Without delving into the broad topic of SERS substrates, recently reviewed elsewhere,<sup>69</sup> a few comments are, nevertheless, in order. Many papers continue to be published on SERS substrates.<sup>70</sup> A possible explanation for this circumstance is that SERS continues to be a favourite 'application' reported for virtually any plasmonic substrate, therefore not adding much more than noise to the SERS literature. The Van Duyne lab views the SERS substrate problem as one that is largely solved. The key rules for the rational design of SERS substrates have been established.<sup>5,6,45,69</sup> We argue that new SERS substrates should not be designed based on solely the novelty of a nanoparticle shape or size, but driven more by experimental constraints or applications.

Taking the three high performance substrates (FONs, NSL nanotriangles, and nanosphere oligomers) used in the Van Duyne lab (Fig. 8A–C) as examples, all possess a minimum average EF  $\sim 10^8$  at an excitation wavelength of 785 nm, have tuneable LSPR responses to achieve a maximum average EF at excitation wavelengths ranging from UV–NIR, are reproducible, and are uniform ( $<10\%$  intensity

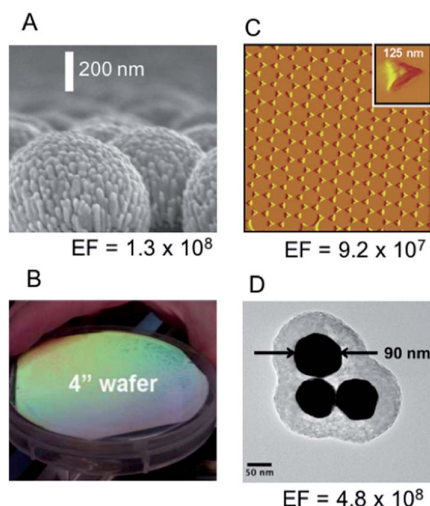


**Fig. 8** High-performance SERS substrates showing strong enhancement factors (EFs). (A) Silver film-over-nanospheres (AgFONs) exhibiting an immobilized nanopillar array (AgINRA) as seen by high-resolution SEM. (B) AgFON substrates with AgINRA features are reproducible on the macroscopic scale with near uniform EFs. Reprinted with permission from ref. 71, copyright 2013 American Chemical Society. (C) An extension of the AgFON–AgINRA substrates, periodic particle arrays (PPAs) designed by nanosphere lithography (NSL) techniques and mask-stripping. Reprinted with permission from ref. 78, copyright 2007 American Chemical Society. (D) To fully understand the surface-enhancement process from plasmonic substrates, fully correlated studies are performed on silica-encased colloidal SERS substrates. Reprinted with permission from ref. 5, copyright 2010 American Chemical Society.

variation across the surface). All can be fabricated at wafer scale given enough effort (Fig. 8D).<sup>71</sup> To be sure, fabrication and information transfer challenges remain in order to achieve these metrics. That said, a reliable commercial source of SERS substrates with optimum metrics would be of significant benefit to the SERS field.

## 5.2 The analyte generality problem

When target analytes have high affinities for bare plasmonic surfaces, there is no problem getting high quality SERS data. However, many important target analytes do not bind to bare plasmonic surfaces. The glucose sensing problem, briefly described above, is a case in point. In such cases, it becomes evident that engineering plasmonic surfaces for all types of analytes is required to enable SERS to be a truly general analytical method. Further, all such surface engineering approaches must also satisfy the constraints imposed by the SERS distance dependence.

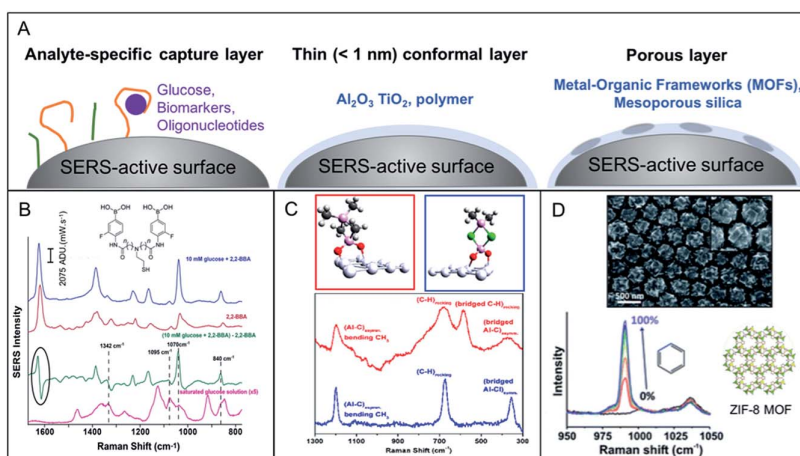


**Fig. 9** Strategies for substrate generality. (A) From left to right, schematic drawings illustrating: the adsorption of analyte-specific adsorbate layers aiming to capture small biological molecules (e.g., glucose), biomarkers, and oligonucleotides; thin (less than 1 nm thick) conformal layers made of alumina or titania deposited by atomic layer deposition (ALD), or thin polymer layers, enabling non-binding analytes to still lay within the sensing volume of the SERS substrate; porous layers such as metal–organic frameworks and mesoporous silica that can trap small non-binding molecules and thus give physical access to the SERS substrate. (B) Illustration of an analyte-specific capture layer for glucose, consisting of a fluorinated bisboronic acid analogue, whose perturbation of the  $\sim 1620\text{ cm}^{-1}$  band informs the presence of glucose both qualitatively and quantitatively (direct correlation between glucose concentration and integrated intensity). Reprinted with permission from ref. 48, copyright 2016 American Chemical Society. (C) *In operando* SERS spectra and corresponding molecular structures of methylalumina ALD species. Reprinted with permission from ref. 75, copyright 2017 American Chemical Society. (D) Scanning electron microscopy image of a MOF (ZIF-8)-protected AgFON substrate and corresponding SER spectra displaying growth of captured species. Reprinted with permission from ref. 73, copyright 2014 American Chemical Society.

Fig. 9A schematically illustrates three surface engineering strategies that have been demonstrated to deal with target analytes that do not directly bind to plasmonic surfaces. All three are layered structures that: (1) specifically capture the target analytes; (2) are ultrathin (<1 nm) and conformal; and (3) have a tuneable pore size. An example of the short capture ligand strategy is the bisboronic acid SERS glucose sensor, further illustrated in Fig. 9B.<sup>48</sup> ALD was used to implement the ultrathin conformal layer strategy to detect an anthrax biomarker (Fig. 9C).<sup>72</sup> Kreno *et al.* (Fig. 9D) demonstrated the porous layer approach by trapping weakly binding analytes (volatile aromatic molecules: benzene and toluene) within metal–organic frameworks grafted on AgFON surfaces.<sup>73</sup> Concentration dependence and time resolved measurements provided evidence for the hypothesis that these vapors were reversibly adsorbed on the surfaces of MOF nanocrystals exposed at grain boundaries. This work represents an interesting but nascent avenue that needs to be generalized.

### 5.3 Operando SERS for catalysis

*Operando* spectroscopy simultaneously studies the fundamental spectroscopic characterization of surface phenomena and catalytic performance.<sup>74</sup> *Operando* measurements differ from *in situ* measurements by being performed under “true catalytic” conditions, where catalytic activity/selectivity measurements can be

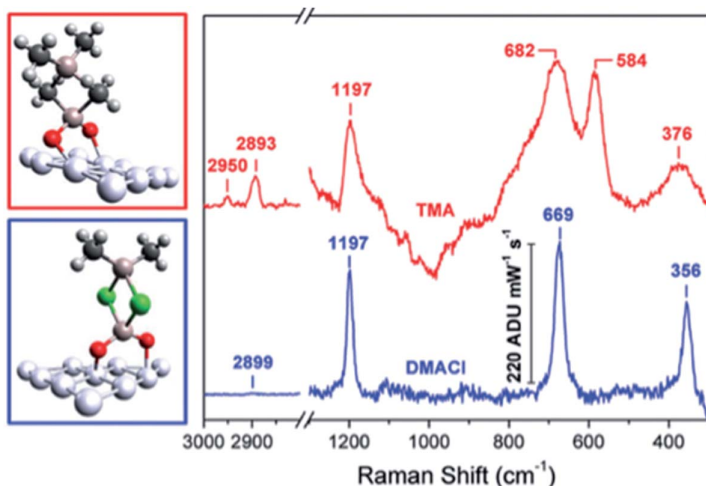


Fig. 10 Structural determination of surface species by integrating atomic layer deposition (ALD) with SERS. Left: Molecular structures of transient dimeric surface species. Right: SERS difference spectra of a AgFON exposed to 60 s of trimethylaluminum (TMA) (1st cycle) (red) and 60 s of dimethylaluminum chloride (DMACl) (1st cycle) (blue) in the low wavenumber (1300–300  $\text{cm}^{-1}$ ) and C–H (3000–2800  $\text{cm}^{-1}$ ) stretching regions. Two of the three peaks observed with both precursors – at 1197 and 682/669  $\text{cm}^{-1}$  – are attributed to alumina surface species with a coordinated methyl group. The peak seen only in the TMA spectrum at 584  $\text{cm}^{-1}$  ( $\nu$ (bridged C–H rocking)) is assigned to the bridged methyl rocking in the parallel and perpendicular dimer models based on comparison to simulations. Reprinted with permission from ref. 75. Copyright 2017 American Chemical Society.

made alongside structural measurements.<sup>74</sup> *In situ* SERS typically falls short of providing insight into the catalytic system of interest due to either the cell or the substrate being incapable of withstanding the high pressures and temperatures necessary for measuring the relevant kinetic information. Issues such as heat and mass transfer gradients can also arise from cell design and can complicate kinetics measurements. Over other techniques, *operando* SERS has the advantage of being able to probe the lower wavenumber region during reaction-specific conditions as a means of acquiring structurally relevant information about the analyte species. By probing the low wavenumber region, where pertinent metal-carbon and metal-oxygen vibrations are located, one can determine the structures of transient species present during the reaction. This type of study was recently performed on the alumina ALD process to show previously unestablished transient dimeric surface species.<sup>75</sup> Illustrated in Fig. 10 are the low wavenumber vibrational modes that were used to make structural determinations about the dimeric methylalumina species.

#### 5.4 Deep UV SERS

Aluminum film over nanosphere (ALFON) substrates have been fabricated for UV-SERS at the deepest UV wavelength reported to date ( $\lambda_{\text{ex}} = 229$  nm). The ALFONs were fabricated with two different support nanosphere sizes using localized surface plasmon resonance spectroscopy, electron microscopy, the SERS of adenine, tris-(2,2'-bipyridine)ruthenium(II) and *trans*-1,2-bis(4-pyridyl)-ethylene, the SERS of 6-mercapto-1-hexanol (as a nonresonant molecule), and dielectric function analysis. Overall, we found that ALFONs with a native  $\text{Al}_2\text{O}_3$  oxide layer have plasmonic properties for deep UV-SERS that in combination with the resonance enhancement of the adsorbates can give average enhancement factors of the order of  $10^6$ . These experimental results are supported by theoretical analysis of the dielectric function.<sup>76</sup>

## Acknowledgements

We gratefully acknowledge the following sources of support for this research: the National Science Foundation through the Center for Chemical Innovation dedicated to Chemistry at the Space-Time Limit (CaSTL) Grant CHE-1414466; the Northwestern University Materials Research Science and Engineering Center Grant DMR-1121262; Grant CHE-1506683, and the Graduate Research Fellowship Grant DGE-0824162; the Department of Energy Office of Basic Energy Sciences SISGR Grant DE-FG02-09ER16109 and the Northwestern University Institute for Catalysis in Energy Processes (ICEP) Grant DE-FG02-03ER15457; the Air Force Office of Scientific Research MURI Grant FA9550-14-1-0003; the Air Force Research Laboratory under Agreement FA8650-15-2-5518; and the Assistant Secretary of Defense for Health Affairs, through the Peer Reviewed Medical Research Program under Award No. W81XWH-16-1-0375. The views and conclusions contained herein are those of the authors and should not be interpreted as necessarily representing the official policies or endorsements, either expressed or implied, of the Air Force Research Laboratory or the U.S. Government. The opinions, interpretations, conclusions, and recommendations are those of the authors and are not necessarily endorsed by the Department of Defense.

## References

- 1 J. A. Dieringer, A. D. McFarland, N. C. Shah, D. A. Stuart, A. V. Whitney, C. R. Yonzon, M. A. Young, X. Zhang and R. P. Van Duyne, *Faraday Discuss.*, 2006, **132**, 9–26.
- 2 D. Graham, M. Moskovits and Z.-Q. Tian, *Chem. Soc. Rev.*, 2017, **46**, 3864–3865.
- 3 Y. Wang, S. K. Eswaramoorthy, L. J. Sherry, J. A. Dieringer, J. P. Camden, G. C. Schatz, R. P. Van Duyne and L. D. Marks, *Ultramicroscopy*, 2009, **109**, 1110–1113.
- 4 A.-I. Henry, J. M. Bingham, E. Ringe, L. D. Marks, G. C. Schatz and R. P. Van Duyne, *J. Phys. Chem. C*, 2011, **115**, 9291–9305.
- 5 K. L. Wustholz, A.-I. Henry, J. M. McMahon, R. G. Freeman, N. Valley, M. E. Piotti, M. J. Natan, G. C. Schatz and R. P. V. Duyne, *J. Am. Chem. Soc.*, 2010, **132**, 10903–10910.
- 6 S. L. Kleinman, B. Sharma, M. G. Blaber, A.-I. Henry, N. Valley, R. G. Freeman, M. J. Natan, G. C. Schatz and R. P. Van Duyne, *J. Am. Chem. Soc.*, 2013, **135**, 301–308.
- 7 A. D. McFarland, M. A. Young, J. A. Dieringer and R. P. Van Duyne, *J. Phys. Chem. B*, 2005, **109**, 11279–11285.
- 8 J. Gersten and A. Nitzan, *J. Chem. Phys.*, 1980, **73**, 3023–3037.
- 9 E. C. Le Ru and P. G. Etchegoin, *Principles of Surface-Enhanced Raman Spectroscopy*, Elsevier, Amsterdam, 2009.
- 10 G. J. Kovacs, R. O. Loutfy, P. S. Vincett, C. Jennings and R. Aroca, *Langmuir*, 1986, **2**, 689–694.
- 11 Q. Ye, J. Fang and L. Sun, *J. Phys. Chem. B*, 1997, **101**, 8221–8224.
- 12 G. Compagnini, C. Galati and S. Pignataro, *Phys. Chem. Chem. Phys.*, 1999, **1**, 2351–2353.
- 13 B. J. Kennedy, S. Spaeth, M. Dickey and K. T. Carron, *J. Phys. Chem. B*, 1999, **103**, 3640–3646.
- 14 S. S. Masango, R. A. Hackler, N. Large, A.-I. Henry, M. O. McAnally, G. C. Schatz, P. C. Stair and R. P. Van Duyne, *Nano Lett.*, 2016, **16**, 4251–4259.
- 15 L. Jensen, C. M. Aikens and G. C. Schatz, *Chem. Soc. Rev.*, 2008, **37**, 1061–1073.
- 16 N. Valley, N. Greeneltch, R. P. Van Duyne and G. C. Schatz, *J. Phys. Chem. Lett.*, 2013, **4**, 2599–2604.
- 17 R. R. Frontiera and R. A. Mathies, *Laser Photonics Rev.*, 2011, **5**, 102–113.
- 18 P. Kukura, D. W. McCamant and R. A. Mathies, *Annu. Rev. Phys. Chem.*, 2007, **58**, 461–488.
- 19 E. Ploetz, M. Gellner, M. Schütz, B. Marx, S. Schlücker and P. Gilch, *AIP Conf. Proc.*, 2010, **1267**, 88–89.
- 20 R. R. Frontiera, A.-I. Henry, N. L. Gruenke and R. P. Van Duyne, *J. Phys. Chem. Lett.*, 2011, **2**, 1199–1203.
- 21 N. L. Gruenke, M. O. McAnally, G. C. Schatz and R. P. Van Duyne, *J. Phys. Chem. C*, 2016, **120**, 29449–29454.
- 22 L. E. Buchanan, N. L. Gruenke, M. O. McAnally, B. Negru, H. E. Mayhew, V. A. Apkarian, G. C. Schatz and R. P. Van Duyne, *J. Phys. Chem. Lett.*, 2016, **7**, 4629–4634.
- 23 R. R. Frontiera, N. L. Gruenke and R. P. Van Duyne, *Nano Lett.*, 2012, **12**, 5989–5994.

- 24 L. E. Buchanan, M. O. McAnally, N. L. Gruenke, G. C. Schatz and R. P. Van Duyne, *J. Phys. Chem. Lett.*, 2017, **8**, 3328–3333.
- 25 M. O. McAnally, J. M. McMahon, R. P. Van Duyne and G. C. Schatz, *J. Chem. Phys.*, 2016, **145**, 094106.
- 26 A. Mandal, S. Erramilli and L. Ziegler, *J. Phys. Chem. C*, 2016, **120**, 20998–21006.
- 27 S. Yampolsky, D. A. Fishman, S. Dey, E. Hulkko, M. Banik, E. O. Potma and V. A. Apkarian, *Nat. Photonics*, 2014, **8**, 650–656.
- 28 Y. Zhang, Y.-R. Zhen, O. Neumann, J. K. Day, P. Nordlander and N. J. Halas, *Nat. Commun.*, 2014, **5**, 4424.
- 29 K. T. Crampton, A. Zeytunyan, A. S. Fast, F. T. Ladani, A. Alfonso-Garcia, M. Banik, S. Yampolsky, D. A. Fishman, E. O. Potma and V. A. Apkarian, *J. Phys. Chem. C*, 2016, **120**, 20943–20953.
- 30 X. Hua, D. V. Voronine, C. W. Ballmann, A. M. Sinyukov, A. V. Sokolov and M. O. Scully, *Phys. Rev. A*, 2014, **89**, 043841.
- 31 D. V. Voronine, A. M. Sinyukov, X. Hua, K. Wang, P. K. Jha, E. Munusamy, S. E. Wheeler, G. Welch, A. V. Sokolov and M. O. Scully, *Sci. Rep.*, 2012, **2**, 891.
- 32 A.-I. Henry, B. Sharma, M. F. Cardinal, D. Kurouski and R. P. Van Duyne, *Anal. Chem.*, 2016, **88**, 6638–6647.
- 33 D. Kim, A. R. Campos, A. Datt, Z. Gao, M. Rycenga, N. D. Burrows, N. G. Greeneltch, C. A. Mirkin, C. J. Murphy, R. P. Van Duyne and C. L. Haynes, *Analyst*, 2014, **139**, 3227–3234.
- 34 D. Graham, D. G. Thompson, W. E. Smith and K. Faulds, *Nat. Nanotechnol.*, 2008, **3**, 548–551.
- 35 T. Donnelly, W. E. Smith, K. Faulds and D. Graham, *Chem. Commun.*, 2014, **50**, 12907–12910.
- 36 A. Pallaoro, G. B. Braun and M. Moskovits, *Nano Lett.*, 2015, **15**, 6745–6750.
- 37 B. Sharma, K. Ma, M. R. Glucksberg and R. P. Van Duyne, *J. Am. Chem. Soc.*, 2013, **135**, 17290–17293.
- 38 W. E. Doering, M. E. Piotti, M. J. Natan and R. G. Freeman, *Adv. Mater.*, 2007, **19**, 3100–3108.
- 39 M. J. Natan, R. Cromer, W. E. Doering and I. D. Walton, Polymer coated SERS nanotag, *US pat.*, US7723100 B2, 2010.
- 40 S. E. Bohndiek, A. Wagadarikar, C. L. Zavaleta, D. Van de Sompel, E. Garai, J. V. Jokerst, S. Yazdanfar and S. S. Gambhir, *Proc. Natl. Acad. Sci. U. S. A.*, 2013, **110**, 12408–12413.
- 41 C. L. Zavaleta, E. Garai, J. T. C. Liu, S. Sensarn, M. J. Mandella, D. Van de Sompel, S. Friedland, J. Van Dam, C. H. Contag and S. S. Gambhir, *Proc. Natl. Acad. Sci. U. S. A.*, 2013, **110**, E2288–E2297.
- 42 M. F. Kircher, A. de la Zerda, J. V. Jokerst, C. L. Zavaleta, P. J. Kempen, E. Mittra, K. Pitter, R. Huang, C. Campos, F. Habte, R. Sinclair, C. W. Brennan, I. K. Mellinghoff, E. C. Holland and S. S. Gambhir, *Nat. Med.*, 2012, **18**, 829–834.
- 43 E. Garai, S. Sensarn, C. L. Zavaleta, N. O. Loewke, S. Rogalla, M. J. Mandella, S. A. Felt, S. Friedland, J. T. C. Liu, S. S. Gambhir and C. H. Contag, *PLoS ONE*, 2015, **10**, e0123185.
- 44 K. Carron and R. Cox, *Anal. Chem.*, 2010, **82**, 3419–3425.
- 45 B. Sharma, R. R. Frontiera, A.-I. Henry, E. Ringe and R. P. Van Duyne, *Mater. Today*, 2012, **15**, 16–25.



- 46 M. O. McAnally, B. T. Phelan, R. M. Young, M. R. Wasielewski, G. C. Schatz and R. P. Van Duyne, *Anal. Chem.*, 2017, **89**, 6931–6935.
- 47 O. Lyandres, N. C. Shah, C. R. Yonzon, J. T. Walsh, M. R. Glucksberg and R. P. Van Duyne, *Anal. Chem.*, 2005, **77**, 6134–6139.
- 48 B. Sharma, P. Bugga, L. R. Madison, A.-I. Henry, M. G. Blaber, N. G. Greeneltch, N. Chiang, M. Mrksich, G. C. Schatz and R. P. Van Duyne, *J. Am. Chem. Soc.*, 2016, **138**, 13952–13959.
- 49 T. D. James, M. D. Phillips and S. Shinkai, in *Boronic Acids in Saccharide Recognition*, The Royal Society of Chemistry, 2006, pp. 3–176, DOI: 10.1039/9781847557612-00003.
- 50 J. A. Dieringer, R. B. Lettan, K. A. Scheidt and R. P. Van Duyne, *J. Am. Chem. Soc.*, 2007, **129**, 16249–16256.
- 51 J. P. Camden, J. A. Dieringer, Y. Wang, D. J. Masiello, L. D. Marks, G. C. Schatz and R. P. Van Duyne, *J. Am. Chem. Soc.*, 2008, **130**, 12616–12617.
- 52 A. M. Michaels, M. Nirmal and L. E. Brus, *J. Am. Chem. Soc.*, 1999, **121**, 9932–9939.
- 53 A. M. Michaels, J. Jiang and L. Brus, *J. Phys. Chem. B*, 2000, **104**, 11965–11971.
- 54 M. D. Sonntag, J. M. Klingsporn, L. K. Garibay, J. M. Roberts, J. A. Dieringer, T. Seideman, K. A. Scheidt, L. Jensen, G. C. Schatz and R. P. Van Duyne, *J. Phys. Chem. C*, 2012, **116**, 478–483.
- 55 N. Chiang, X. Chen, G. Goubert, D. V. Chulhai, X. Chen, E. A. Pozzi, N. Jiang, M. C. Hersam, T. Seideman, L. Jensen and R. P. Van Duyne, *Nano Lett.*, 2016, **16**, 7774–7778.
- 56 D. Kurouski, M. Mattei and R. P. Van Duyne, *Nano Lett.*, 2015, **15**, 7956–7962.
- 57 Z.-C. Zeng, S.-C. Huang, D.-Y. Wu, L.-Y. Meng, M.-H. Li, T.-X. Huang, J.-H. Zhong, X. Wang, Z.-L. Yang and B. Ren, *J. Am. Chem. Soc.*, 2015, **137**, 11928–11931.
- 58 M. Mattei, G. Kang, G. Goubert, D. V. Chulhai, G. C. Schatz, L. Jensen and R. P. Van Duyne, *Nano Lett.*, 2017, **17**, 590–596.
- 59 N. Martín Sabanés, T. Ohto, D. Andrienko, Y. Nagata and K. F. Domke, *Angew. Chem., Int. Ed.*, 2017, **56**, 9796–9801.
- 60 A. J. Wilson and K. A. Willets, *Analyst*, 2016, **141**, 5144–5151.
- 61 C. E. Harvey and B. M. Weckhuysen, *Catal. Lett.*, 2015, **145**, 40–57.
- 62 S. Zaleski, A. J. Wilson, M. Mattei, X. Chen, G. Goubert, M. F. Cardinal, K. A. Willets and R. P. Van Duyne, *Acc. Chem. Res.*, 2016, **49**, 2023–2030.
- 63 S. Zaleski, M. F. Cardinal, D. V. Chulhai, A. J. Wilson, K. A. Willets, L. Jensen and R. P. Van Duyne, *J. Phys. Chem. C*, 2016, **120**, 24982–24991.
- 64 S. Zaleski, M. F. Cardinal, J. M. Klingsporn and R. P. Van Duyne, *J. Phys. Chem. C*, 2015, **119**, 28226–28234.
- 65 N. Jiang, N. Chiang, L. R. Madison, E. A. Pozzi, M. R. Wasielewski, T. Seideman, M. A. Ratner, M. C. Hersam, G. C. Schatz and R. P. Van Duyne, *Nano Lett.*, 2016, **16**, 3898–3904.
- 66 J. M. Klingsporn, N. Jiang, E. A. Pozzi, M. D. Sonntag, D. Chulhai, T. Seideman, L. Jensen, M. C. Hersam and R. P. V. Duyne, *J. Am. Chem. Soc.*, 2014, **136**, 3881–3887.
- 67 E. A. Pozzi, G. Goubert, N. Chiang, N. Jiang, C. T. Chapman, M. O. McAnally, A.-I. Henry, T. Seideman, G. C. Schatz, M. C. Hersam and R. P. V. Duyne, *Chem. Rev.*, 2017, **117**, 4961–4982.



- 68 E. A. Pozzi, N. L. Gruenke, N. Chiang, D. V. Zhdanov, N. Jiang, T. Seideman, G. C. Schatz, M. C. Hersam and R. P. Van Duyne, *J. Phys. Chem. Lett.*, 2016, **7**, 2971–2976.
- 69 B. Sharma, M. Fernanda Cardinal, S. L. Kleinman, N. G. Greeneltch, R. R. Frontiera, M. G. Blaber, G. C. Schatz and R. P. Van Duyne, *MRS Bull.*, 2013, **38**, 615–624.
- 70 Over 6200 published paper found (~800 in 2016) when searching ‘SERS substrates’ in the Web of Science (Clarivate Analytics) database.
- 71 N. G. Greeneltch, M. G. Blaber, A.-I. Henry, G. C. Schatz and R. P. Van Duyne, *Anal. Chem.*, 2013, **85**, 2297–2303.
- 72 X. Zhang, J. Zhao, A. V. Whitney, J. W. Elam and R. P. Van Duyne, *J. Am. Chem. Soc.*, 2006, **128**, 10304–10309.
- 73 L. E. Kreno, N. G. Greeneltch, O. K. Farha, J. T. Hupp and R. P. Van Duyne, *Analyst*, 2014, **139**, 4073–4080.
- 74 M. A. Bañares, *Catal. Today*, 2005, **100**, 71–77.
- 75 R. A. Hackler, M. O. McAnally, G. C. Schatz, P. C. Stair and R. P. Van Duyne, *J. Am. Chem. Soc.*, 2017, **139**, 2456–2463.
- 76 B. Sharma, M. F. Cardinal, M. B. Ross, A. B. Zrimsek, S. V. Bykov, D. Punihaole, S. A. Asher, G. C. Schatz and R. P. Van Duyne, *Nano Lett.*, 2016, **16**, 7968–7973.
- 77 N. L. Gruenke, M. O. McAnally, G. C. Schatz and R. P. Van Duyne, 2016.
- 78 E. M. Hicks, O. Lyandres, W. P. Hall, S. Zou, M. R. Glucksberg and R. P. Van Duyne, *J. Phys. Chem. C*, 2007, **111**, 4116–4124.

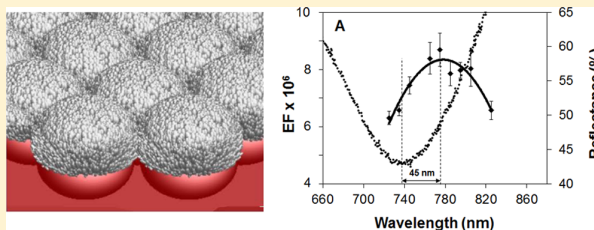
# Unraveling the Near- and Far-Field Relationship of 2D Surface-Enhanced Raman Spectroscopy Substrates Using Wavelength-Scan Surface-Enhanced Raman Excitation Spectroscopy

Dmitry Kurouski,<sup>\*,†</sup> Nicolas Large,<sup>‡</sup> Naihao Chiang,<sup>§</sup> Anne-Isabelle Henry, Tamar Seideman, George C. Schatz,<sup>§</sup> and Richard P. Van Duyne<sup>\*,§</sup>

Department of Chemistry, Northwestern University, 2145 Sheridan Road, Evanston, Illinois 60208, United States

## Supporting Information

**ABSTRACT:** Lithographic and nonlithographic two-dimensional (2D) substrates for surface-enhanced Raman spectroscopy (SERS) have gained enormous popularity as analytical platforms for detection and identification of various analytes. However, their near- and far-field properties in most cases remain poorly understood. We have previously developed a metal nanopillar film over nanospheres (FON) platform exhibiting Raman enhancement factors of  $\sim 10^7$ . These substrates have a reproducible and predictable localized surface plasmon resonance throughout the entire visible region and much of the near-IR region of the electromagnetic spectrum. Extending upon these results, we have utilized wavelength-scan surface-enhanced Raman excitation spectroscopy to unravel the relationship between near- and far-field properties of FON surface-enhanced Raman spectroscopy substrates. We examined by scanning electron microscopy FONs fabricated by either stationary (ST-FONs) or spun (SP-FONs) metal deposition to examine the interrelationships of nanoscale structure and near- and far-field properties. We demonstrate that the line width and spectral position of the far-field and near-field resonances of ST- and SP-FONs directly depend on the nanofeature distribution at the metallic surface. In particular, we show that the actual nanofeature morphology and distribution directly impact the spectral alignment of the far-field and near-field resonances.



## INTRODUCTION

Surface-enhanced Raman spectroscopy (SERS) is a powerful analytical technique that is capable of detecting molecular analytes down to the single-molecule level.<sup>1,2</sup> Electromagnetic enhancement is demonstrated to be the dominant mechanism contributing to the SERS enhancement.<sup>3</sup> It involves the localization and amplification of the incident optical excitation by surface plasmon resonances (localized and propagating) of noble-metal nanoparticles.<sup>4–7</sup> Localized surface plasmon resonances (LSPRs) are coherent, incompressible, collective oscillations of the conduction electron gas sustained by noble-metal nanoparticles and nanostructured surfaces. They are responsible for drastic enhancement of the local electric field ( $E$ ) in the vicinity of the metallic nanofeatures, which can reach  $10^2$ – $10^3$  times the incident electric field ( $E_0$ ).<sup>8</sup> The LSPR strongly depends on the plasmonic nanofeature size, shape, material, and local dielectric environment.<sup>9–13</sup> Therefore, in principle, the knowledge of the LSPR spectral properties, which can be obtained from the far-field scattering spectrum, should be sufficient to determine the excitation wavelength that would give the highest enhancement factor ( $EF \approx |E/E_0|^4$ ) for a given SERS substrate.

Chemically synthesized gold and silver nanoparticles have been routinely used for single-molecule SERS experiments, where their aggregation into nanoparticle clusters provides the

sites for electromagnetic field enhancement, also known as hot spots.<sup>14–17</sup> Nanoparticle synthesis is versatile, allowing for tailoring the sizes and geometries of the nanoparticles to fulfill particular experimental needs.<sup>18–22</sup> Recently, numerous different kinds of nanoparticles with built-in hot spots, i.e., eliminating the need for nanoparticle aggregation, have been reported. They include porous nanoparticles, octopods/nanostars, octahedra, concave, truncated, and etched nanocubes, and nanocuboids.<sup>18,22–26</sup> However, nanoparticle synthesis scale-up can be difficult to implement and often results in an increase of the size polydispersity. Furthermore, precursors of their synthesis, such as cetyltrimethylammonium bromide (CTAB) and citric acid, commonly overcomplicate their practical applications in surface-enhanced spectroscopies and sensing.<sup>9,27</sup>

Removal of these surfactants commonly leads to random aggregation and precipitation of the metallic nanoparticles, which prevents reproducibility of the resulting SERS enhancement.

Two-dimensional (2D) SERS substrates are ideally suited platforms for the detection of analytes as they provide adequate nanofeatures without the need for stabilizing adsorbants that

Received: May 17, 2017

Revised: June 22, 2017

Published: June 22, 2017



could in fine limit the SERS efficiency by blocking the analytes' access to the metal surface. The bare metallic nanostructured film can then potentially be later functionalized with specific capture ligands.<sup>28,29</sup> Over the last couple decades, several SERS substrates have been proposed, including films over nanospheres (FONs),<sup>30,31</sup> colloidal crystal films,<sup>32</sup> nanoparticle arrays,<sup>33–38</sup> particles grafted on silanized glasses,<sup>39,40</sup> paper-based three-dimensional (3D) SERS substrates,<sup>41</sup> and plasmonic nanoholes.<sup>18,22,26,42</sup> On the basis of the fabrication techniques used, there are several types of SERS platforms. The fabrication of nonlithographic substrates is commonly carried out through a thermal evaporation of plasmonic metals on a glass or silicon substrate.<sup>43</sup> This results in generation of nanometer-scale plasmonic features.<sup>44,45</sup> Although the fabrication of nonlithographic substrates such as metal islands or porous films is relatively facile and provides reasonable SERS enhancement ( $10^4$ – $10^6$ ), the lack of control in the density of hot spots on the substrate makes it difficult to use as a reliable substrate. Lithographic substrates are characterized by well-defined nanostructures at specific locations on the substrate and hence achieve high SERS enhancement factors (typically  $10^6$ – $10^8$ ).<sup>46–48</sup>

Electron-beam lithography (EBL) is one of the commonly used methods to fabricate nanoparticle arrays with tunable interparticle distances and shapes.<sup>49,50</sup> However, high labor intensity and time consumption of EBL-based substrates and high fabrication costs limit their broad and large-scale utilization.<sup>48</sup> A well-developed type of lithographic substrate is the FON, which is fabricated by metal evaporation on a mask of close-packed silica or polystyrene spheres.<sup>30,31,47</sup> It was previously demonstrated that LSPR of FONs could be tuned between 330 and 1840 nm by varying the diameter of the silica or polystyrene spheres. Moreover, FONs exhibit one of the highest reported EFs of  $10^8$  with only 10% variability over substrates of 10 cm diameter. It was also noted that, as a result of metal deposition over the close-packed silica or polystyrene spheres, two major types of nanofeatures are grown: elongated nanopillars and nanoscale blobs. Greeneltch et al. showed that substrate spinning during the metal deposition promotes the formation of nanopillars.<sup>51</sup> These spun FON substrates (SP-FONs) exhibited EFs nearly an order of magnitude higher than those of FONs prepared under stationary conditions (ST-FONs). However, it remains unclear how different the distributions of nanofeatures are and how their size, shape, and overall morphology affect the relationship between the near- and far-field properties of these FON substrates. The morphological differences in an SERS substrate family can lead to complex near- to far-field relationships.<sup>41</sup> Elucidation of such relationships allows for even more precise tuning and tailoring of the LSPR of the FON substrate, thus leading to a better optimization of its SERS performance.

Wavelength-scan surface-enhanced Raman excitation spectroscopy (WS-SERES) is capable of unraveling the near-field properties of SERS substrates. Using WS-SERES, Doherty et al. previously demonstrated that highly uniform SERS substrates exhibit a  $\sim 50$  nm red shift of their near-field maximum compared to the maximum of their optical scattering profile.<sup>33</sup> McFarland et al. observed that near- and far-field profiles of periodic particle arrays (PPAs) would overlap if the substrate was annealed at 300 °C for 1 h.<sup>52</sup> Finally, WS-SERES was recently used to investigate the near-field properties of paper- and fabric-based 3D SERS substrates, which demonstrated extremely weak optical scattering.<sup>41</sup> It was found that

nanoparticle dimers and trimers and higher order nanoparticle clusters primarily determine the near-field properties of these substrates. It should be noted that SERS signals are mainly generated at hot spots at plasmonic substrates; thus, SERS excitation spectral shapes are considerably affected by the near-field optical profiles of hot spots that are different from the far-field optical profiles of the overall plasmonic substrates. At the same time, the far-field response of 3D SERS substrates either was shown to primarily originate from the monomers or could not be clearly defined.

In the present study, we have utilized WS-SERES, scanning electron microscopy (SEM), optical scattering, and finite-difference time-domain (FDTD) calculations to explore the near- and far-field properties of FON substrates. Specifically, we unravel the effect of the FON nanofeature distributions on the correlation between the near- and far-field responses of these SERS substrates. We noticed that spun deposition of Ag resulted in the predominant formation of nanopillars on the surface of the FONs. On the other hand, stationary deposition of Au led to nearly exclusive growth of nanoscale blobs. Here, we used these peculiarities of metal deposition to promote the growth of two different kinds of nanofeatures, i.e., nanopillars (SP-FON) and nanoscale blobs (ST-FON), on the surface of FONs. New structural models of both FON structures have been developed, and electrodynamics calculations are used with these models to provide a quantitative description of the observed optical properties.

## METHODS

**Fabrication of SERS Substrates.** Both SP- and ST-FON SERS substrates were prepared by packing silicon spheres (600 and 540 nm, respectively) on freshly cleaned silicon wafers, as previously described in ref 51. A 200 nm layer of Ag was deposited on the spheres while the substrates were spun at  $\sim 550$  rpm (homemade thermal evaporator) for the SP-FONs. ST-FONs were prepared by evaporation of 150 nm of Au on stationary hold substrates (PVD 75, Kurt J. Lesker, Efferson Hills, PA). Benzenethiol (Sigma-Aldrich, St. Louis, MO) was vapor-deposited onto the ST- and SP-FON SERS substrates by placing 3–4 drops of concentrated (100%) benzenethiol solution in a Petri dish around the substrate. The substrates were left overnight in the atmosphere of benzenethiol vapors and then immediately measured using WS-SERES.

Cyclohexane (Sigma-Aldrich) was used as an intensity standard ( $1028.3\text{ cm}^{-1}$  normal Raman scattering band) for a correction of the inherent  $\nu^4$  behavior of Raman scattering. Specifically, the intensity of the  $1075\text{ cm}^{-1}$  band of benzenethiol, which was used as a reported SERS signal for all substrates, was divided by the intensity of the  $1028.3\text{ cm}^{-1}$  band of cyclohexane to obtain the SERS efficiency at each excitation wavelength. Such normalization also allows us to eliminate variations in the SERS intensity that are not due to enhancement by the substrate, as well as the spectral dependence of the detection system.<sup>52</sup>

**Raman Spectroscopy.** SERS and normal Raman spectra were collected on an inverted microscope (Nikon TE-300) equipped with a 20 $\times$  dry Nikon objective (numerical aperture (NA) of 0.45) from the same area of the SERS substrate as that from which the reflection spectra were captured. A diode-pumped solid-state laser, Spectra-Physics (Mountain View, CA) Millennia Xs, was used for 532 nm excitation. It was also used to drive the tunable Ti:sapphire oscillator to generate wavelengths from 725 to 825 nm. A Spectra-Physics He–Ne diode-based

laser was used to generate a 633 nm laser excitation. The laser spot size was approximately  $2.7\ \mu\text{m} \times 1.8\ \mu\text{m}$ . The signal was collected in a backscattering configuration and directed to a confocal Raman spectrometer (Princeton Instruments, SP2500i) equipped with a 1200 groove/mm grating blazed at 500 nm (532 nm excitation) or a 600 groove/mm grating blazed at 750 nm (633 and 725–825 nm excitations) with the slit entrance set to 100  $\mu\text{m}$ . Prior to the signal entering the spectrograph, Rayleigh scattering was filtered with a long-pass filter (Semrock, LP03-532RS-25 (532 nm excitation) or LP03-633RS-25 (633 nm excitation)). To filter the Rayleigh scattering at 725–825 nm excitations, a 900/11 nm VersaChrome tunable band-pass filter was used. The dispersed light was then sent to a liquid nitrogen-cooled charge-coupled device (CCD) (Action300i, Spec-10 400B). A motorized stage (Physik Instrumente, 710 Digital PZT) was used to move the sample relative to the incident laser beam. All data were processed using GRAMS/AI 7.0 (Thermo Galactic, Salem, NH).

**UV–Vis Spectroscopy.** Scattering spectra (400–900 nm) were recorded by illuminating the sample with the microscope lamp and analyzing the transmitted light by a fiber-optically coupled Ocean Optics spectrometer (SD200, Ocean Optics, Dundee, FL).<sup>51,47</sup> The size of the light spot was approximately 1 mm in diameter. The spot to spot variations in the reflectance were negligible (Figure 1S).  $T_{\text{aqu}} = 10\ \text{ms}$ , with 103 averages. Silver and gold films with the same metal thickness as was deposited on the investigated substrates were used as a reference to reach 100% transmission.

**Scanning Electron Microscopy.** SEM images were acquired with a LEO Gemini 1525 microscope using an InLens detector, operating at an acceleration voltage of 5.00 kV. The working distance was varied between 3 and 7 mm.

**Electrodynamic Calculations.** FDTD simulations were performed using the commercial package Lumerical FDTD Solutions<sup>53</sup> to calculate the plasmonic properties (reflectance and near-field) of the FON substrates. The FONs were modeled on the basis of the SEM data. The silica spheres were modeled with diameters of 600 and 540 nm for the ST-FON and SP-FON, respectively, and are arranged in a hexagonal lattice on a semi-infinite silica substrate. The ST-FON was modeled with a  $200 \pm 10\ \text{nm}$  metallic layer constituted of approximately 3000 elongated spheroids of sizes ranging from 5 to 20 nm randomly distributed on top of each microsphere. Similarly, the SP-FON was modeled with a  $150 \pm 10\ \text{nm}$  metallic layer constituted of  $\sim 3000$  randomly distributed 15–20 nm spherical grains. The two FDTD-modeled geometries are shown in Figure 3. Periodic boundary conditions and symmetries were used in the in-plane directions to mimic infinite arrays, and perfectly matched layers (PMLs) were assumed along the out-of-plane direction. Dielectric permittivities tabulated by Palik and by Johnson and Christy were used for Ag and Au, respectively.<sup>54,55</sup> The optical excitation was taken as a broad-band plane-wave source (total-field scattered-field, TFSF, source). A nonuniform conformal mesh with a minimum mesh size of 0.25 nm was used to describe the overall nanostructures. An auto-shutoff parameter of  $10^{-6}$  was chosen as the convergence parameter, allowing a propagation time  $\tau \approx 10\ \text{ns}$  of the electromagnetic fields. The reflectance spectra were averaged over 15 different morphologies (i.e., nanofeature distributions) to account for experimental heterogeneities.

## RESULTS AND DISCUSSION

Electron microscopy examination provides a means to evaluate the structural uniformity of a substrate, as well as providing information about the size and shape of the observed nanofeatures. This information is commonly used as an input for theoretical and numerical calculations of the substrate near- and far-field properties. We used SEM to examine the morphology of the nanostructured metal film and characterize the shape and sizes of the nanofeatures present at the surface of both ST- and SP-FONs (Figure 1). The morphological analysis

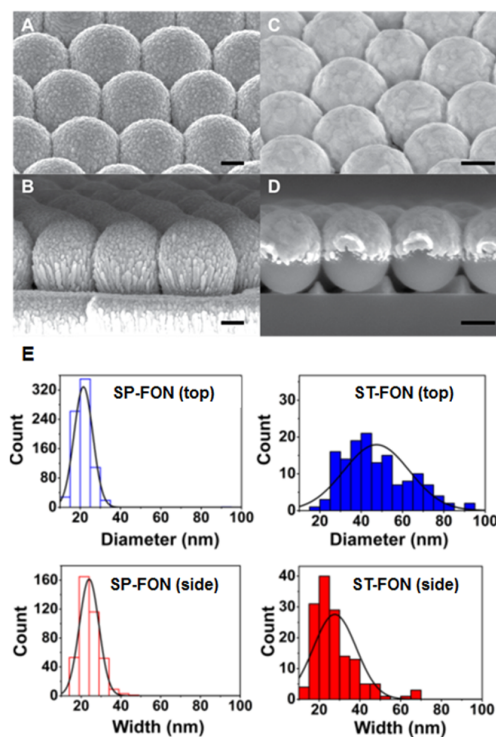


**Figure 1.** SEM images of SP-FONs (A, B) and ST-FONs (C, D). Scale bars correspond to 200 nm (A, B) and 300 nm (C, D). (E) Size distributions of nanofeatures on the top (upper panels) and side (lower panels) surfaces of SP- and ST-FONs.

reveals that SP-FONs had average feature sizes of  $24 \pm 5$  and  $22 \pm 5\ \text{nm}$  with a full width at half-maximum (fwhm) of 10 nm in the top and side views, respectively. As for the other substrates, namely, ST-FONs, average nanofeature sizes of  $28 \pm 11$  and  $47 \pm 16\ \text{nm}$  with fwhm's of 20 and 70 nm were observed in the top and side views, respectively. From these data on the side and top views, nanofeatures on ST-FONs appear very asymmetric (28 and 47 nm, respectively), in contrast to their counterparts on the SP-FONs (24 and 22 nm, respectively).

We further characterized the SP-FONs and ST-FONs by measuring both their near- and far-field responses. The near-field SERS response was measured using WS-SERES from nine different, nonoverlapping spots on three SP-FON and two ST-FON substrates. The excitation wavelength employed in all the measurements was tuned from 725 to 825 nm, in increments of 10 nm (Figure 2). Benzenethiol (BZT; inset in Figure 2A) was used as the probed analyte because it forms a monolayer on the metal surface and is not resonant in the 600–900 nm spectral



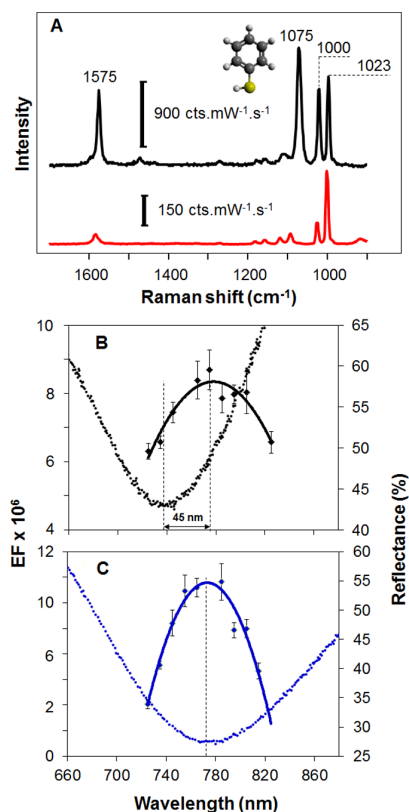


**Figure 2.** (A) SERS (black) and normal Raman (red) spectra of benzenethiol (BZT) acquired with 785 nm excitation,  $P = 50 \mu\text{W}$ , and  $T = 10 \text{ s}$ . (B, C) Near-field profiles (EF, solid line) and far-field optical responses (reflectance, dotted line) of ST-FONs (B) and SP-FONs (C).

window. Overnight exposition of ST- and SP-FON substrates in the atmosphere of BZT results in the formation of a BZT

monolayer on the metal surface. A typical SERS spectrum obtained from such a metallic surface is shown in Figure 2A (black line). It should be noted that the SERS spectra of BZT acquired from ST-FONs and SP-FONs are very similar to each other. A normal Raman spectrum of BZT is also shown for comparison (Figure 2A, red line). Finally, the optical scattering responses of both ST- and SP-FONs were also obtained by a home-built UV-vis apparatus.<sup>51</sup>

Both ST- and SP-FONs exhibit Gaussian near-field profiles with the maxima around 755–775 nm. ST-FONs (Figure 2B) showed nearly similar enhancement in the 750–790 nm range ( $\text{EF} \approx 8.3 \times 10^6$ ). We also found that the EF of ST-FONs decreased by nearly a factor of 2 at 725 and 825 nm relative to the maximum, giving rise to an fwhm of  $\sim 75 \text{ nm}$ , slightly broader than that of their SP-FON counterparts (fwhm of  $\sim 65 \text{ nm}$ , Figure 2C). The highest enhancement is found at 755–775 nm, which corresponds to  $\text{EF} \approx 1 \times 10^7$ . The second largest enhancements were measured at 745, 785, and 795 nm ( $\text{EF} \approx 8.3 \times 10^6$ ). Finally, the lowest EF for SP-FONs was observed at 725 nm ( $\text{EF} \approx 2 \times 10^6$ ). The far-field properties exhibit opposite behaviors as shown by the reflectance spectra (Figure 2B,C, dotted lines). The spectrum of the SP-FON substrates appears to be broader than the scattering profile of ST-FONs (fwhm of 160 nm vs 110 nm). Interestingly, we can also notice that the maxima for the far-field scattering and for the near-field response are spectrally aligned in the case of the SP-FONs (Figure 2C). On the other hand, the maximum of the near-field response of the ST-FON is red-shifted by about 45 nm with respect to the reflectance (far-field) maximum (Figure 2B).

To gain further insight into the structure–property relationships of the FON substrates and further understand the relationship between the near- and far-field properties, we have used the FDTD method to calculate the near- and far-field properties of both ST- and SP-FONs (Figure 3A,B, respectively). Due to the structural complexity of these substrates, FDTD calculations were performed for 15 different morphologies (i.e., different surface roughness distributions) and averaged out. The far-field optical properties are also

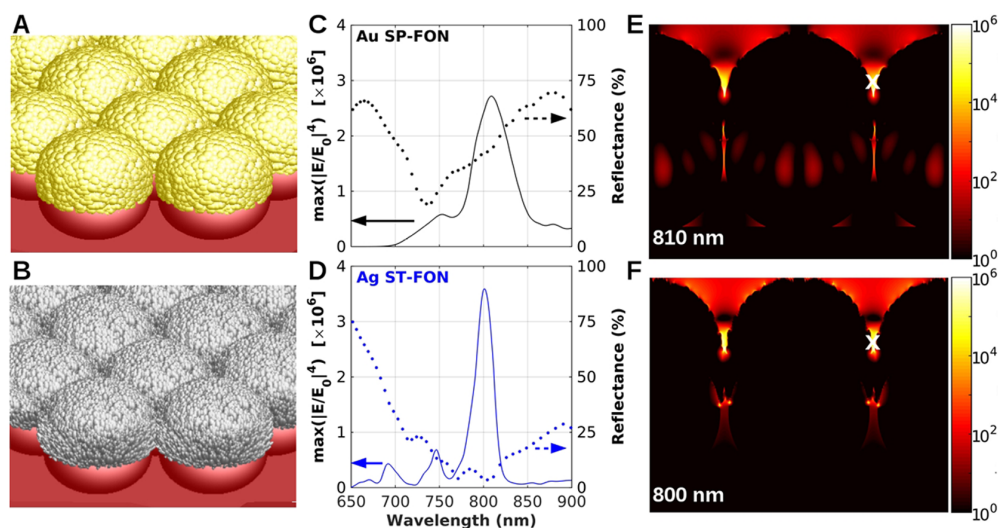


**Figure 3.** FDTD calculations for the ST- and SP-FONs. (A, B) Modeled geometries used in the FDTD simulations for the Au ST-FON and Ag SP-FON, respectively. (C, D) Reflectance spectra (dotted lines) and fourth power of the near field ( $|E/E_0|^4$ , solid line) calculated within the gap (white mark in panels E and F) for the Au ST-FON and Ag SP-FON, respectively. (E, F) Spatial distribution of  $|E/E_0|^4$  around the Au ST-FON ( $\lambda = 810 \text{ nm}$ ) and Ag SP-FON ( $\lambda = 800 \text{ nm}$ ), respectively.

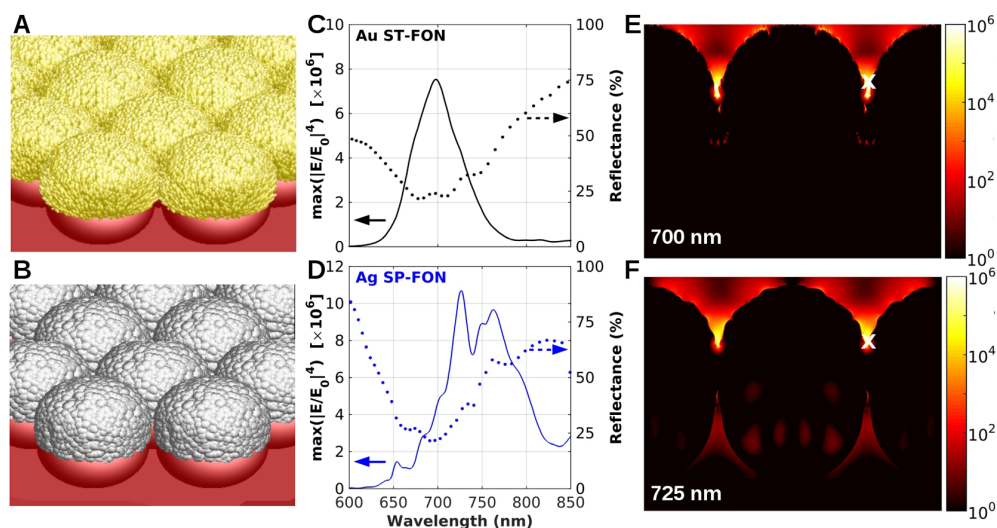


**Figure 4.** FDTD calculations for the SP- and ST-FONs. (A, B) Modeled geometries used in the FDTD simulations for the Au SP-FON and Ag ST-FON, respectively. (C, D) Reflectance spectra (dotted lines) and fourth power of the near field ( $|E/E_0|^4$ , solid line) calculated within the gap (white mark in panels E and F) for the Au SP-FON and Ag ST-FON, respectively. (E, F) Spatial distribution of  $|E/E_0|^4$  around the Au SP-FON ( $\lambda = 700$  nm) and Ag ST-FON ( $\lambda = 725$  nm), respectively.

polarization averaged. The simulation details are provided in the **Methods**. As the SERS signal is experimentally dominated by strong plasmonic hot spots present at the surface of the metallic nanostructured film, we calculate the near-field response in the gap regions, i.e., where the local electric field intensity is the highest (white mark in **Figure 3E,F**). Similarly to the experimental results, we have found that the maximum of the near-field response (i.e.,  $\max(|E/E_0|^4)$ ) of the ST-FON is red-shifted by  $\sim 60$  nm with respect to the reflectance minimum, as shown in **Figure 3C**. However, the SP-FON does not exhibit such a noticeable spectral shift as can be seen from **Figure 3D**. Instead, near- and far-field profiles of SP-FON appeared to be spectrally aligned as observed experimentally. Additionally, and very similarly to the experimental observations, the reflectance profile of Ag SP-FONs appears much broader than that of Au ST-FONs. These results are in excellent quantitative agreement with the WS-SERS results presented in **Figure 2**. Note also that the maximum experimental and calculated enhancements for both ST-FONs and SP-FONs are similar and are on the order of  $10^6$  to  $10^7$ . It is important to notice that although the morphology is modeled with random surface roughness, small discrepancies in the spectral line shape can be attributed to the high surface heterogeneity of the actual FONs, thus leading to large inhomogeneous spectral broadening.

Parts E and F of **Figure 3** show the near-field spatial distribution ( $|E/E_0|^4$ ) at the LSPR resonance (i.e., when the local electric field is the most intense). It can be seen that most of the near field is located in the gaps between the microspheres. However, due to the surface roughness, some localized hot spots can be found on top of the FON, in particular for the Ag SP-FON (**Figure 3F**). This is in agreement with previously published work on the distance dependence of SERS.<sup>56</sup> As can be seen from **Figure 3C–F**, the calculated EF reaches values on the order of  $3 \times 10^6$ , very good quantitative agreement with the experimental estimations.

To demonstrate that the observed relationship between near- and far-field responses is not due to the nature of the plasmonic

metal used in each of the investigated FONs, we have performed the same theoretical analysis with the complementary configurations. Specifically, we calculated the near- and far-field properties of Au SP-FONs and Ag ST-FONs (**Figure 4A,B**). As can be clearly noticed from **Figure 4D**, the maximum of the near-field response ( $\max(|E/E_0|^4)$ ) of the Ag ST-FON, similarly to the Au ST-FON in **Figure 3**, is red-shifted by about 50 nm with respect to the reflectance minimum. At the same time, both Au SP-FONs do not exhibit such a spectral shift (**Figure 4C**).

Unraveling the relationship between the far- and near-field optical responses of plasmonic materials is important to further understand the role and control the fabrication of nanoscale features underlying the SERS effect, as well as for the rational fabrication of SERS substrates and ultimately the optimization of their performance. However, to date, the inter-relationship between the nanoscale morphology of 2D substrates such as the ones found in the metal film of FONs and their properties is not clearly understood. Due to the intrinsic structural heterogeneity of these substrates at the nanoscale, the prediction of their optical far- and near-field properties using theoretical models is challenging. In the current study, we demonstrated that SEM allows for the visualization of morphological heterogeneity of nanostructures on the surfaces of both ST- and SP-FONs. However, these results alone cannot be used for prediction of the far- and near-field properties of FONs. For instance, according to the SEM images, nanopillars on the surface of the SP-FON are 25–30 nm in diameter. However, such nanostructures would exhibit LSPR at  $\sim 500$  nm, which was not experimentally observed.<sup>57,58</sup> Similarly, the size of the ST-FON nanostructures (28–47 nm) should give rise to a much broader far-field optical response than the optical response of SP-FONs (nanofeatures of 25–30 nm diameter). However, direct measurements of the optical scattering from ST- and SP-FONs showed the opposite (**Figure 2**), which is also supported by the FDTD calculations (**Figures 3 and 4**).

From the two sets of FDTD calculations, it clearly appears that the spectral shift observed experimentally with the ST-

FONs (Figure 2B), or the spectral alignment observed with ST-FONs (Figure 2C), is directly connected to the actual morphology of the FON rather than to the material. Spectral red shift between near-field and far-field resonances is commonly observed in plasmonic nanostructures. Using coupled harmonic oscillator models, Zuloaga and Nordlander showed that the amount of red shift varies on the basis of the total damping in the system.<sup>59</sup> Besides the intrinsic damping of the plasmonic materials, the total damping is directly governed by the type of morphological features forming the nanostructure (radiative damping). Small particles, or in the case of the ST-FONs small nanofeatures (i.e., nanopillars), have minimal radiative damping and very little intrinsic damping, resulting in a negligible red shift (or the absence of a red shift) of the near-field spectrum. As for SP-FONs, the small blobs tend to merge more easily than the nanopillars and form smoother and more continuous metallic films, thus resulting in overall larger features as can be seen in the FDTD models (Figures 3A and 4B). This effect further results in a significant increase of the radiative damping due to prominent retardation effects, leading to important spectral shifts. Furthermore, the actual size distribution of these nanofeatures also directly impacts the inhomogeneous damping of the system.

## CONCLUSIONS

In conclusion, we unraveled the interrelationships between the structure and near- and far-field properties of SERS substrates made of nanostructured metal films over nanospheres, known as FONs. Depending on the fabrication method (stationary vs spinning metal deposition, designated as ST-FONs and SP-FONs, respectively), we clearly confirmed by SEM analysis that it is possible to control the fine morphology of the metal film in the 10–90 nm range, with the resulting nanofeatures differing in their shape and size dispersity. Using WS-SERES, we directly measured the near-field SERS enhancement profile of both ST-FONs and SP-FONs and clearly showed that the near- and far-field profiles of SP-FONs were spectrally aligned, whereas a ~45 nm spectral shift was observed in the case of ST-FONs. The extensive numerical analysis revealed that the presence of nanofeatures presenting a small size polydispersity results in the spectral alignment of optical far-field and near-field profiles. The absence of, commonly observed, near- to far-field spectral shift is attributed to a significant increase in the radiative damping originating from the surface morphology of the FONs.

## ASSOCIATED CONTENT

### Supporting Information

The Supporting Information is available free of charge on the ACS Publications website at DOI: 10.1021/acs.jpcc.7b04787.

Spot to spot variations in the reflectance spectra of SP-FON (Figure S1) (PDF)

## AUTHOR INFORMATION

### Corresponding Authors

\*E-mail: dkurouski@gmail.com.

\*E-mail: vanduyne@northwestern.edu.

### ORCID

Dmitry Kurouski: 0000-0002-6040-4213

Nicolas Large: 0000-0002-2699-5718

Naihao Chiang: 0000-0003-3782-6546

George C. Schatz: 0000-0001-5837-4740

Richard P. Van Duyne: 0000-0001-8861-2228

### Present Addresses

<sup>†</sup>D.K.: Department of Biochemistry and Biophysics, Texas A&M University, 300 Olsen Blvd., College Station, TX 77843, United States.

<sup>‡</sup>N.L.: Department of Physics & Astronomy, The University of Texas at San Antonio, One UTSA Circle, San Antonio, TX 78249, United States.

### Author Contributions

D.K. and N.C. conceived and designed the experimental measurements. A.-I.H. performed the SEM structural analysis. N.L. performed the electrodynamic calculations and theoretical analysis.

### Notes

The authors declare no competing financial interest.

## ACKNOWLEDGMENTS

This work made use of the EPIC facility of Northwestern University's NUANCE Center, which has received support from the Soft and Hybrid Nanotechnology Experimental (SHyNE) Resource (National Science Foundation (NSF) Grant ECCS-1542205), the MRSEC program (NSF Grant DMR-1121262) at the Materials Research Center, the International Institute for Nanotechnology (IIN), the Keck Foundation, and the State of Illinois, through the IIN. This work was also supported by the NSF CaSTL Center (NSF Grant CHE-1414466) and by AFOSR MURI Grant FA9550-14-1-0003. N.L. acknowledges financial support from the Department of Physics and Astronomy and from the College of Science of The University of Texas at San Antonio. Computing resources were provided by the Quest high-performance computing facility at Northwestern University, which is jointly supported by the Office of the Provost, the Office for Research, and Northwestern University Information Technology (NUIT). This material is also based on research sponsored by the Air Force Research Laboratory under Agreement FA8650-15-2-5518. The views and conclusions contained herein are those of the authors and should not be interpreted as necessarily representing the official policies or endorsements, either expressed or implied, of the Air Force Research Laboratory or the U.S. Government. Finally, this work was supported by the Assistant Secretary of Defense for Health Affairs, through the Peer Reviewed Medical Research Program under Award No. W81XWH-16-1-0375. The opinions, interpretations, conclusions, and recommendations are those of the authors and are not necessarily endorsed by the Department of Defense.

## REFERENCES

- (1) Kneipp, K.; Wang, Y.; Kneipp, H.; Perelman, L. T.; Itzkan, I.; Dasari, R. R.; Feld, M. Single Molecule Detection Using Surface-Enhanced Raman Scattering (SERS). *Phys. Rev. Lett.* **1997**, *78*, 1667–1670.
- (2) Nie, S.; Emory, S. R. Probing Single Molecules and Single Nanoparticles by Surface-Enhanced Raman Scattering. *Science* **1997**, *275*, 1102–1106.
- (3) Schatz, G. C.; Yong, M. A.; Van Duyne, R. P. Electromagnetic Mechanism of SERS. In *Surface-Enhanced Raman Scattering: Physics and Applications*; Kneipp, K., Moskovits, M., Kneipp, H., Eds.; Springer, Berlin, 2006; Vol. 103; pp 19–46.
- (4) Moskovits, M. Surface Roughness and the Enhanced Intensity of Raman Scattering by Molecules Adsorbed on Metals. *J. Chem. Phys.* **1978**, *69*, 4159–4161.



- (5) Gersten, J.; Nitzan, A. Electromagnetic Theory of Enhanced Raman-Scattering by Molecules Adsorbed on Rough Surfaces. *J. Chem. Phys.* **1980**, *73*, 3023–3037.
- (6) Kerker, M.; Wang, D. S.; Chew, H. Surface Enhanced Raman Scattering (SERS) by Molecules Adsorbed at Spherical Particles. *Appl. Opt.* **1980**, *19*, 3373–3388.
- (7) King, F. W.; Van Duyne, R. P.; Schatz, G. C. Theory of Raman Scattering by Molecules Adsorbed on Electrode Surfaces. *J. Chem. Phys.* **1978**, *69*, 4472–4481.
- (8) Hao, E.; Schatz, G. C. Electromagnetic Fields Around Silver Nanoparticles and Dimers. *J. Chem. Phys.* **2004**, *120*, 357–366.
- (9) Martinsson, E.; Shahjamali, M. M.; Large, N.; Zaree, N.; Zhou, Y.; Schatz, G. C.; Mirkin, C. A.; Aili, D. Influence of Surfactant Bilayers on the Refractive Index Sensitivity and Catalytic Properties of Anisotropic Gold Nanoparticles. *Small* **2016**, *12*, 330–342.
- (10) Kelly, K. L.; Coronado, E.; Zhao, L. L.; Schatz, G. C. The Optical Properties of Metal Nanoparticles: the Influence of Size, Shape, and Dielectric Environment. *J. Phys. Chem. B* **2003**, *107*, 668–677.
- (11) Wustholz, K. L.; Henry, A. I.; McMahon, J. M.; Freeman, R. G.; Valley, N.; Piotti, M. E.; Natan, M. J.; Schatz, G. C.; Van Duyne, R. P. Structure-Activity Relationships in Gold Nanoparticle Dimers and Trimers for Surface-Enhanced Raman Spectroscopy. *J. Am. Chem. Soc.* **2010**, *132*, 10903–10910.
- (12) Haes, A. J.; Haynes, C. L.; McFarland, A. D.; Schatz, G. C.; Van Duyne, R. P.; Zou, S. Plasmonic Materials for Surface-Enhanced Sensing and Spectroscopy. *MRS Bull.* **2005**, *30*, 368–375.
- (13) Ringe, E.; McMahon, J. M.; Sohn, K.; Cobley, C.; Xia, Y.; Huang, J.; Schatz, G. C.; Marks, L. D.; Van Duyne, R. P. Unraveling the Effects of Size, Composition, and Substrate on the Localized Surface Plasmon Resonance Frequencies of Gold and Silver Nanocubes: A Systematic Single-Particle Approach. *J. Phys. Chem. C* **2010**, *114*, 12511–12516.
- (14) Zrimsek, A. B.; Wong, N.; Van Duyne, R. P. Single Molecule Surface-Enhanced Raman Spectroscopy: A Critical Analysis of the Bianalyte vs. Isotopologue Proof. *J. Phys. Chem. C* **2016**, *120*, 5133–5142.
- (15) Kleinman, S. L.; Frontiera, R. R.; Henry, A. I.; Dieringer, J. A.; Van Duyne, R. P. Creating, Characterizing, and Controlling Chemistry with SERS Hot Spots. *Phys. Chem. Chem. Phys.* **2013**, *15*, 21–36.
- (16) Kleinman, S. L.; Ringe, E.; Valley, N.; Wustholz, K. L.; Phillips, E.; Scheidt, K. A.; Schatz, G. C.; Van Duyne, R. P. Single-Molecule Surface-Enhanced Raman Spectroscopy of Crystal Violet Isotopologues: Theory and Experiment. *J. Am. Chem. Soc.* **2011**, *133*, 4115–4122.
- (17) Large, N.; Saviot, L.; Margueritat, J.; Gonzalo, J.; Afonso, C. N.; Arbouet, A.; Langot, P.; Mlayah, A.; Aizpurua, J. Acousto-Plasmonic Hot Spots in Metallic Nano-Objects. *Nano Lett.* **2009**, *9*, 3732–3738.
- (18) Zhang, Q.; Large, N.; Wang, H. Gold Nanoparticles with Tipped Surface Structures as Substrates for Single-Particle Surface-Enhanced Raman Spectroscopy: Concave Nanocubes, Nanotrisoctahedra, and Nanostars. *ACS Appl. Mater. Interfaces* **2014**, *6*, 17255–17267.
- (19) Betz, J. F.; Yu, W. W.; Cheng, Y.; White, I. M.; Rubloff, G. W. Simple SERS Substrates: Powerful, Portable, and Full of Potential. *Phys. Chem. Chem. Phys.* **2014**, *16*, 2224–2239.
- (20) Kurouski, D.; Sorci, M.; Postiglione, T.; Belfort, G.; Lednev, I. K. Detection and Structural Characterization of Insulin Prefibrillar Oligomers Using Surface Enhanced Raman Spectroscopy. *Biotechnol. Prog.* **2014**, *30*, 488–495.
- (21) Ringe, E.; Zhang, J.; Langille, M. R.; Mirkin, C. A.; Marks, L. D.; Van Duyne, R. P. Correlating the Structure and Localized Surface Plasmon Resonance of Single Silver Right Bipyramids. *Nanotechnology* **2012**, *23*, 444005.
- (22) Zhang, Q.; Large, N.; Nordlander, P.; Wang, H. Porous Au Nanoparticles with Tunable Plasmon Resonances and Intense Field Enhancements for Single-Particle SERS. *J. Phys. Chem. Lett.* **2014**, *5*, 370–374.
- (23) Mulvihill, M. J.; Ling, X. Y.; Henzie, J.; Yang, P. Anisotropic Etching of Silver Nanoparticles for Plasmonic Structures Capable of Single-Particle SERS. *J. Am. Chem. Soc.* **2010**, *132*, 268–274.
- (24) Rycenga, M.; Langille, M. R.; Personick, M. L.; Ozel, T.; Mirkin, C. A. Chemically Isolating Hot Spots on Concave Nanocubes. *Nano Lett.* **2012**, *12*, 6218–6222.
- (25) Shao, Z.; Zhu, W.; Wang, H.; Yang, Q.; Yang, S.; Liu, X.; Wang, G. Controllable Synthesis of Concave Nanocubes, Right Bipyramids, and 5-Fold Twinned Nanorods of Palladium and Their Enhanced Electrocatalytic Performance. *J. Phys. Chem. C* **2013**, *117*, 14289–14294.
- (26) Jing, H.; Zhang, Q.; Large, N.; Yu, C.; Blom, D. A.; Nordlander, P.; Wang, H. Tunable Plasmonic Nanoparticles with Catalytically Active High-Index Facets. *Nano Lett.* **2014**, *14*, 3674–3682.
- (27) Kurouski, D.; Van Duyne, R. P. In Situ Detection and Identification of Hair Dyes Using Surface-Enhanced Raman Spectroscopy (SERS). *Anal. Chem.* **2015**, *87*, 2901–2906.
- (28) Szlag, V. M.; Styles, M. J.; Madison, L. R.; Campos, A. R.; Wagh, B.; Sprouse, D.; Schatz, G. C.; Reineke, T. M.; Haynes, C. L. SERS Detection of Ricin B-Chain via N-Acetyl-galactosamine Glycopolymers. *ACS Sensors* **2016**, *1*, 842–846.
- (29) Bantz, K. C.; Meyer, A. F.; Wittenberg, N. J.; Im, H.; Kurtulus, O.; Lee, S. H.; Lindquist, N. C.; Oh, S. H.; Haynes, C. L. Recent Progress in SERS Biosensing. *Phys. Chem. Chem. Phys.* **2011**, *13*, 11551–11567.
- (30) Camden, J. P.; Dieringer, J. A.; Zhao, J.; Van Duyne, R. P. Controlled Plasmonic Nanostructures for Surface-Enhanced Spectroscopy and Sensing. *Acc. Chem. Res.* **2008**, *41*, 1653–1661.
- (31) Dick, L. A.; McFarland, A. D.; Haynes, C. L.; Van Duyne, R. P. Metal Film Over Nanosphere (MFON) Electrodes for Surface-Enhanced Raman Spectroscopy (SERS): Improvements in Surface Nanostructure Stability and Suppression of Irreversible Loss. *J. Phys. Chem. B* **2002**, *106*, 853–860.
- (32) Kuncicky, D. M.; Prevo, B. G.; Velev, O. D. Controlled Assembly of SERS Substrates Templated by Colloidal Crystal Films. *J. Mater. Chem.* **2006**, *16*, 1207–1211.
- (33) Doherty, M. D.; Murphy, A.; McPhillips, J.; Pollard, R. J.; Dawson, P. Wavelength Dependence of Raman Enhancement from Gold Nanorod Arrays: Quantitative Experiment and Modeling of A Hot Spot Dominated System. *J. Phys. Chem. C* **2010**, *114*, 19913–19919.
- (34) Haynes, C. L.; McFarland, A. D.; Zhao, L. L.; Van Duyne, R. P.; Schatz, G. C.; Gunnarsson, L.; Prikulis, J.; Kasemo, B.; Kall, M. Nanoparticle Optics: the Importance of Radiative Dipole Coupling in Two-Dimensional Nanoparticle Arrays. *J. Phys. Chem. B* **2003**, *107*, 7337–7342.
- (35) De Jesus, M. A.; Giesfeldt, K. S.; Oran, J. M.; Abu-Hatab, N. A.; Lavrik, N. V.; Sepaniak, M. J. Nanofabrication of Densely Packed Metal-Polymer Arrays for Surface-Enhanced Raman Spectrometry. *Appl. Spectrosc.* **2005**, *59*, 1501–1508.
- (36) Félidj, N.; Aubard, J.; Lévi, G.; Krenn, J. R.; Hohenau, A.; Schider, G.; Leitner, A.; Aussenegg, F. R. Optimized Surface-Enhanced Raman Scattering on Gold Nanoparticle Arrays. *Appl. Phys. Lett.* **2003**, *82*, 3095–3097.
- (37) Zhang, M.; Large, N.; Koh, A. L.; Cao, Y.; Manjavacas, A.; Sinclair, R.; Nordlander, P.; Wang, S. X. High-Density 2D Homo- and Hetero- Plasmonic Dimers with Universal Sub-10-nm Gaps. *ACS Nano* **2015**, *9*, 9331–9339.
- (38) Le, F.; Brandl, D. W.; Urzhumov, Y. A.; Wang, H.; Kundu, J.; Halas, N. J.; Aizpurua, J.; Nordlander, P. Metallic Nanoparticle Arrays: A Common Substrate for Both Surface-Enhanced Raman Scattering and Surface-Enhanced Infrared Absorption. *ACS Nano* **2008**, *2*, 707–718.
- (39) Bernard, S.; Félidj, N.; Truong, S.; Peretti, P.; Levi, G.; Aubard, J. Study of Langmuir-Blodgett Phospholipidic Films Deposited on Surface Enhanced Raman Scattering Active Gold Nanoparticle Monolayers. *Biopolymers* **2002**, *67*, 314–318.
- (40) Seitz, O.; Chehimi, M. M.; Cabet-Deliry, E.; Truong, S.; Félidj, N.; Perruchot, C.; Greaves, S. J.; Watts, J. F. Preparation and



Characterisation of Gold Nanoparticle Assemblies on Silanised Glass Plates. *Colloids Surf., A* **2003**, *218*, 225–239.

(41) Kurouski, D.; Large, N.; Chiang, N.; Greeneltch, N.; Carron, K. T.; Seideman, T.; Schatz, G. C.; Van Duyne, R. P. Unraveling Near-Field and Far-Field Relationships for 3D SERS Substrates - A Combined Experimental and Theoretical Analysis. *Analyst* **2016**, *141*, 1779–1788.

(42) Yu, Q.; Guan, P.; Qin, D.; Golden, G.; Wallace, P. M. Inverted Size-Dependence of Surface-Enhanced Raman Scattering on Gold Nanohole and Nanodisk Arrays. *Nano Lett.* **2008**, *8*, 1923–1928.

(43) Dieringer, J. A.; McFarland, A. D.; Shah, N. C.; Stuart, D. A.; Whitney, A. V.; Yonzon, C. R.; Young, M. A.; Zhang, X.; Van Duyne, R. P. Surface Enhanced Raman Spectroscopy: New Materials, Concepts, Characterization Tools, and Applications. *Faraday Discuss.* **2006**, *132*, 9–26.

(44) Liao, P. F.; Bergman, J. G.; Chemla, D. S.; Wokaun, A.; Melngailis, J.; Hawryluk, A. M.; Economou, N. P. Surface-Enhanced Raman Scattering from Microlithographic Silver Particle Surfaces. *Chem. Phys. Lett.* **1981**, *82*, 355–359.

(45) Chen, C. Y.; Burstein, E. Giant Raman Scattering by Molecules at Metal-Island Films. *Phys. Rev. Lett.* **1980**, *45*, 1287–1291.

(46) Stiles, P. L.; Dieringer, J. A.; Shah, N. C.; Van Duyne, R. P. Surface-Enhanced Raman Spectroscopy. *Annu. Rev. Anal. Chem.* **2008**, *1*, 601–626.

(47) Kurouski, D.; Postiglione, T.; Deckert-Gaudig, T.; Deckert, V.; Lednev, I. K. Amide I Vibrational Mode Suppression in Surface (SERS) and Tip (TERS) Enhanced Raman Spectra of Protein Specimens. *Analyst* **2013**, *138*, 1665–1673.

(48) Brown, R. J.; Milton, M. J. T. Nanostructures and Nanostructured Substrates for Surface-Enhanced Raman Scattering (SERS). *J. Raman Spectrosc.* **2008**, *39*, 1313–1326.

(49) Gunnarsson, E. J.; Bjerneld, H.; Xu, S.; Petronis, B.; Kasemo, B.; Kall, M. Interparticle Coupling Effects in Nanofabricated Substrates for Surface-Enhanced Raman Scattering. *Appl. Phys. Lett.* **2001**, *78*, 802–804.

(50) Atay, T.; Song, J.-H.; Nurmikko, A. V. Large Enhancement of Fluorescence Efficiency from CdSe/ZnS Quantum Dots Induced by Resonant Coupling to Spatially Controlled Surface Plasmons. *Nano Lett.* **2004**, *4*, 1627–1631.

(51) Greeneltch, N. G.; Blaber, M. G.; Henry, A. I.; Schatz, G. C.; Van Duyne, R. P. Immobilized Nanorod Assemblies: Fabrication and Understanding of Large Area Surface-Enhanced Raman Spectroscopy Substrates. *Anal. Chem.* **2013**, *85*, 2297–2303.

(52) McFarland, A. D.; Young, M. A.; Dieringer, J. A.; Van Duyne, R. P. Wavelength-Scanned Surface-Enhanced Raman Excitation Spectroscopy. *J. Phys. Chem. B* **2005**, *109*, 11279–11285.

(53) Lumerical Solutions, Inc. FDTD Solutions. <http://www.lumerical.com/tcad-products/fdtd>.

(54) Lynch, D. W.; Hunter, W. R. An Introduction to the Data for Several Metals. In *Handbook of Optical Constants of Solids*; Palik, E. D., Ed.; Academic Press: Burlington, MA, 1997; Vol. 1; pp 275–367.

(55) Johnson, P. B.; Christy, R. W. Optical Constant of Noble Metals. *Phys. Rev. B* **1972**, *6*, 4370–4379.

(56) Masango, S. S.; Hackler, R. A.; Large, N.; Henry, A.-I.; McAnally, M. O.; Schatz, G. S.; Stair, P. C.; van Duyne, R. P. High-Resolution Distance Dependence Study of Surface-Enhanced Raman Scattering Enabled by Atomic Layer Deposition. *Nano Lett.* **2016**, *16*, 4251–4259.

(57) Ringe, E.; Langille, M. R.; Sohn, K.; Zhang, J.; Huang, J.; Mirkin, C. A.; Van Duyne, R. P.; Marks, L. D. Plasmon Length: A Universal Parameter to Describe Size Effects in Gold Nanoparticles. *J. Phys. Chem. Lett.* **2012**, *3*, 1479–1483.

(58) Ringe, E.; Sharma, B.; Henry, A. I.; Marks, L. D.; Van Duyne, R. P. Single Nanoparticle Plasmonics. *Phys. Chem. Chem. Phys.* **2013**, *15*, 4110–4129.

(59) Zuloaga, J.; Nordlander, P. On the Energy Shift Between Near-Field and Far-Field Peak Intensities in Localized Plasmon Systems. *Nano Lett.* **2011**, *11*, 1280–1283.

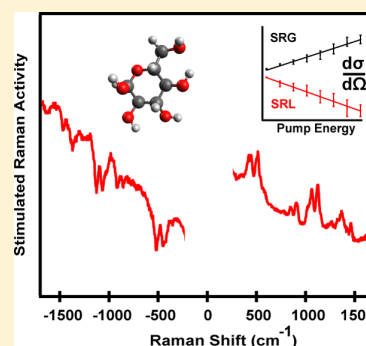
# Quantitative Determination of the Differential Raman Scattering Cross Sections of Glucose by Femtosecond Stimulated Raman Scattering

Michael O. McAnally,<sup>†</sup> Brian T. Phelan,<sup>†,‡</sup> Ryan M. Young,<sup>†,‡</sup> Michael R. Wasielewski,<sup>†,‡</sup> George C. Schatz,<sup>†</sup> and Richard P. Van Duyne<sup>\*,†</sup>

<sup>†</sup>Department of Chemistry and <sup>‡</sup>Argonne-Northwestern Solar Energy Research Center, Northwestern University, Evanston, Illinois 60208-3113, United States

**S** Supporting Information

**ABSTRACT:** Femtosecond stimulated Raman spectroscopy (FSRS) is a vibrational spectroscopy technique that has been used in a wide variety of applications: from transient vibrational signature tracking to amplifying weak normal Raman scattering signals. Presented here is an application of FSRS to quantify the differential Raman scattering cross sections (DRSCs) of glucose. In using FSRS to determine the DRSCs of multiple glucose vibrational modes, we demonstrate the applicability of both stimulated Raman loss (SRL) spectroscopy and stimulated Raman gain (SRG) FSRS. Using the two analogous FSRS techniques, SRG and SRL, we determine that the DRSCs of glucose excited at 514.5 nm range from a low of  $5.0 \pm 1.1 \times 10^{-30}$  to a high of  $8.9 \pm 0.9 \times 10^{-30}$  cm<sup>2</sup> molecule<sup>-1</sup> sr<sup>-1</sup>. This work establishes both the compatibility of SRL for measuring DRSCs and values for the DRSC of multiple vibrational modes of glucose.



An accurate value for the Raman scattering cross section of an analyte is a requirement for assessing the likelihood of success for a proposed measurement. As the Raman scattering cross section describes the scattering activity of an analyte, it is easy to compare the utility of different Raman scattering techniques for observing an analyte. While the Raman scattering cross section is an important property, it can be quite difficult to measure using normal Raman scattering (NRS), which measures the differential Raman scattering cross section (DRSC) by comparison with a standard.<sup>1,2</sup>

An alternative approach to using NRS for measuring Raman scattering cross sections is to use stimulated Raman scattering.<sup>3</sup> Femtosecond stimulated Raman scattering (FSRS) is the implementation that will be used here. FSRS has numerous advantages over NRS for measuring DRSCs, including being a self-referencing technique to remove instrument response from grating and camera efficiencies, removing ambiguities of solid angle scattering collection in NRS due to FSRS being a coherent scattering process, and increasing Raman scattering efficiency over NRS by coherent processes. In comparing FSRS to NRS, it is important to note that the DRSC is an intrinsic molecular property. The boost in Raman scattering efficiency from FSRS compared to NRS is due to the collection of coherent oscillators emitting Raman shifted photons in a stimulated manner from the driven macroscopic polarization in FSRS compared to the incoherent oscillators spontaneously emitting Raman shifted photons in NRS.

Ground state, or nontransient FSRS, has been used to measure the Raman scattering cross sections for a variety of

analytes, including resonant dye molecules.<sup>4–6</sup> FSRS as a vibrational spectroscopy technique has been used extensively for measuring transient vibrational features of photoexcited species when coupled with a photoexcitation, or actinic, pulse.<sup>7,8</sup> However, the stimulated Raman process in itself is useful as the coherent Raman process boosts the Raman scattering efficiency compared to NRS. FSRS can be performed as either a stimulated Raman gain (SRG) or a stimulated Raman loss (SRL) process.<sup>9,10</sup> As FSRS cross section measurements have been shown to be identical to NRS measurements, the more highly efficient FSRS measurements are helpful for weakly scattering systems. An important analyte that falls into this category is glucose.

Glucose is the most important molecule in the metabolic chain. The concentration of glucose is a key diagnostic quantity for many metabolic disorders, most notably diabetes.<sup>11</sup> The importance of glucose has led to many researchers attempting to quantify glucose concentration in vivo using Raman scattering techniques,<sup>12–14</sup> including SRS microscopy.<sup>15</sup> As NRS studies of glucose showed very weak scattering,<sup>16,17</sup> surface-enhanced Raman scattering (SERS)<sup>12,13</sup> and coherent Raman scattering techniques<sup>14,15</sup> were used to enhance the low overall NRS signal (shown in Figure S-4).

Unfortunately, previous research<sup>12,13</sup> either cites a literature value of the DRSC that references unpublished and nonpeer

**Received:** April 10, 2017

**Accepted:** June 8, 2017

**Published:** June 13, 2017



reviewed data for the DRSC of the  $1126\text{ cm}^{-1}$  mode of glucose<sup>1,18</sup> or simply omits the exact value. To resolve this issue, we utilize FSRS to quantitatively determine its DSRCs using both SRL and SRG simultaneously.

To measure a FSRS signal, a chopper is frequently employed to modulate the Raman pump field. Modulation of the Raman pump field, when synced with a camera, measures sequential Raman pump-on and Raman pump-off intensities of the Raman probe field as shown in eq 1.<sup>3</sup>

$$I_{\text{FSRS}} = \frac{(I_{\text{probe}})_{\text{pump-on}}}{(I_{\text{probe}})_{\text{pump-off}}} \quad (1)$$

As the stimulated Raman activity only occurs when both the Raman pump and probe fields are coincident in time and space inside the sample, measuring the ratio allows for extraction of the FSRS intensity. The FSRS signal being proportional to a ratio of intensities makes the technique well-suited for measuring optical properties as instrument response issues related to grating and detector efficiencies are normalized.<sup>1–3</sup>

The signal intensity in FSRS can be approximated as shown in eq 2<sup>3</sup>

$$I_{\text{FSRS}} = a \times \sigma_{\text{R}} \times l \times N \times I_{\text{RP}} \quad (2)$$

where the intensity of the FSRS signal ( $I_{\text{FSRS}}$ ), or stimulated Raman activity, is linear with respect to a collection of analyte-independent physical constants ( $a$ ), the analyte total Raman scattering cross section ( $\sigma_{\text{R}}$ ), path length ( $l$ ), analyte concentration ( $N$ ), and Raman pump power ( $I_{\text{RP}}$ ). Thus, performing a study of the stimulated Raman activity as a function of Raman pump power can isolate the analyte total Raman scattering cross section along with a collection of controllable physical constants.

While FSRS provides information about the total Raman scattering cross section, the more commonly referenced fundamental Raman scattering property is the DRSC. To measure an absolute DRSC of an analyte, tightly controlled experimental conditions including polarization and geometry need to be used.<sup>1,2,19,20</sup> Alternatively, the same physical information can be obtained by measuring the Raman scattering properties of an analyte in reference to a known absolute DRSC.<sup>1,2,21</sup>

There are important motivations for the use of FSRS over NRS in the approach taken herein. While the self-referencing for grating and camera instrumental responses that are intrinsic to FSRS are helpful, these same properties exist when performing the relative DRSC experiment in NRS. However, FSRS still has the advantage over NRS as it (1) allows for a more complete collection of signal photons compared to the isotropic scatter of NRS and (2) takes advantage of the multiple field–matter interactions in coherent Raman scattering to more efficiently create signal photons in the probe field compared to spontaneously emitted signal photons from NRS.

To measure the relative DRSCs of glucose, we use an approach similar to that used previously.<sup>3–6</sup> However, unlike the previous studies, we use a sufficiently broad continuum that overlaps the Raman pump on both the Stokes and anti-Stokes frequencies simultaneously, dispersing the full SRG and SRL spectra on the CCD. Briefly, the concept is as follows: by using FSRS, the stimulated Raman activity as a function of Raman pump power can be determined, fit in a linear regime, and compared to a known standard.

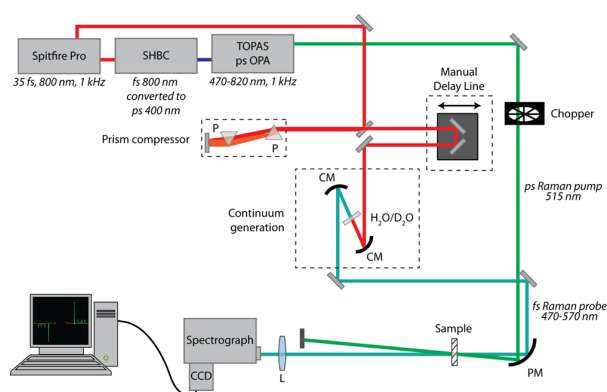


**Figure 1.** Experimental FSRS setup for measuring DRSCs of glucose consisting of an amplified Ti:sapphire laser system, a second harmonic bandwidth compressor (SHBC), a tunable picosecond optical parametric amplifier (TOPAS), curved mirrors (CM), prisms (P), lens (L), parabolic mirror (PM), spectrograph, and CCD camera.

A 1 kHz Ti:sapphire system (Spitfire Pro, Spectra Physics), described previously,<sup>22</sup> was used for this experiment (Figure 1). Specifically, <35 mW of the fundamental was directed through a prism compressor, along a manual stage, and into a 50:50 mixture of  $\text{H}_2\text{O}/\text{D}_2\text{O}$  in a 5 mm cuvette for continuum generation, creating the chirped Raman probe (470–570 nm), which was determined to be <100 fs at a single frequency and ~500 fs across the entire frequency range. Approximately 1.5 W was split from the fundamental to pump a second harmonic bandwidth compressor (SHBC, Light Conversion), which creates an intense 400 nm picosecond bandwidth pulse that pumped a commercial tunable optical parametric amplifier (TOPAS-400-WL, Light Conversion). The TOPAS was tuned to an output center wavelength of 514.5 nm (~0.7 ps), creating a Raman pump that matches the literature values for DRSCs of glucose and cyclohexane used in the present study.<sup>1,20</sup> The Raman probe was overlapped temporally with the Raman pump, chopped at 125 Hz; then, both were focused into the sample (2 mm quartz cuvette) by a parabolic mirror. The transmitted Raman probe containing the stimulated Raman activity was focused into a spectrograph (Triax 180, Horiba Jobin Yvon), dispersed using a 1200 gv/mm grating, and recorded as differential optical density ( $\Delta\text{OD}$ ) on a CCD camera (PIXIS 100B, Princeton Instruments) using home-built LabView programming. The spectral resolution of the experiment was determined to be sub-20  $\text{cm}^{-1}$  based on fitting solvent modes near the glucose modes of interest (Figure S3, Table S-2). Using this system, FSRS spectra of 1 M aqueous glucose and neat cyclohexane were obtained in triplicate at Raman pump pulse energies of 0.2–1.6  $\mu\text{J}/\text{pulse}$  with 2 min acquisition times per spectrum.

Individual FSRS spectra of glucose showing the simultaneous SRL and SRG stimulated Raman activity at the highest (1.6  $\mu\text{J}/\text{pulse}$ ) and lowest (0.2  $\mu\text{J}/\text{pulse}$ ) Raman pump energies are displayed in Figure 2. The increasing background near the Raman pump is attributed to cross-phase modulation.<sup>3</sup> The decision to display Raman pump energy instead of Raman pump power was made to allow for easier conversion when considering higher repetition rate laser systems. As will be seen in eq 3, there is no functional difference between measuring a stimulated Raman activity as a function of Raman pump power

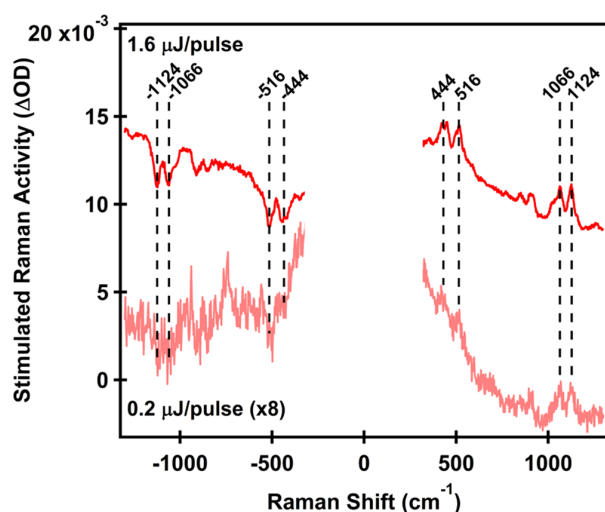


**Figure 2.** FSRS spectra of the lowest (0.2 uJ/pulse) and highest (1.6 uJ/pulse) Raman pump energies of the linear Raman pump regime used in the experimental determination of the DRSCs of glucose. Labeled peaks have DRSCs determined by use of eq 3 and are reported in Table 1. Spectra have been shifted vertically for clarity.

or energy because the relevant parameter is a ratio in which repetition rate dependencies are removed.

The method of measuring the DRSC indirectly can be adapted to the total Raman scattering cross sections measured in FSRS (see eqs S-1–S-7) by incorporating the effects of the linear Raman scattering depolarization ratio:<sup>2</sup>

$$\frac{d\sigma_{R,glu}}{d\Omega} = \left( \frac{1 + \rho_{R,glu}}{1 + 2\rho_{R,glu}} \right) \left( \frac{1 + 2\rho_{R,chl}}{1 + \rho_{R,chl}} \right) \left( \frac{m_{glu}}{m_{chl}} \right) \left( \frac{N_{chl}}{N_{glu}} \right) \frac{d\sigma_{R,chl}}{d\Omega} \quad (3)$$

Eq 3 shows that the relative DRSCs of glucose (glu) with respect to cyclohexane (chl) can be measured by using the linear Raman scattering depolarization ratios (obtained from ref 17), the concentrations of glucose and cyclohexane, a known value of the absolute DRSC of cyclohexane, and the ratio of the linear fits of stimulated Raman activity with respect to Raman pump power or energy. This method is in contrast to the process of directly measuring the total cross section which requires knowledge of the total spectral photon flux, a quantity that is exceedingly difficult to measure accurately across the broad spectral range used in the current experiment.<sup>23</sup>

Using the FSRS apparatus shown in Figure 1, we obtained the integrated stimulated Raman activity as a function of Raman pump energy. When the Raman pump energy dependence for each vibrational mode of interest in glucose was fit (444, 516, 1066, 1124  $\text{cm}^{-1}$ ), linear fits were obtained for both SRL and SRG (see Figure S-1). The range of Raman pump pulse energies used was verified to provide linear response in the stimulated Raman activity for both SRL and SRG in the reference neat cyclohexane system (see Figure S-2). In Table 1, we summarize the results of the DRSCs obtained by SRL and SRG for glucose along with values of the DRSCs for the 1126  $\text{cm}^{-1}$  (1124  $\text{cm}^{-1}$  in the current study) mode of glucose and the 802  $\text{cm}^{-1}$  (801  $\text{cm}^{-1}$  in the current study) mode of cyclohexane; all were obtained with Raman pump wavelengths of 514.5 nm.

**Table 1.** Results of the Study Performed Herein, Along with the Literature Values for Glucose and Cyclohexane<sup>a</sup>

molecule	$\nu_{\text{exp}}$ ( $\text{cm}^{-1}$ )	$d\sigma/d\Omega$ ( $\text{cm}^2 \text{ molecule}^{-1} \text{ sr}^{-1} \times 10^{-30}$ )
glucose	444 (SRL)	$6.5 \pm 0.6$
	444 (SRG)	$6.1 \pm 0.9$
	516 (SRL)	$8.9 \pm 0.9$
	516 (SRG)	$5.9 \pm 1.0$
	1066 (SRL)	$5.0 \pm 1.1$
	1066 (SRG)	$5.3 \pm 0.5$
	1124 (SRL)	$6.4 \pm 0.5$
	1124 (SRG)	$6.3 \pm 0.8$
glucose	1126	5.6
cyclohexane	802	5.2

<sup>a</sup>The literature value for the 1126  $\text{cm}^{-1}$  mode of glucose is from ref 1, and the literature value for the 801  $\text{cm}^{-1}$  mode of cyclohexane is from ref 20. All DRSCs were evaluated at an excitation wavelength of 514.5 nm.

From the results in Table 1, the DRSCs of glucose vary between  $5.0 \times 10^{-30}$  and  $8.9 \times 10^{-30} \text{ cm}^2 \text{ molecule}^{-1} \text{ sr}^{-1}$  for the 444, 516, 1066, and 1124  $\text{cm}^{-1}$  vibrational modes. The literature value<sup>1</sup> of  $5.6 \times 10^{-30} \text{ cm}^2 \text{ molecule}^{-1} \text{ sr}^{-1}$  is an unsubstantiated value<sup>18</sup> that we confirm with the present experimental work and expand to further vibrational modes of interest. The DRSC discrepancy for the 516  $\text{cm}^{-1}$  mode is likely due to differing backgrounds near the mode when comparing the SRL and SRG sides as seen in Figure 2.

The results summarized in Table 1 do raise an important question: why is glucose so difficult to observe by Raman scattering if the DRSC of glucose is so similar to cyclohexane?<sup>12,13,15</sup> To answer that question, we examine calculated DRSCs for both cyclohexane and glucose using density functional theory (DFT).<sup>24</sup>

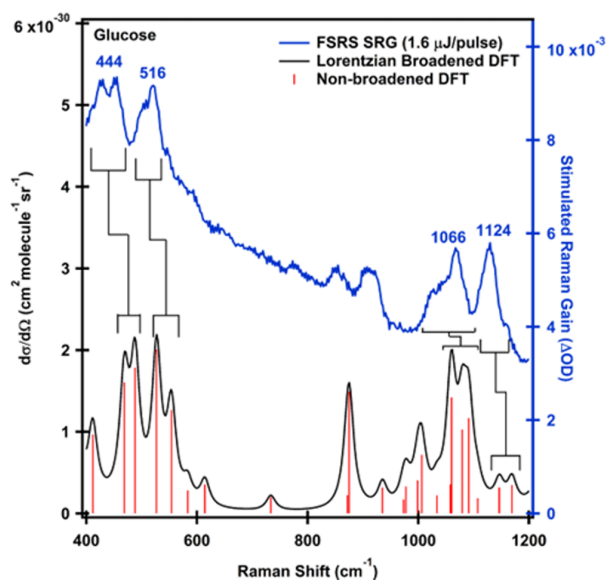


**Figure 3.** Comparison of FSRS SRG (blue) to DFT calculated (black and red) Raman scattering spectra for glucose using gas-phase geometry (see Supporting Information for details on calculations). The bracketed regions are to guide the eye for comparisons between experimental and calculated spectra.



When one examines Figures 3 and 4, the difference in empirically observed Raman scattering intensity can be traced to the relatively complicated vibrational manifold of glucose compared to cyclohexane. In glucose, the peaks nominally labeled as 444, 516, 1066, and 1124  $\text{cm}^{-1}$  are in reality convoluted spectra of multiple vibrational modes. Meanwhile in cyclohexane, the Raman spectrum is dominated by fewer overall vibrational modes. Thus, when comparing the two molecules and their Raman scattering activity, an important point to consider is the broader distribution of vibrational modes present in the “single” peaks of glucose compared to cyclohexane. The effect of inhomogeneous line broadening due to a combination of multiple conformations and hydrogen bonding further complicates the Raman spectrum of glucose in aqueous solutions.<sup>14,25–27</sup> The effects of multiple vibrational modes contained in “single peaks” of glucose, multiple conformations, and hydrogen bonding effectively widen the peaks making them less distinguishable relative to cyclohexane.

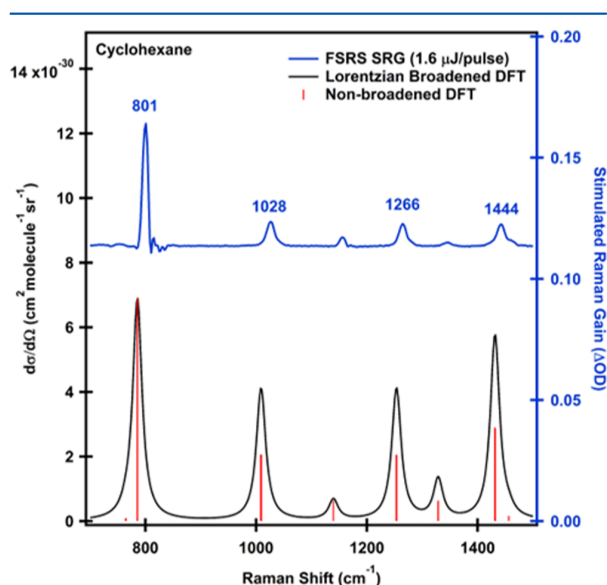


**Figure 4.** Comparison of FSRS SRG (blue) to DFT calculated (black and red) Raman scattering spectra for cyclohexane using gas-phase geometry.

In conclusion, we demonstrate for the first time the applicability of SRL for measuring DRSCs of weakly scattering analytes. SRL has been considered for many theoretical considerations and has been demonstrated to have the highest possible stimulated Raman activity.<sup>28–30</sup> However, this is the first study to show the applicability of SRL for DRSC measurements. For the presented case of glucose, we have determined the DRSC to be in line with previously reported, but unsubstantiated, values for the 1124  $\text{cm}^{-1}$  mode of glucose. The generality of using either SRL or SRG for measuring DRSCs is highly advantageous as it allows for flexibility in experimental system constraints from laser equipment to wavelength dependent extinction effects.

## ■ ASSOCIATED CONTENT

### Supporting Information

The Supporting Information is available free of charge on the ACS Publications website at DOI: 10.1021/acs.analchem.7b01335.

Linear plots of glucose and cyclohexane integrated stimulated Raman activity used for determining the differential Raman scattering cross sections, table of linear Raman scattering depolarization ratio values, derivation of eq 3, details of DFT calculations for differential Raman scattering cross sections of glucose and cyclohexane, and normal Raman scattering spectrum of aqueous glucose (PDF)

## ■ AUTHOR INFORMATION

### Corresponding Author

\*E-mail: vanduyne@northwestern.edu. Phone: 847-491-3516. Fax: 847-491-7713.

### ORCID

Michael O. McAnally: 0000-0002-8681-2952  
Brian T. Phelan: 0000-0002-5849-0319  
Ryan M. Young: 0000-0002-5108-0261  
Michael R. Wasielewski: 0000-0003-2920-5440  
George C. Schatz: 0000-0001-5837-4740

### Author Contributions

The manuscript was written through contributions of all authors. All authors have given approval to the final version of the manuscript.

### Notes

The authors declare no competing financial interest.

## ■ ACKNOWLEDGMENTS

The authors thank Ji Eun Park for providing the glucose normal Raman scattering spectrum in Figure S-4. M.O.M., G.C.S., and R.P.V.D. were supported by the National Science Foundation Center for Chemical Innovation dedicated to Chemistry at the Space-Time Limit (CaSTL) Grant CHE-1414466. M.O.M. acknowledges support from the National Science Foundation Graduate Research Fellowship Program (DGE-0824162). This work was supported by the Chemical Sciences, Geosciences, and Biosciences Division, Office of Basic Energy Sciences, DOE under Grant No. DE-FG02-99ER14999 (B.T.P., R.M.Y., M.R.W.). This work was supported by the Assistant Secretary of Defense for Health Affairs, through the Peer Reviewed Medical Research Program under Award No. W81XWH-16-1-0375. Opinions, interpretations, conclusions, and recommendations are those of the author and are not necessarily endorsed by the Department of Defense.

## ■ REFERENCES

- (1) McCreery, R. L. *Raman spectroscopy for chemical analysis*; John Wiley & Sons: New York, 2000.
- (2) Le Ru, E.; Etchegoin, P. G. *Principles of surface-enhanced Raman spectroscopy and related plasmonic effects*; Elsevier: Amsterdam, The Netherlands, 2009.
- (3) McCamant, D. W.; Kukura, P.; Yoon, S.; Mathies, R. A. *Rev. Sci. Instrum.* **2004**, 75 (11), 4971–4980.
- (4) Shim, S.; Stuart, C. M.; Mathies, R. A. *ChemPhysChem* **2008**, 9 (5), 697–699.
- (5) Lee, J.; Challa, J. R.; McCamant, D. W. *J. Raman Spectrosc.* **2013**, 44 (9), 1263–1272.

- (6) Silva, W. R.; Keller, E. L.; Frontiera, R. R. *Anal. Chem.* **2014**, *86* (15), 7782–7787.
- (7) Kukura, P.; McCamant, D. W.; Yoon, S.; Wandschneider, D. B.; Mathies, R. A. *Science (Washington, DC, U. S.)* **2005**, *310* (5750), 1006–1009.
- (8) Kukura, P.; McCamant, D. W.; Mathies, R. A. *Annu. Rev. Phys. Chem.* **2007**, *58*, 461–488.
- (9) Frontiera, R. R.; Shim, S.; Mathies, R. A. *J. Chem. Phys.* **2008**, *129* (6), 64507.
- (10) Umaphathy, S.; Lakshmanan, A.; Mallick, B. J. *Raman Spectrosc.* **2009**, *40* (3), 235–237.
- (11) Alberts, B.; Bray, D.; Hopkin, K.; Johnson, A.; Lewis, J.; Raff, M.; Roberts, K.; Walter, P. *Essential cell biology*, 4th ed.; Garland Science: New York, 2013.
- (12) Shafer-Peltier, K. E.; Haynes, C. L.; Glucksberg, M. R.; Van Duyne, R. P. *J. Am. Chem. Soc.* **2003**, *125* (2), 588.
- (13) Shah, N. C.; Yuen, J. M.; Lyandres, O.; Glucksberg, M. R.; Walsh, J. T.; Van Duyne, R. P. In *In Vivo Glucose Sensing*; Cunningham, D. D., Stenken, J. A., Eds.; John Wiley & Sons: New York, 2010; pp 421–443.
- (14) Wang, X.; Zhang, A.; Zhi, M.; Sokolov, A. V.; Welch, G. R. *Phys. Rev. A: At, Mol, Opt. Phys.* **2010**, *81* (1), 13813.
- (15) Hu, F.; Chen, Z.; Zhang, L.; Shen, Y.; Wei, L.; Min, W. *Angew. Chem.* **2015**, *127* (34), 9959–9963.
- (16) Vasko, P. D.; Blackwell, J.; Koenig, J. L. *Carbohydr. Res.* **1972**, *23* (3), 407–416.
- (17) Mathlouthi, M.; Luu, D. V. *Carbohydr. Res.* **1980**, *81*, 203–212.
- (18) Ray, K. G. Ph.D. Thesis, *Spatially resolved Raman spectroscopy of carbon electrode materials: A study of surface microstructure and reactivity*, Ohio State University, Columbus, OH, 1998.
- (19) Schrötter, H. W.; Klöckner, H. W. In *Raman Spectroscopy of Gases and Liquids*; Weber, A., Ed.; Springer Berlin Heidelberg: Berlin, Heidelberg, 1979; pp 123–166.
- (20) Trulson, M. O.; Mathies, R. A. *J. Chem. Phys.* **1986**, *84*, 2068.
- (21) Le Ru, E. C.; Blackie, E. J.; Meyer, M.; Etchegoin, P. G. *J. Phys. Chem. C* **2007**, *111* (37), 13794–13803.
- (22) Brown, K. E.; Veldkamp, B. S.; Co, D. T.; Wasielewski, M. R. *J. Phys. Chem. Lett.* **2012**, *3* (17), 2362–2366.
- (23) McCamant, D. W.; Kukura, P.; Mathies, R. A. *J. Phys. Chem. A* **2003**, *107* (40), 8208–8214.
- (24) Baerends, E. J.; Ziegler, T.; Autschbach, J.; Bashford, D.; Bérces, A.; Bickelhaupt, F. M.; Bo, C.; Boerrigter, P. M.; Cavallo, L.; Chong, D. P.; Deng, L.; Dickson, R. M.; Ellis, D. E.; van Faassen, M.; Fan, L.; Fischer, T. H.; Fonseca Guerra, C.; Franchini, M.; Ghysels, A.; Giammona, A.; van Gisbergen, S. J. ; Götz, A.; Groeneveld, J. A.; Gritsenko, O. V.; Grüning, M.; Gusarov, S.; Harris, S. E.; van den Hoek, P.; Jacob, C. R.; Jacobsen, H.; Jensen, L.; Kaminski, J. W.; van Kessel, G.; Kootstra, F.; Kovalenko, A.; Krykunov, M. V.; van Lenthe, E.; McCormack, D. A.; Michalak, A.; Mitoraj, M.; Morton, S. M.; Neugebauer, J.; Nicu, V. P.; Noodleman, L.; Osinga, V. P.; Patchkovskii, S.; Pavanello, M.; Philipsen, P. H. T.; Post, D.; Pye, C. C.; Ravenek, W.; Rodríguez, J. I.; Ros, P.; Schipper, P. R. T.; van Schoot, H.; Schreckenbach, G.; Seldenthuis, J. S.; Seth, M.; Snijders, J. G.; Solà, M.; Swart, M.; Swerhone, D.; te Velde, G.; Vernooijs, P.; Versluis, L.; Visscher, L.; Visser, O.; Wang, F.; Wesolowski, T. A.; van Wezenbeek, E. M.; Wiesenekker, G.; Wolff, S. K.; Woo, T. K.; Yakovlev, A. L. *SCM Theoretical Chemistry*; Vrije Universiteit: Amsterdam, The Netherlands, 2010.
- (25) Arboleda, P. H.; Loppnow, G. R. *Anal. Chem.* **2000**, *72* (9), 2093–2098.
- (26) Molteni, C.; Parrinello, M. *J. Am. Chem. Soc.* **1998**, *120* (9), 2168–2171.
- (27) Mathlouthi, M.; Luu, C.; Meffroy-Biget, A. M.; Vinh Luu, D. *Carbohydr. Res.* **1980**, *81* (2), 213–223.
- (28) Zhao, B.; Niu, K.; Li, X.; Lee, S.-Y. *Sci. China: Chem.* **2011**, *54* (12), 1989–2008.
- (29) Mallick, B.; Lakshmanan, A.; Umaphathy, S. *J. Raman Spectrosc.* **2011**, *42* (10), 1883–1890.
- (30) Harbola, U.; Umaphathy, S.; Mukamel, S. *Phys. Rev. A: At, Mol, Opt. Phys.* **2013**, *88* (1), 11801.